Università degli Studi di Salerno

Dipartimento di Fisica "E. R. Caianiello" e Dipartimento di Matematica

in convenzione con

Università degli Studi della Campania "Luigi Vanvitelli"

Dipartimento di Matematica e Fisica

Dottorato di Ricerca "Matematica, Fisica e Applicazioni"

XXIX Ciclo

Curriculum Fisica

Tesi di dottorato

Crystal growth and physical properties of helimagnetic oxides

Candidato

Luisa Rocco

Tutor

Dr. Antonio Vecchione

Coordinatore

Ch.mo Prof. Sandro Pace

Contents

Abstract

This work is focused on two helimagnetic materials: $Ba_2CuGe_2O_7$ and $Cu_3Nb_2O_8$. Recent studies report a number of interesting anisotropic properties.

$Ba_2CuGe_2O_7$ melilite oxide shows a complex magnetic behaviour, indeed it is known that at low temperature the system undergoes a transition from a paramagnetic phase to an incommensurate antiferromagnetic cycloid spin structure. Applying a magnetic field, additional magnetic transitions take place, as for example a spin-cone phase. Moreover, $Ba_2CuGe_2O_7$ shows also multiferroic properties.

Several works report that the physical properties of melilite oxides mainly depend on the nature of the transition metal ion, thus interesting properties could emerge in mixed melilite oxides. In this work $Ba_2MGe_2O_7$ with M=Cu,Ni and Mn have been studied.

$Cu_3Nb_2O_8$ is an unusual helimagnetic compound that undergoes a series of magnetic ordering at low temperature. Development of electric polarization $\mathbf{P}$ has been reported at $T_N \sim 25K$ corresponding to emergence of a non-collinear helicoidal ordering. $\mathbf{P}$ is oriented perpendicularly to the common plane of rotation of the spins. This observation cannot be reconciled with the conventional theory developed for cycloidal multiferroics.

The study of all these complex anisotropic phenomena requires the availability of good single crystals.

In this thesis, an investigation on crystal growth conditions of $Ba_2MGe_2O_7$ and of $Cu_3Nb_2O_8$ will be presented. Single crystal samples are vital to study the physical properties exhibited by compounds which have high magnetic/ferroelectric anisotropy where significantly different behaviour is seen along different crystallographic directions.

Preliminarily, high quality polycrystalline powders have been prepared for all compounds, indeed this is a critical point to grow pure crystalline samples.

In this work the procedure to synthesize polycrystalline powders with high purity is reported. Moreover, by using powder X-ray diffraction and energy dispersive spectroscopy (EDS), the composition of the starting polycrystalline powder is checked.

Successfully, the growth conditions to realize large and pure single crystals suitable for low temperature magnetometry and lattice dynamic studies are described.

The chemical composition and the morphology of the crystals are investigated by X-ray diffraction and by scanning electron microscopy (SEM), with wavelength dispersive spectrometry (WDS). Furthermore, the excellent quality of the crystals is confirmed by rocking curve measurements.

The X-ray Laue back reflection and electron backscattered diffraction (EBSD) techniques are used to orient single crystals specifically for selected experiments.

To study the magnetic phase diagrams of grown crystals, magnetization measurement vs temperature is performed in the range 1.5 K<T<300K on both $Ba_2CuGe_2O_7$ and $Cu_3Nb_2O_8$ crystals. Moreover, low temperature (0.5 K<T<5 K) magnetometry study is performed on oriented single crystal of $Ba_2CuGe_2O_7$. For the first time, a magnetic phase below 0.6 K is detected.

Finally, this work reports lattice dynamics of $Ba_2CuGe_2O_7$ helimagnet provided by Infra-red and Raman spectra.

Introduction

In addition to the well-known magnetic orders (ferromagnetism, antiferromagnetism, etc.) in the solid state, a series of more complex magnetic structures appear. For example, materials hosting not-uniformly ordered magnetic phases are of great interest. Among these candidates, there are helimagnetic systems, in which the spins twist along one direction forming periodic modulation [1, 2, 3, 4]. In spiral magnetic structures, the magnetic moments of adjacent atoms are rotated to one another in such a way that the vectors that represent them lie on the same spiral. The essential difference between spiral magnetic structures and other magnetic structures is that in the general case the pitch of the spiral is incommensurable with the corresponding period of the crystal lattice and, in addition, is temperature-dependent. There are several types of spiral magnetic structures, two examples are illustrated in Fig.1 .

Fig.1 a) shows a helical spiral where the moments rotate in a perpendicular plane to the axis of the spiral, while Fig.1 b) shows a conical magnetic structure which represents a distortion of the previous structure.

Recent studies reported complex magnetic phase diagrams of magnets as for example MnSi, $Fe_{0.8}Co_{0.2}Si$, $Fe_{0.5}Co_{0.5}Si$ and FeGe [5, 6, 7, 8]. These compounds are very different in terms of chemical composition and crystalline structure. Nevertheless, all magnetic phase diagrams show a common platform indicating a helimagnetic phase. When physical conditions change (applied magnetic field, temperature, etc.) a variety of complex magnetic phases are observed, as for example conical spirals (a conical distortion of the helical structure) and magnetic vortices (spin texture where, generally, the spin at the core points down, while spins at the perimeter point up).

In $Ba_2CuGe_2O_7$ [9] and in $Cu_3Nb_2O_8$ [10] an electric polarization is observed when they are ordered magnetically.

Helimagnetism shows interesting consequences, as for example the emergence
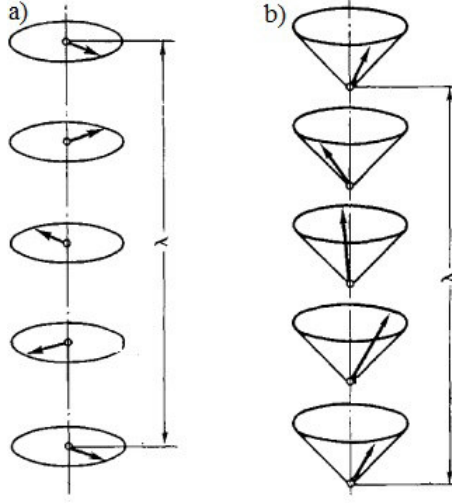
Figure 1: . Examples of spiral magnetic structures (λ is the period of the spiral):
a) helical spiral magnetic structure b) ferromagnetic (conical) spiral.

of spontaneous (ferroelectric) polarization mediated by the spin-exchange and spin orbit interactions has been observed [11]. Various types of spin order can have a potential to break the inversion symmetry and produce a spontaneous ferroelectric polarization **P**. When the spins form a transverse-spiral (cycloidal) modulation along a specific crystallographic direction, every nearest-neighbour spin pair produces a unidirectional local P and, hence, the macroscopic **P** of electronic (spin) origin should be generated [11].

On the theoretical level, research has focused on the interactions determining the helimagnetism.

Systems lacking inversion symmetry, such as selected three-dimensional compounds, multilayers and surfaces support Dzyaloshinsky-Moriya (DM) spin-orbit interactions [12, 13, 14]. In recent years DM interactions have attracted great interest, because they may stabilize magnetic structures with a unique chirality and non-trivial topology. The inherent coupling between the various properties provided by DM interactions is potentially relevant for a variety of applications including, for instance, multiferroic and spintronic devices [15]. Therefore, the exploration of new magnetic materials is an important task to study complex and magnetic phenomena and in the development of future information technology.

Multiferroic materials simultaneously exhibit ferroelectricity and magnetism and provide alternative ways to encode and store data using both electric polarization and magnetization. Moreover, the mutual control between electric polarization and magnetization due to the strong magnetoelectric coupling

gives even more potential to applications in the sensor industry, spintronics and so on.

A spintronic device, generally, doesn't need an applied electric current in order to retain information and so have a much lower power consumption than typical charge-based devices. Spintronics could theoretically be used for magnetic random access memory (MRAM). Applying a magnetic field may be possible to control the magnetisation state of a sample allowing less waste of power.

Another proposed practical application for multiferroic materials is as read heads for magnetic storage devices [16, 17]. Nowadays, read heads make use of magnetoresistance effects while by the use of a multiferroic device an output voltage could be generated in the absence of an external current. This would then lead to reduced power consumption of the device, which is particularly valuable for battery powered handheld devices.

In general, three different microscopic mechanisms of ferroelectricity of spin origin has been identified: exchange-striction, spin-current model and spin dependent *p-d* hybridization [11]. The exploration of those mechanisms lead to the discovery of materials showing the coupled cycloidal spin and ferroelectric orders.

In this work two helimagnetic systems are studied, in the case of $Ba_2CuGe_2O_7$ the ferroelectric order is due to spin dependent *p-d* hybridization [9], while in the case of $Cu_3Nb_2O_8$ is related to the spin-current model [10].

$Ba_2CuGe_2O_7$ is a melilite-type oxide with non-centro symmetric tetragonal crystal structure. This insulator material shows a complex magnetic phase diagram where the spin structure sensitively depends on the orientation of the magnetic field and undergoes several phase transitions [18]. Helical magnetic structure is promoted by DM interaction below T_N=3K. At low temperature and for magnetic field applied (H∼2T) along *c*-axis, antiferromagnetic cone phase is observed. The spins are mostly aligned in a commensurate antiferromagnetic pattern in the *ab* plane. In addition, there is a small incommensurate precession of transverse spin components.

The system $Cu_3Nb_2O_8$ is an unusual multiferroic compound that undergoes a series of magnetic ordering at low temperatures. Development of electric polarization has been reported at T_N ∼25K with the emergence of a non-collinear helicoidal ordering [10].

$Cu_3Nb_2O_8$ shows an improper ferroelectricity because the electrical polarization is oriented perpendicularly to the common plane of rotation of the spins. This observation cannot be reconciled with the conventional theory developed for cycloidal multiferroics.

Therefore, $Ba_2CuGe_2O_7$ and $Cu_3Nb_2O_8$ helimagnets can host a number of interesting properties. The study of all these complex phenomena requires

the availability of good single crystals.

Single crystal samples are vital to study the physical properties exhibited by compounds which have high magnetic\ferroelectric anisotropy where significantly different behaviour is seen along different crystallographic directions. In order to outline a complete magnetic diagram, high-quality single crystals are essential.

In the case of $Ba_2MGe_2O_7$ family (with M a transition metal) in literature there are some details on the growth of single crystals by the optical floating-zone technique. However, there was no a full report on growth of $Ba_2CuGe_2O_7$ single crystals up to this work. Also the chemical diagram phase of $Ba_2CuGe_2O_7$ was not reported, thus the synthesis of pure phase and the following crystal growth are open issue.

Recently, helimagnetic $Cu_3Nb_2O_8$ is also investigated but his magnetic phase diagram is not fully described and many questions remain open, i.e. on the microscopic origin of unusual multiferroicity.

Also in this case, the availability of single crystal samples is required for further investigation about magnetic and structural properties.

The most of research on this compound has been done on polycrystalline samples with the exception of only one investigation by Johnson et al. [10] on $Cu_3Nb_2O_8$ single crystals realized by floating zone techinique.

No detail about crystal growth is reported in literature and also for $Cu_3Nb_2O_8$ the chemical phase diagram is not whole known. Thus the search for optimal crystal growth is required to get large and pure single crystal samples.

In this thesis, the investigation of crystal growth conditions of $Ba_2CuGe_2O_7$ and $Cu_3Nb_2O_8$ is presented.

As discussed in Chapter 1, the physical properties of melilite oxides $Ba_2MGe_2O_7$ change with the transition metal ion, thus interesting properties could emerge in mixed melilite oxides [9]. This work investigates two mixed melilite oxides: $Ba_2Cu_{(1-x)}Ni_xGe_2O_7$ and $Ba_2Cu_{(1-x)}Mn_xGe_2O_7$.

In Chapter 1 the main principles of the helimagnetic systems and the most interesting consequences are described. Next Sections describe the melilite oxides and they focus on $Ba_2M(Cu,Mn,Ni,Co,V)Ge_2O_7$ family. Magnetic phase diagram of $Ba_2CuGe_2O_7$ and all properties of this helimagnet are discussed in detail. Finally, $Cu_3Nb_2O_8$ is described and its known properties are discussed.

Chapter 2 is concerned on the growth of large and pure single crystals. First, synthesis of $Ba_2CuGe_2O_7$ polycrystalline powders by different methods is described. Then, the conditions of the single crystal growth are provided. This work carries out the single crystal growth of the helimagnet $Ba_2CuGe_2O_7$ by the floating zone technique, using different gas atmospheres and pressures. The work reports the optimized growth conditions allowing the synthesis of large crystals.

The synthesis of polycrystalline and crystalline samples $Ba_2Cu_{(1-x)}Ni_xGe_2O_7$ and $Ba_2Cu_{(1-x)}Mn_xGe_2O_7$ are discussed. They are grown to investigate the effects on the magnetic properties due to the partial substitution of copper with nickel or manganese in the structure.

The growth conditions of $Cu_3Nb_2O_8$ are shown in the Chapter 2. This thesis sets out in detail about crystal growth of this compound by floating zone using image furnaces with two mirrors and four mirrors symmetry.

Morphological, compositional and structural study on samples is discussed in Chapter 3. By using powder X-ray diffraction and energy dispersive spectroscopy (EDS), the structure and the composition of polycrystalline powders are investigated. Powder X-ray diffraction is also used to check the composition of the grown single crystals. The morphology and chemical composition of the crystals are investigated by scanning electron microscopy (SEM) with wavelength dispersive spectrometry (WDS). Furthermore, the quality of the crystals is studied by rocking curve measurements. The X-ray Laue back reflection and electron backscattered diffraction (EBSD) techniques are used to orient single crystals specifically for selected experiments. Such experiments are illustrated in Chapter 4.

To study the magnetic phase diagrams of grown crystals, magnetization measurement as function of the temperature is performed. Low temperature magnetometry study is performed on oriented single crystal of $Ba_2CuGe_2O_7$ and a magnetic phase below 0.6 K is discussed for the first time.

This work provides also M(T) curves comparison acquired on single crystal of $Ba_2CuGe_2O_7$ and of $Ba_2Cu_{(1-x)}Ni_xGe_2O_7$ for selected crystalline directions. Magnetic measurements are performed on $Cu_3Nb_2O_8$ single crystals, too. This system is one of only two multiferroic known with centrosymmetric triclinic crystal structure with P -1 space group. For the first time, we report magnetization vs temperature data measured along the crystallographic axes of $Cu_3Nb_2O_8$.

While magnetoelectric properties of $Ba_2CuGe_2O_7$ have been extensively discussed in the past, no investigations are reported on its lattice dynamics. The end of the chapter is devoted to the study of lattice dynamics of $Ba_2CuGe_2O_7$ provided by Infra-red and Raman spectra.

Chapter 1

Helimagnetism as a platform for complex magnetic behaviour

Complex oxides exhibit several properties, including magnetism, ferroelectricity, magnetoresistance, which are of great interest among the scientific and technological communities. This dissertation investigates various aspects of helimagnetism. In general, helimagnets are magnets with spins aligned in helical order at low temperature.

A variety of complex magnetic phases with spins forming helical or conical spirals, as well as magnetic vortices, are due to the competition among ferromagnetic exchange, Dzyaloshinskii-Moriya (DM) interaction and magnetic anisotropy [19].

In this chapter, the main properties of the helimagnetic systems are introduced and the most interesting consequences are described briefly. For example, some helimagnetic systems show a magnetically-induced ferroelectricity. The sign of the electric polarization depends on the helicity (direction of rotation of spin), while the direction of polarization depends on further details of the helical order and the underlying lattice symmetry.

This work focuses on two systems: the $Ba_2CuGe_2O_7$ and the $Cu_3Nb_2O_8$, where electric polarization arises from different mechanisms of magnetic interaction. In the following of this chapter, their crystalline and magnetic structures are discussed.

1.1 Magnetic structures

Magnetic materials have a microscopic structure for arrangement of atomic magnetic moments. This is called the *magnetic structure*. A magnetic structure describes the arrangements and symmetry of spins in a crystal lattice. The magnitude and direction of the spin on each magnetic atom site is specified [20]. The magnetism is a dynamic process involving spin waves so the magnetic structure is a *static approximation* of magnetic moments configuration in the lattice.

Below, the Fourier representation of the magnetic structure is introduced and the magnetic structures in solids are illustrated briefly. A full discussion is complex and it is beyond the aim of this work, however further details are well illustrated in the reference [21].

The magnetic structure is characterized by the magnetic moment density which is given by $\mathbf{M} = \langle \psi^\dagger(\mathbf{r}) \mid \mathbf{m} \mid \psi(\mathbf{r}) \rangle$, where $\psi(\mathbf{r})$ is the field operator of electrons and $\mathbf{m}$ denotes the magnetic moment for an electron.

In a crystalline system, the space is divided into the Wigner-Seitz cells for each atom. A magnetic moment of atom i, $\mathbf{m}_i$, is defined as the integral of $\mathbf{M}(\mathbf{r})$ on the i-th atom. The integration is over the Wigner-Seitz cell belonging to atom i. In the case of the crystalline system, the atomic position $\mathbf{R}_i$ is expressed by using the primitive translational vectors $\boldsymbol{a}, \boldsymbol{b}, \boldsymbol{c}$ as $\mathbf{R}_i = i_1 \mathbf{a} + i_2 \mathbf{b} + i_3 \mathbf{c}$. The atomic magnetic moment is expanded with use of the Fourier lattice series, $\mathbf{m}_i = \sum_q \mathbf{m}(\mathbf{q}) e^{(i\mathbf{q}\mathbf{R}_i)}$, where m(q) are Fourier components of the magnetic moments defined in terms of the wave vector $\mathbf{q}$ in the first Brillouin zone. Moreover, we assume that there is only one atom per unit cell. The microscopic magnetic structure of magnetic materials is specied by a set of $\mathbf{m}(\mathbf{q})$.

The ferromagnetic structure is the simplest structure where all of the atomic magnetic moments have the same direction. It is realized when all the Fourier components vanish except $\mathbf{m}(\mathbf{q} = 0) = \mathbf{m}$.

The antiferromagnetic structure is defined by alternative arrangement of the atomic magnetic moments along a direction, e.g., the z direction. The structure is specified by a set, $\mathbf{m}(\pm\mathbf{Q}) = \mathbf{m}\mathbf{k}e^{(\pm i\alpha)}$ and $\mathbf{m}(\mathbf{q} = \pm\mathbf{Q}) = 0$, where $\mathbf{Q}$ consists of half a reciprocal lattice vectors, and $\mathbf{k}$ denotes a unit vector along the z axis, and α denotes a phase of the structure. In the case $\alpha = 0$, then $\mathbf{m}_i = \mathbf{m}\mathbf{k}\cos(\mathbf{Q} \cdot \mathbf{R}_i)$. Therefore, when the position $\mathbf{R}_i$ moves along $\boldsymbol{Q}$ vector, $\mathbf{Q} \cdot \mathbf{R}_i$ changes by π. Accordingly, the magnetic moment $\mathbf{m}_i$ changes its sign.

When the periodicity of the spins follows the crystal structure, the antiferromagnetic order is called *commensurate* [22].

The AF structure on the simple cubic lattice as shown in Fig. 1.1(a) is expressed by the wave vector $\mathbf{Q} = \frac{(1,1,1)\pi}{a}$, a being the lattice constant.

The AF structure on the body-centered cubic lattice as shown in Fig. 1.1(b) is expressed by the wave vector $\mathbf{Q} = \frac{(0,0,1)2\pi}{a}$.

In the case of the face-centred cubic lattice (fcc) structure, two kinds of AF structures are known. The AF structure of the first-kind as shown in Fig. 1.1(c) is described by a wave vector $\mathbf{Q} = \frac{(0,0,1)2\pi}{a}$. The atomic moment alternatively changes the direction with a translation by $\frac{(0,0,1)a}{2}$. It is also possible to change direction alternatively along (1,1,1) axis. This is referred as the AF structure of the second-kind, and it is characterized by $\mathbf{Q} = \frac{(1,1,1)\pi}{a}$ (Fig. 1.1(d)).
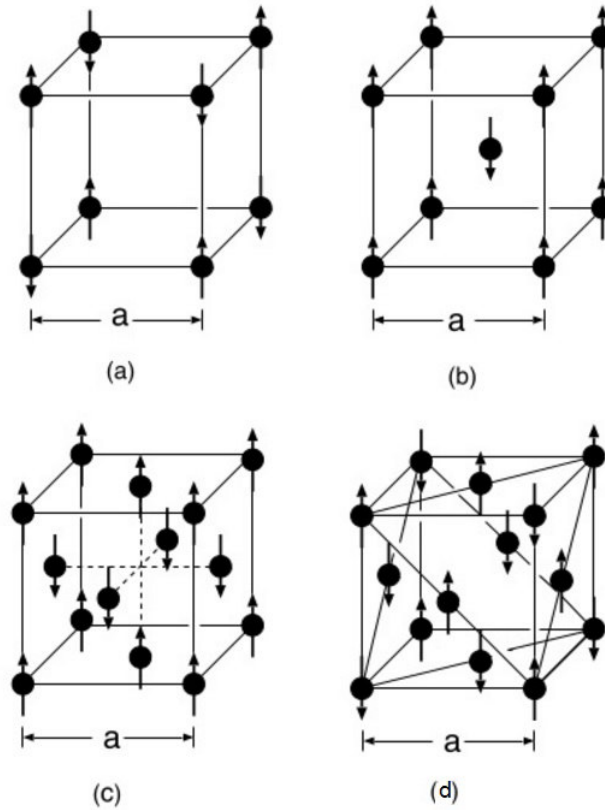
Figure 1.1: Antiferromagnetic arrangements on (a) the simple cubic (sc) lattice, (b) body-centred cubic (bcc) lattice, (c) face-centred cubic (fcc) lattice, (d) the antiferromagnetic structure of the second-kind on the face-centred cubic lattice. The lattice constants are shown by a. [21]

A more complex magnetic ordering shows sinusoidal spin density wave (SDW) structure (Fig. 1.2 (a)). This kind of magnetic ordering is described by $\mathbf{m}_i = m\mathbf{k}\sin(\mathbf{Q} \cdot \mathbf{R}_i + \alpha)$, where $\boldsymbol{Q}$ vector is neither equal to 0 nor to the AF wave vectors. The magnetic moment sinusoidally changes with a period λ along the $\boldsymbol{Q}$ direction. The period of magnetic structure is not necessarily commensurate with the lattice spacing, in general. In this case, the magnetic structure is called *incommensurate.*

It is also possible that the magnetic moment rotates with a translation (see Fig. 1.2(b)). This is known as *helical* structure, and is expressed by:

$$\mathbf{m}_i = m(\mathbf{e}_1 \cos(\mathbf{Q} \cdot \mathbf{R}_i + \alpha) + \mathbf{e}_2 \sin(\mathbf{Q} \cdot \mathbf{R}_i + \alpha)) \tag{1.1}$$

Here $\mathbf{e}_1$ and $\mathbf{e}_2$ are the unit vectors being orthogonal to each other. The magnetic moment with amplitude m rotates on the $\mathbf{e}_1 - \mathbf{e}_2$ plane with the translation along the $\boldsymbol{Q}$ vector.

The conical magnetic structure is shown in Fig. 1.2 (c). The magnetic moment rotates for example on the x-y plane when the moment translates along the direction of $\boldsymbol{Q}$.

In this case, the magnetic structure is described by:

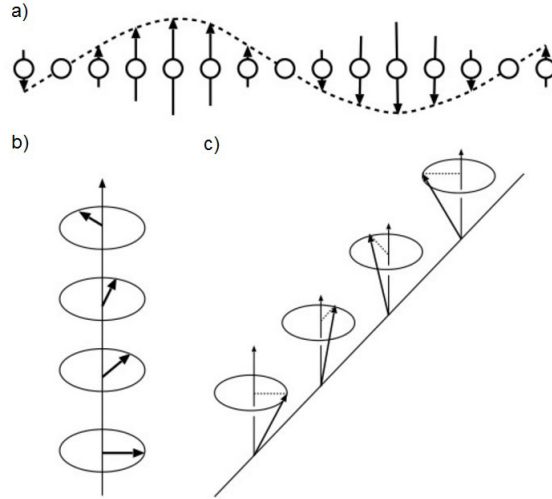$$\mathbf{m}_i = m_z\mathbf{k} + \mathbf{m}(\mathbf{i}\cos(\mathbf{Q} \cdot \mathbf{R}_i + \alpha) + \mathbf{j}\sin(\mathbf{Q} \cdot \mathbf{R}_i + \alpha)) \tag{1.2}$$

Figure 1.2: a) Spin density wave structure b) Helical structure c) Conical structure [21]

The origin of magnetic order in a material takes place because of the different interactions between magnetic moments. The main one is the

exchange interaction between two spins. It is a purely quantum mechanical term proportional to the dot product of the corresponding spin operators. Such interaction between neighbouring spins $\boldsymbol{S}_i$ and $\boldsymbol{S}_j$ is described by the Heisenberg model, with the Hamiltonian given by:

$$\mathbf{H}_{ex} = -\sum_{i,j} J_{i,j}\mathbf{S}_i \cdot \mathbf{S}_j \qquad (1.3)$$

The value $J_{i,j}$ is the exchange constant and describes the nature of the interaction between $\boldsymbol{S}_i$ and $\boldsymbol{S}_j$. If $J_{i,j}$ is positive, neighbouring spins favour a parallel alignment, and the system is ferromagnetic. If $J_{i,j}$ is negative, neighbouring spins favour an antiparallel alignment and the system is antiferromagnetic.

The exchange interaction is a direct result of the Pauli exclusion principle, which forbids fermions with the same spin to exist in the same position and time and of the electrostatic Coulomb repulsion. The exchange interaction requires the overlap of electron orbitals and it is therefore a short range effect. Chiral magnets are a particular type of non-collinear magnet that deserve a special mentioning, indeed helimagnetic structure belong to this class. Systems with lattice lacking inversion symmetry, develop in addition to the exchange interaction a Dzyaloshinskii-Moriya (DM) interaction [12, 13, 14]. This interaction is chiral, thus one direction is preferred. The DM interaction tries to destabilise the collinear antiferromagnetic state ($\rightarrow\leftarrow$) and can introduce a canting of two magnetic moments at different sites ($\searrow\nwarrow\nearrow$) or ($\nearrow\nwarrow\searrow$), with one of which having a lower energy than that original collinear state ($\rightarrow\leftarrow$).

Consistent with the periodic lattice of the crystal the ground state for most of the known chiral magnets corresponds to a spiral state. The periodicity of the spiral is given by an interplay between the DM interaction and the Heisenberg exchange. Of course, spiral states may also be supported in non-chiral magnets. In that case, they can result from competing Heisenberg exchange interactions between different neighbours or are due to geometrical frustration.

In 1957 Dzyaloshinskii [12] predicted on the basis of symmetry arguments the presence of a unidirectional magnetic interaction of the form:

$$\mathbf{H}_{DM} = \mathbf{D}_{i,j} \cdot (\mathbf{S}_i \times \mathbf{S}_j) \qquad (1.4)$$

where $\boldsymbol{D}_{i,j}$ is known as DM vector. DM interaction results from relativistic spin orbit corrections to the ordinary superexchange mechanism and therefore is weak when compared to antiferromagnetic symmetric exchange [22].

1.2 Helimagnetism

Helimagnetic phases are also referred as *spiral magnetic order*, generally distinguished between *helical* and *cycloidal* arrangements of the magnetic moments, where in a helical spiral the moments rotate in a plane perpendicular to the propagation vector while in a cycloidal spiral the propagation vector lies within the rotation plane of the spins.

The most well-known helimagnet is manganese silicide (MnSi). This compound is a cubic crystal with space group $P2_13$. MnSi shows a helical spin structure below the temperature 30 K (Fig. 1.3) [1, 2, 3, 4].
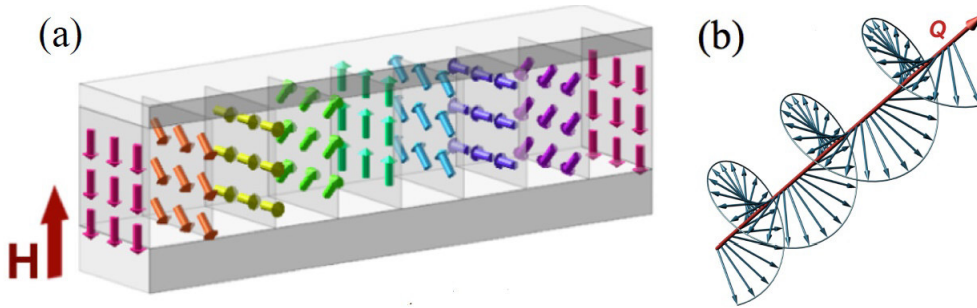
Figure 1.3: a)Magnetic ordering in a helimagnet. On each plane, there is a ferromagnetic order, but the direction of magnetization rotates along the helical direction. The arrow denotes the direction of the helix. b) Diagram of helimagnetic structure.[23]

Such helical order can be explained by the DM mechanism [12, 14] due to spin-orbit coupling [24] and to lack of spatial inversion symmetry in lattice structure. The helimagnetic pattern is shown in Fig. 1.3. There is ferromagnetic order on any given plane perpendicular to the helix, and the direction of the magnetization rotates along the direction of the helix. The helix is characterized by $\boldsymbol{Q}$ vector, indicating the direction of the helix. The $\boldsymbol{Q}$ modulus is the helical wavenumber, where $\frac{2\pi}{Q}$ is the helical wavelength, describing the distance that the ferromagnetic order repeats itself.

Fig. 1.4 shows magnetic phase diagrams of MnSi (Fig. 1.4 (a)), $Fe_{0.8}Co_{0.2}Si$ (Fig. 1.4 (b)), $Fe_{0.5}Co_{0.5}Si$ (Fig. 1.4 (c)) and FeGe (Fig. 1.4 (d)). These systems have different chemistry and structure; however, the magnetic phase diagrams show similar features. Indeed, for low magnetic fields and below definite critical temperatures, all systems are helimagnetic. This magnetic order is the platform through which more complex magnetic behaviours arise for increased magnetic fields and higher temperature.

At the lowest temperature and for small magnetic applied field all phase diagrams show a helical phase. For MnSi and $Fe_{0.8}Co_{0.2}Si$ this phase is indicated as *helical*, while for $Fe_{0.5}Co_{0.5}Si$ and FeGe this phase is indicated as *H*.

Increasing the magnetic field, different behaviours are observed in the mentioned systems. For MnSi, at T<30K and for H>0.6 T, a *field polarized* phase is observed. Instead, for $Fe_{0.8}Co_{0.2}Si$ at T<30K and for 0.6<H<1.5 T a *conical* phase is observed. For FeGe the conical phase is observed at T<278K and 0.1<H<0.3 T.

All phase diagrams show a *skyrmion phase*. Magnetic skyrmions are particle-like nanometre-sized spin textures of topological origin found in several magnetic materials, and they are characterized by a long lifetime [25]. As will be discussed in section (1.3.2), skyrmions are observed both by means of neutron scattering in momentum space and microscopy techniques in real space. A skyrmion appears as a vortex-like spin texture in a chiral-lattice magnet.

In MnSi the skyrmions are observed at $T \sim 30$ K. In magnetic phase diagram (Fig. 1.4 (a)) this region is indicated as *A phase*. Muhlbauer et al. observed the skyrmions for the first time in MnSi [26]. The neutron beam is parallel to the applied magnetic field, and the magnetic phase exhibits six fold symmetry, as shown in Fig. 1.5 (a). This configuration is a two-dimensional (2D) hexagonal periodic structure on a plane which is perpendicular to the applied magnetic field.

Also in $Fe_{0.8}Co_{0.2}Si$ skyrmions are observed as shown in (Fig. 1.4 (b)). This region is indicated as *A phase* at $T \sim 30$ K.

The region of skyrmions is very wide for $Fe_{0.5}Co_{0.5}Si$, it is indicated as *SkX* in Fig. 1.4 (c). Around this region, mixed phases of skyrmion and helix ($H + Sk$) and of skyrmion and ferromagnetism ($H + FM$) are observed.

In FeGe different phases of skyrmions are observed. There are several possible types of skyrmion structure corresponding to different values of vorticity m and helicity γ, as defined in reference [25]. In magnetic diagram phase of FeGe different types of skyrmions are observed when the temperature and the magnetic field increase. Thus, in the phase diagram of FeGe (Fig. 1.4 (d)) the regions of skyrmions are indicated as A_0, A_1, A_2 and A_3.
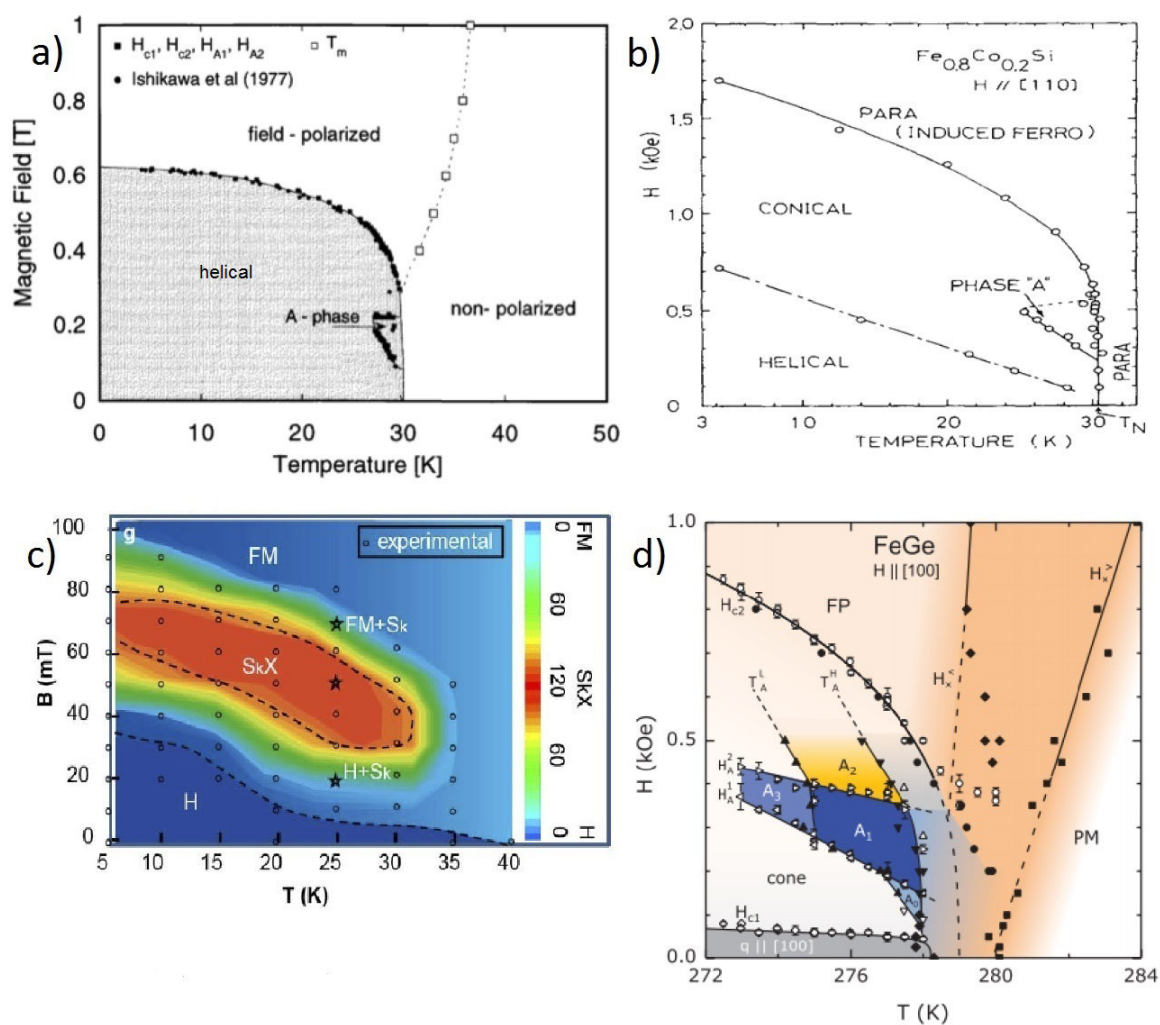
Figure 1.4: Magnetic phase diagram of a)MnSi [5] b)Fe$_{0.8}$Co$_{0.2}$Si [6] c)Fe$_{0.5}$Co$_{0.5}$Si [7] d)FeGe [8].
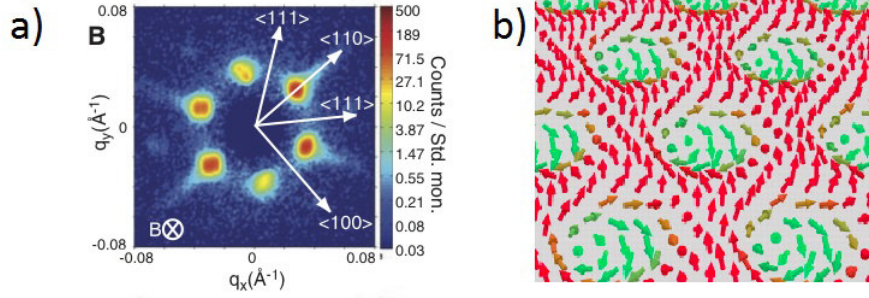
Figure 1.5: a) Neutron scattering data in the columnar phase of MnSi. The applied magnetic field is perpendicular to the paper. The six-fold pattern implies the two-dimensional hexagonal columnar structure. b)A hexagonal lattice of Skyrmions in the columnar phase of MnSi [26]

1.3   Interesting consequences of helimagnetism

### 1.3.1   Multiferroics of spiral spin origin

The frustration in spin exchange interactions as well as the Dzyaloshinskii-Moriya (DM) interaction on non-centrosymmetric lattice can often produce the helical spin structure. Among them, the transverse-spiral (cycloidal) structure in an insulating magnet can almost always produce the ferroelectricity whose polarization direction depends on the vector spin chirality. Even for the case of the longitudinal-spiral or proper screw structure, the coupling of such a spin texture to the underlying chemical lattice can produce the ferroelectric polarization via the spin-orbit interaction.

The magnetically flexible spin structure immediately leads to the magnetic control of the ferroelectric polarization vector, both in magnitude and direction.

A material that combine more ferroic properties is called multiferroic [27]. Main three ferroic properties are ferroelectricity, ferromagnetism, and ferroelasticity. Similarly to a ferromagnet, a ferroelectric material shows a spontaneous electric polarisation P that can be switched by an applied electric field E, while a ferroelastic material displays a spontaneous deformation that can be reversed by an applied mechanical stress [28]. The most interesting multiferroics exhibit a strong correlation of magnetism and ferroelectricity (Fig. 1.6).

The prospect of controlling magnetic moment M (dipole moment P) by applied voltages (by applied magnetic fields) drives the research for these

innovative materials to built new forms of multifunctional devices.
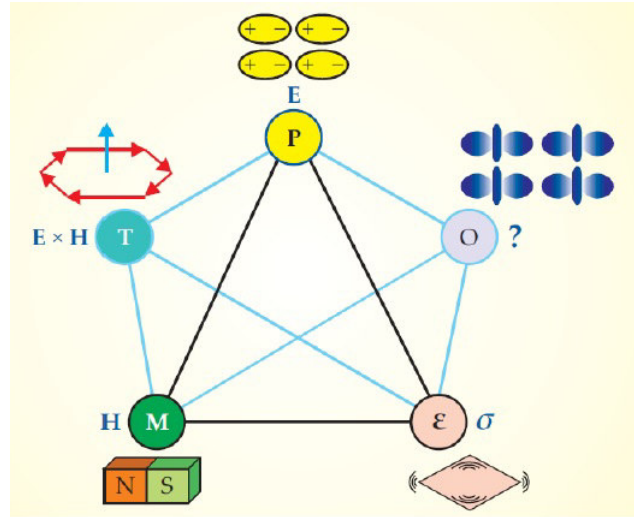
Figure 1.6: Interactions in multiferroics. The primary ferroic orderings (ferro-electricity ($\boldsymbol{P}$), ferromagnetism ($\boldsymbol{M}$), and ferroelasticity (ε)) can be switched by electric ($\boldsymbol{E}$), magnetic ($\boldsymbol{H}$), and stress (σ) fields, respectively. Multiferroic coupling allows to drive those ferroic orderings by others fields. Physicists are also exploring the possibility of ferro-toroidics, a promising new ferroic ordering of toroidal moments ($\mathbf{T}$), which should be switchable by crossed electric and magnetic fields. The O represents other possibilities such as spontaneous switchable orbital orderings, vortices, and chiralities that will likely enrich future research [29]

Various types of spin order can have a potential to break the inversion symmetry and produce a spontaneous (ferroelectric) $\mathbf{P}$. This is valid for both collinear and non-collinear forms of magnetic order, when they are placed on some specific lattice geometry.

Rather lattice-form-independent mechanisms for the magnetically induced ferroelectricity are found for versatile compounds with spiral spin orders, as depicted in Figure 1.7. When the spins on the adjacent atomic sites are mutually canted, the horizontal mirror-plane symmetry is lost, resulting in the possible generation of a polarization along the vertical direction [30, 31, 32]. Transverse screw spin configurations, such as cycloidal and transverse-conical spin orders (Fig. 1.7 (b),(d)), can always produce spontaneous $\mathbf{P}$ irrespective of magnetic modulation vectors. When the spins form a transverse-spiral (cycloidal) modulation along a specific crystallographic direction, every nearest-neighbor spin pair produces a unidirectional local $\mathbf{P}_{ij}$ and, hence, the

Compound	Structure	Magnetic Order	$\mathbf{P}(\mu Cm^{-2})$	Ref.
$RMnO_3$	Orthorhombic (mmm)	Cycloidal	≤ 2000	[38]
$CuFeO_2$	Rhombohedral ($-3m$)	Screw	~ 300	[39]
$CoCr_2O_4$	Cubic ($m3m$)	Conical	~ 2	[40]
$MnWO_4$	Monoclinic ($2 \backslash m$)	Cycloidal	~ 60	[41, 42]

Table 1.1: List of magnetoelectrics related to spiral spin structure.[11]

macroscopic $\mathbf{P}$ of electronic (spin) origin should be generated. The direction of the polarization can be expressed with equation $\mathbf{P}_{ij} = a\Sigma_{i,j}\mathbf{e}_{ij} \times (\mathbf{S}_i \times \mathbf{S}_j)$. Here, $\mathbf{e}_{ij}$ is the unit vector connecting the neighboring spins $\mathbf{S}_i$ and $\mathbf{S}_j$, and the proportional constant a is determined by the spinorbit and spin-exchange interactions as well as the possible spin-lattice coupling term. The sign of $\mathbf{P}$ depends on a clock-wise or counter-clock-wise rotation of the spin (called spin helicity) in proceeding along the spiral propagation axis. The model was termed the spin-current model (Katsura-Nagaosa-Balatsky model) on the basis of the above-mentioned duality analogy or the inverse Dzyaloshinskii-Moriya (DM) model.

Most of the magnetically induced multiferroics exhibit a spiral magnetic structure (Tab 1.1). The magnetic order in these system is highly frustrated and competing interactions between the magnetic moments lead to complex magnetic structures [30, 31, 32, 33, 34, 35, 36, 37]. For that reason the ordering temperature in these compunds is rather low.

Two spins of neighboring sites can couple through different ways generating an electric moment dipole, when the sum over the crystal lattice sites is not cancelled, the macroscopic $\mathbf{P}$ survives.

Mainly, there are three mechanisms of ferroelectricity of spin origin [11]:

Symmetric spin exchange interaction, $P_{ij} \propto \Pi_{ij}(\mathbf{S}_i \cdot \mathbf{S}_j)$. It works between the neighboring spins $\mathbf{S}_i$ and $\mathbf{S}_j$ and induces striction along crystallographic direction Π_{ij}.

Inverse Dzyaloshinskii Moriya (DM) interaction, $P_{ij} \propto \mathbf{e}_{ij}(\mathbf{S}_i \times \mathbf{S}_j)$ .It is an antisymmetric spin exchange interaction between canted spins $\mathbf{S}_i$ and $\mathbf{S}_j$ where $\mathbf{e}_{ij}$ is a unit vector linking two sites.

Spin ligand interaction ($p-d$ hybridization), $P_{ij} \propto (\mathbf{S}_i\mathbf{e}_{ij})^2\mathbf{e}_{ij}$. This mechanism is caused by the variation of hybridization between transition
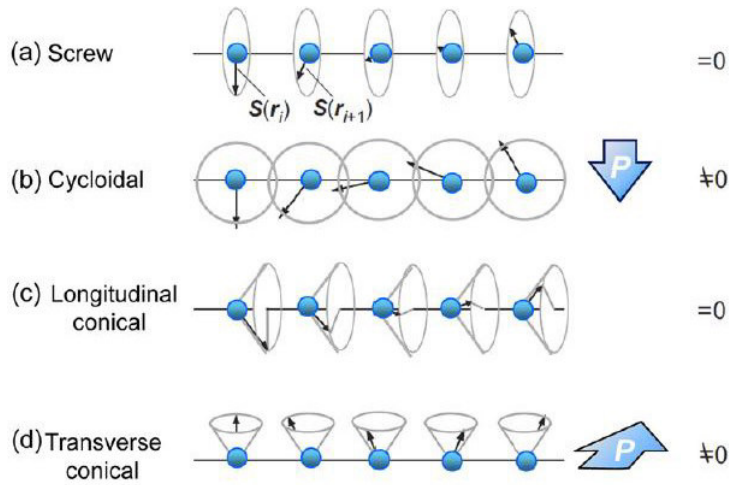
Figure 1.7: Schematic illustrations of types of spiral magnetic structure on a one-dimensional array of magnetic moments $\mathbf{S}(\mathbf{r})$. They include (a) proper screw, (b) cycloidal, (c) longitudinal-conical, and (d) transverse-conical magnetic structures. [11]

metal d orbitals and ligand p orbitals. In this case a single spin moment is essential for the origin of the electric moment between two ions.
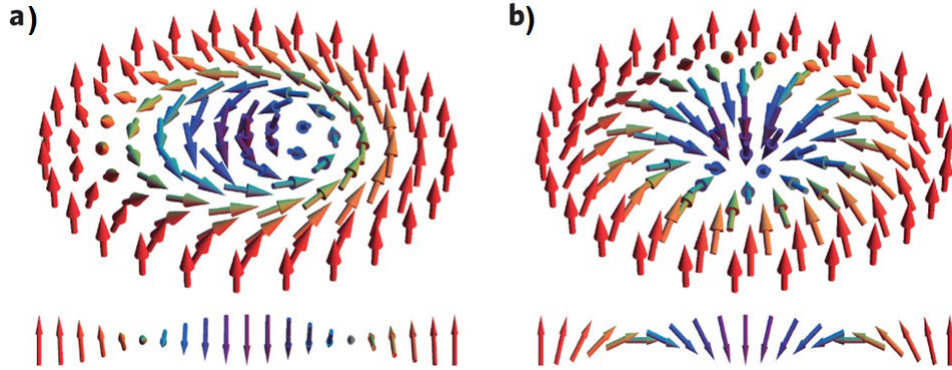
1.3.2   Skyrmions

In the section 1.2, magnetic phase diagrams of some helimagnetic systems are discussed and they show a magnetic phase of skyrmions. As mentioned, magnetic skyrmions are particle-like nanometre-sized spin textures of topological origin found in several magnetic materials, and they are characterized by a long lifetime [25].

A skyrmion is a non-collinear magnetic structure where the magnetic moments point towards the centre (in a similar way to vortex type structures of superconductors). There are several possible types of skyrmion structure, corresponding to different values of vorticity m and helicity γ [25]. An example of two types of skyrmions is shown in Fig. 1.8, where Bloch and Neel type skyrmions are illustrated.

Theory predicts that these topological magnetic structures appear only in non-centrosymmetric structures [25]. The crystal structure of the prototype, MnSi, is the cubic B20 structure with the chiral space group $P2_13$ [44], as already mentioned, it exhibits a rich magnetic phase diagram that represents

the typical phase diagram of a skyrmion system (Fig. 1.9).

Figure 1.8: a) In a Bloch-type skyrmion, the spins rotate in the tangential planes, that is perpendicular to the radial directions when moving from the core to the periphery. b) In a Neel-type skyrmion, the spins rotate in the radial planes from the core to the periphery. The cross-section of the vortex is also depicted in both cases [43].

Skyrmions are found in metallic ($Fe_{1-x}Co_xSi$ [7, 45], FeGe [46]) as well as in insulating (Cu_2OSeO_3 [47]) compounds through Lorentz transmission electron microscopy.

To identify a skyrmion lattice many experimental techniques are used. For example, a non-collinear magnetic structure can be identified by neutron diffraction. Moreover, both specific heat and susceptibility measurements are useful to give information to the magnetic phase diagram containing skyrmions. Finally, real space methods as spin polarized scanning tunnelling microscopy, magnetic force microscopy, scanning Hall microscopy, and Lorentz transmission electron microscopy and the reciprocal space method small angle neutron scattering can be used to investigate the skyrmion lattice.

Various mechanisms can generate skyrmions in magnetic systems, and multiple mechanisms often contribute simultaneously [25]. The first one is due to the long−ranged magnetic dipolar interactions. In magnetic thin films with perpendicular easy-axis anisotropy, the dipolar interaction favours an in-plane magnetization, whereas the anisotropy prefers an out-of-plane magnetization. The competition between these two interactions results in periodic stripes in which the magnetization rotates in the plane perpendicular to the thin film. An applied magnetic field perpendicular to the film turns the stripe state into a periodic array of skyrmions [48]. Skyrmions are typically of the order of 100 nm to 1 μm, which is comparable to the period λ of the spiral.

The second mechanism is the relativistic Dzyaloshinskii-Moriya interaction.
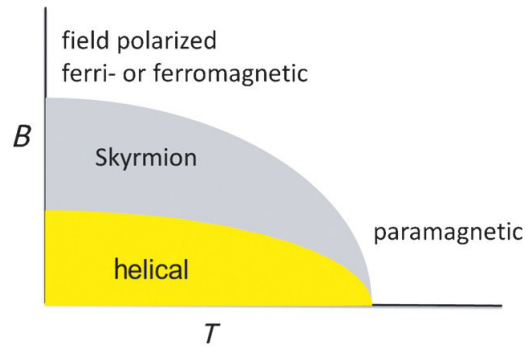
Figure 1.9: Schematic magnetic phase diagram of a compound with a skyrmion ground state. For B=0, helimagnetic order develops below a critical temperature (yellow area). Above a critical field the helical order collapses. In MnSi the skyrmion phase appears only in a small area; in thin films the skyrmion phase is observed for intermediate fields and low T (grey area). At high magnetic fields a collinear interaction is induced and at high temperatures the systems become paramagnetic.

In this case, an analogous transformation from the helical spiral into the triangular-lattice skyrmion crystal under an external magnetic field occurs. In this case, the size is determined by the DM interaction and is typically 5 100 nm.

The third mechanism is due to the frustrated exchange interactions [49]. The skyrmion size is of the order of the lattice constant.

The last mechanism consists of four-spin exchange interactions. Also in this case the interaction can lead to atomic-sized skyrmion structures [50].

While the first mechanism was extensively studied in the 1970s aiming at applications for magnetic memory devices, the other cases are a focus of intensive research now.

It is known that non-centrosymmetric crystal classes can exhibit many interesting physical and technologically properties such as piezoelectricity, ferroelectricity, and pyroelectricity, and second-order nonlinear optical behaviour. The combination of one of these properties with helical magnetism in non-centrosymmetric compounds might open new directions for compounds with multifunctional properties.

In the context of future spintronic applications skyrmions might have an enormous impact [15]. For example, applications of skyrmions can control the magnetoresistance (electric current) by the magnetization in read heads of hard disks based on the GMR effect.

Skyrmions, which can be manipulated by current low densities and small magnetic fields in the mT range can open new directions for MRAM research,

but also for racetrack memory, in which magnetic domain walls are moved by an electrical current. Also, here small skyrmions could have an impact on reducing the energy consumption. Another direction in spintronic is the use and manipulation of a pure spin current, a current without charge transport [47].

1.4 Melilite Oxides

It is well known that non-centrosymmetric tetragonal antiferromagnets can host a number of interesting properties. The helimagnet $Ba_2CuGe_2O_7$ is one notable example. Part of this work is focused on this system, as will be shown in following chapters. $Ba_2CuGe_2O_7$ is a melilite oxide. Below, main properties of these compounds are discussed.

A local origin of magneto-electric coupling in low-symmetry crystals through a spin-dependent hybridization mechanism attracts interest of intense research activity, which has recently expanded to include materials with complex structures [33].

One possibility is offered by layered transition-metal oxides since of interesting magnetic and electronic properties and their low-dimensional characteristics. Melilite oxides have the general formula $A_2MN_2O_7$ (where A is larger cations, for example alkali earth and lanthanide ions; M, N is smaller divalent to tetravalent ions) and typically show a tetragonal structure (space group $P-42_1m$) with a unit cell of $a \sim 8$ Å and $c \sim 5$ Å.

The schematic crystal structure of the compounds is illustrated in Figure 1.10. This pseudo layered structure consists of two-dimensional blocks perpendicular to the c-axis, formed by N_2O_7 dimers linked to MO_4 tetrahedra; these blocks are separated by A sheets.

Crystal sample are realized by different techniques. For example, $Ba_2MgGe_2O_7$ and $Ba_2ZnGe_2O_7$ are grown by the top seeded solution growth technique [51, 52], $Sr_2ZnGe_2O_7$, $Sr_2MgGe_2O_7$, $Ba_2ZnGe_2O_7$ and $Ba_2MgGe_2O_7$, are grown using the Czochralski method [53, 54].

The melilite type oxides show a variety of magnetic properties,[55, 56] as listed in Table 1.2. For example, $Ba_2MGe_2O_7$ (M = Mn, Co, Cu) shows the 2D antiferromagnetic behaviour due to the square planar arrangement of the magnetic M ions. At low temperature, these compounds show different behaviours. In $Ba_2MnGe_2O_7$ an antiferromagnetic transition is observed [57] for $T < 4.6K$, while in $Ba_2CoGe_2O_7$ a multiferroic behaviour is observed, which derived from antiferromagnetic-ferroelectric transitions under the magnetic field[57, 58]. Finally, in $Ba_2CuGe_2O_7$ an incommensurate-commensurate magnetic transition followed by a spiral antiferromagnetic ordering are observed

[59].

Moreover, by introducing further magnetic ions into the M and A sites, the spin−glass behaviour in $Ba_2Fe_2GeO_7$ [60, 61] and ferrimagnetic ordering between Eu^{2+} and Mn^{2+} moments in $Eu_2MnSi_2O_7$ are found [55].

$Sr_2MGe_2O_7$ compounds (with M = Co, Mn) are isostructural to the barium analogues; the substitution of Sr for Ba at the A site should shorten the MM distance along the c axis. This may change the relationship between the intralayer and interlayer magnetic interactions in the melilites.
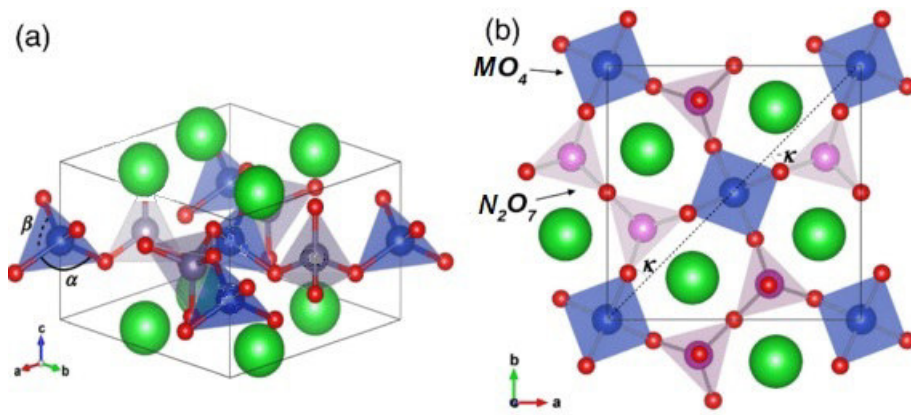
Figure 1.10: Melilite crystal structure of $A_2MN_2O_7$ with $P−42_1m$ symmetry, showing layers of N_2O_7 dimers linked by MO_4 tetrahedra intercalated by A ions. The MO_4 tetrahedra are compressed along the c axis, resulting in different O-M-O angles α, β. (b) Top view of the crystal structure, highlighting two inequivalent MO_4 tetrahedra which are rotated about the c axis of k, respectively.

1.5 The Family of $Ba_2MGe_2O_7$

Among melilite oxides, this work focuses on the class of $Ba_2MGe_2O_7$ (BMGO) materials with M belonging to the row of $3d$ transition metals.

In literature, for system with M = Cu, Co, Mn a study of magnetoelectric properties is reported [9] while Jahn-Teller distortions are investigated in system with M = Ni, V. The synthesis of material with M = Ni, V is not reported in the literature, while a detailed study is discussed in ref. [65] about distortions of crystalline system caused by effects of introduction of Ni and V ions. As will be discussed in following, in compounds with M = Cu,

Compound	T_C (K)	magnetic properties	Ref.
$Sr_2MnSi_2O_7$	3.4	antiferromagnet	[55]
$Ca_2CoSi_2O_7$	5.7	antiferromagnet	[62]
$Sr_2CoSi_2O_7$	7	antiferromagnet	[62]
$Sr_2MnGe_2O_7$	4.4	antiferromagnet	[63]
$Sr_2CoGe_2O_7$	6.5	antiferromagnet	[63]
$Ba_2MnGe_2O_7$	4.6	2D AFM	[57]
$Ba_2CoGe_2O_7$	6.7	2D AFM	[58]
$Ba_2CuGe_2O_7$	3.2	2D spiral AFM, transition IC	[64]
$Ln_2GeBe_2O_7$	>5	Ln = Y, La, Pr, Sm, Gd, Dy; paramagnet	[56]
$Eu_2MgSi_2O_7$	>1.8	paramagnet	[55]
$Eu_2MnSi_2O_7$	10.7	ferrimagnet	[55]

Table 1.2: Magnetic Properties of Melilite-Type Oxides

Co, Mn electric polarization arises as result of $d-p$ hybridization mechanism between transition metal d orbital and ligand p orbitals, while for system with M = Ni, V an electric polarization is expected due to the combination of Jahn-Teller distortions and $d-p$ hybridization.

BMGO shows tetragonal non centrosymmetric (but non polar) $P-42_1m$ (n.113) structure with two M sites, M_1 at $(0,0,0)$ and M_2 at $(\frac{1}{2},\frac{1}{2},0)$.

These compounds show magnetoelectric properties originating from the spin-dependent hybridization between d orbitals of transition metal M and ligand oxygen p orbitals. Other examples of such mechanism are found in $CuFeO_2$ [39] and in $CuCrO_2$ [66], but the number of materials showing the ferroelectricity due to the $d-p$ hybridization mechanism is still limited.

In the $d-p$ hybridization mechanism, the ionic charge at the ligand site (Δe) varies as $\Delta e \propto (\mathbf{S} \cdot \mathbf{r})^2$, where $\mathbf{r}$ is the vector connecting the transition metal and ligand ions, owing to the spin-orbit interaction. As a result, the local electric dipole moment $\mathbf{P} \propto (\mathbf{S} \cdot \mathbf{r})^2\mathbf{r}$ is induced along the bonding direction. Applying these fundamental relations in the case of MO_4 tetrahedron, a model for electric polarization is obtained and it is confirmed by experimental results as reported in [9].

The electronic structure of BMGO is strongly influenced by the local tetrahedral crystal field experienced by d electrons on the M ions causing a splitting between lower two-fold degenerate e_g states and higher three fold t_{2g} states. Figure 1.11 shows the electronic structure of the transition metal d orbital state for BMGO with M = Mn, Co, Cu. For $Ba_2MnGe_2O_7$, the d orbitals of the manganese site shows the high-spin configuration with $S = \frac{5}{2}$ due to the strong Hund's rule coupling. In the case of M = Co^{2+} and Cu^{2+}, $S= \frac{3}{2}$ and

$S = \frac{1}{2}$ states are realized following the Hund's rule as shown.
Below, main physical properties of family BMGO with M =Mn, Co, Cu, Ni and V are discussed.
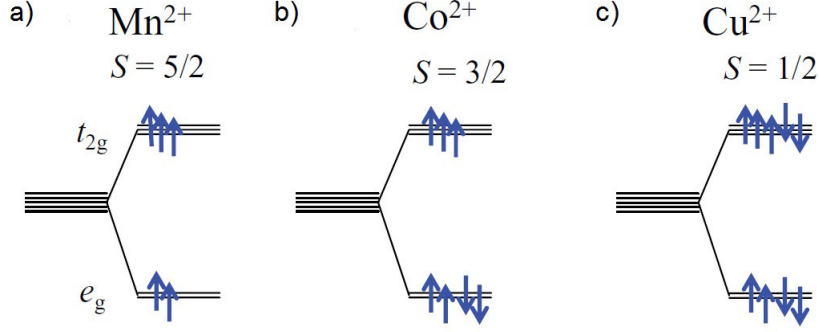
Figure 1.11: The electronic structure of d levels in a) $Ba_2MnGe_2O_7$, b) $Ba_2CoGe_2O_7$, and c) $Ba_2CuGe_2O_7$, respectively.[9]

1.5.1 $Ba_2CuGe_2O_7$

In this section, main properties of $Ba_2CuGe_2O_7$ about crystal structure and its helimagnetism are discussed. However, magnetic behaviour is quite complex, therefore a full discussion is proposed in the next section where magnetic phase diagrams will be shown.

The magnetism of $Ba_2CuGe_2O_7$ is due to $S = \frac{1}{2}$ spins localized on the Cu^{2+} sites. The tetragonal crystal structure is non-centrosymmetric, the lattice constants are $a = 8.466\mathring{A}$, $c = 5.445\mathring{A}$ (Fig. 1.12) [59]. The characteristic feature is a square-lattice arrangement of Cu ions in the (a, b) crystallographic plane with the possibility of super-exchange interactions via the GeO_4 tetrahedra along the diagonals and possibly the sides of the (a, b)-projected unit cell. Adjacent Cu-planes are separated by layers of Ba with no obvious superexchange routes. These structural features suggest that the material may exhibit quasi-2-D behavior and, possibly, competing in plane antiferromagnetic (AF) interactions.

In $Ba_2CuGe_2O_7$ a helical spin structure is observed below $T_N = 3$ K [59], this compound is the alone of BMGO family which shows this magnetic behaviour. The magnetic spiral phase is due to the absence of inversion center which allows the Dzyaloshinskii-Moriya (DM) terms in the Hamiltonian. The helical spin structure [see Fig. 1.13] is realized in $Ba_2CuGe_2O_7$ by the uniform D_{ab}(component of DM vector in (a,b) plane) as the DM-induced modulation of the staggered antiferromagnetic structure.

The electric polarization is observed in $Ba_2CuGe_2O_7$. It is induced by the helical spin structure under the magnetic field up to 5 T [67].

It is found that the spin helicity of the cycloidal spin order is always fixed to the lattice, therefore the magnetic propagation vector $\boldsymbol{k}$ determines the sign of electric polarization in $Ba_2CuGe_2O_7$ [67]. Two types of magnetic domains with orthogonal spin-modulation directions have the opposite spin helicity due to the noncentrosymmetric crystal structure, hence hosting the spontaneous polarization with the opposite directions. Therefore, the ferroelectric single domain can be generated merely by an application of magnetic field without the action of external electric field. Even more importantly, the magnetic $\boldsymbol{k}$ domain can be completely switched by the genuine electric-field stimulation. Measurements of electric polarization (component $\mathbf{P}_c$ [9]) and corresponding $\mathbf{M}$ are performed in the higher magnetic fields up to 14 T at various temperatures. The variations of $\mathbf{P}_c$ are measured in H along the (1,1,0) direction. At the lowest temperature 1.8 K, $\mathbf{P}_c$ shows H^2 dependence in the low-H region and discontinuous change at around 8.7 T.
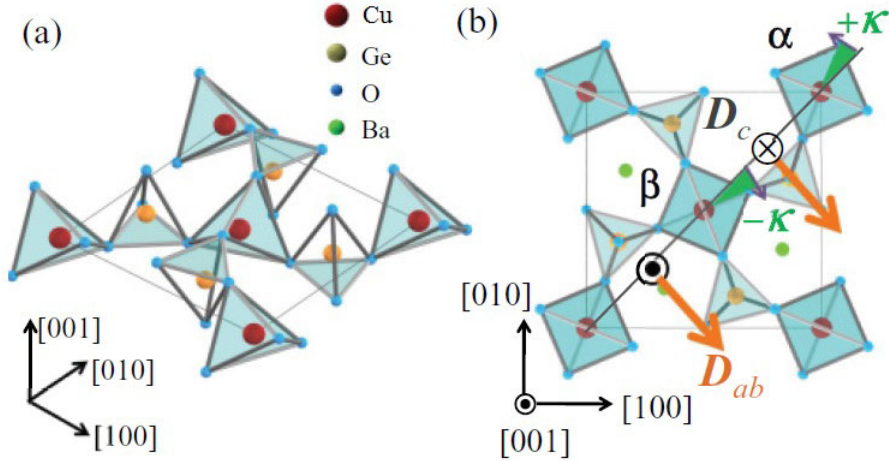
Figure 1.12: (a) Three-dimensional view and (b) top view of the crystal structure of $Ba_2CuGe_2O_7$. Two types of the CuO_4 tetrahedron (α and β) tilt $\pm\kappa$ from the (1,1,0) directions. In-plane and out-of-plane components of the DM vector (D_{ab} and D_c) exist in this crystal structure. [9]

1.5.2 $Ba_2CoGe_2O_7$

In this section, the main features and results of several measurements on $Ba_2CoGe_2O_7$ crystals are summarized briefly.

Crystal structure of $Ba_2CoGe_2O_7$ is very similar to one of $Ba_2CuGe_2O_7$ (Fig. 1.12). The crystal structure is tetragonal P-42_1m with $a = b = 8.3836\mathring{A}$ and $c = 5.5510\mathring{A}$ [68]. Co^{2+} ions carry spin $S = \frac{3}{2}$ and the CoO_4 tetrahedron is distorted along the c direction.

In BMGO family, the magnetic configuration strongly depends on the d electron filling. Only $Ba_2CuGe_2O_7$ shows a spiral antiferromagnet structure below $T_N = 3K$. $Ba_2CuGe_2O_7$ shows a field-induced incommensurate-commensurate (IC) transition, which can be induced also by a partial chemical substitution of the spin carrying Cu^{2+} ions by Co^{2+}.

For all Co concentrations x the solid solution $Ba_2(Co_xCu_{1-x})Ge_2O_7$ orders magnetically. $Ba_2CuGe_2O_7$ ($x = 0$) at $T_N = 3.2$ K shows a helimagnetic spin order while $Ba_2CoGe_2O_7$ ($x = 1$) at $T_N = 6.7$ K exhibits an antiferromagnetic transition and a staggered antiferromagnetic structure in the (0,0,1) plane with slight canting [64]. The antiferromagnetic structure is C-type for $Ba_2CoGe_2O_7$ (Fig. 1.13). A possible explanation is described briefly.

For $x = 0$, in compound the helimagnetic distortion is caused by the in plane component $\mathbf{D}_{ab}$ of the Dzyaloshinskii vector $\boldsymbol{D}$ associated with the same $Cu-Cu$ bonds [64]. This component retains its direction from one bond to the next, and thus favours a spin spiral state [12]. In contrast, the out-of-plane component $\mathbf{D}_c$ is sign alternating and stabilizes a weak ferromagnetic structure. However, for $Ba_2CoGe_2O_7$ Zheludev et al. [58] reported that the strong anisotropy effects push all spins in the system into the (a, b) crystallographic plane. Since in $Ba_2CuGe_2O_7$ the helimagnet-forming uniform component $\mathbf{D}_{ab}$ of the Dzyaloshinskii vector is itself in the (a, b) plane of $Ba_2CoGe_2O_7$, forcing the spins into the (a, b) plane makes the corresponding triple product in the Hamiltonian $\mathbf{D}_{ab} \sim (\mathbf{S}_m \times \mathbf{S}_n)$ vanish. Only the non-helimagnet forming sign-alternating c-axis component of $\boldsymbol{D}$ remains relevant. As a result, the spin structure may be slightly canted, but is, nevertheless, commensurate.

As reported in [69], in $Ba_2CoGe_2O_7$ is discovered the appearance of ferroelectricity below the Neel temperature of $T=6.7K$. The ferroelectric polarization is rather small in magnitude and aligned along the c axis, but its magnitude increases remarkably and its direction rotates away smoothly from the c axis when magnetic fields are applied along the c axis. The electric polarization's behavior of smooth rotation, rather than a sudden flip, is unique. It also accompanies a linear increase in magnetization and a smooth change of dielectric constant with little hysteresis, which may be important for certain technological applications.

As mentioned, this order is due to the mechanism metal-ligand hybridization. It is a single (magnetic) ion effect: when a transition metal is connected to a ligand (with vector $\boldsymbol{e}$), then a polarization of the form $\mathbf{P} \sim (\mathbf{S} \cdot \mathbf{e})^2\mathbf{e}$ develops. In $Ba_2CoGe_2O_7$ the four O-ligands around each Co-ion cooperate to give a

net ferropolarization to the compound.

Other possible mechanisms are not probable. One mechanism is the inverse Dzyaloshinskii-Moriya effect, which is active in helicoidal spin structures, then a polarization $\boldsymbol{P}$ is developed. Since no helicoidal spin structure is present in $Ba_2CoGe_2O_7$ this mechanism is clearly unable to explain the multiferroicity. Another mechanism, the magnetostriction-induced ferroelectricity can be responsible for a developing a ferropolarization, but in $Ba_2CoGe_2O_7$ the structure of the magnetic cell does not support this mechanism.

For further understanding of essential magnetoelectric properties originating from the spin-dependent d-p hybridization mechanism, the magnetic-field dependence of $\mathbf{P}_c$ (component of electric polarization) up to 14 T along (1,1,0) is measured at various temperatures. $\mathbf{P}_c$ decreases with approaching T_N. Even above T_N, the $\mathbf{P}_c$ is finite and shows quadratic magnetic-field dependence.

This is another supporting evidence for the scenario of the spin-dependent d-p hybridization mechanism. Indeed, in this hypothesis $\mathbf{P}_c$ is expected to show the quadratic $\mathbf{H}$ dependence in the high-temperature paramagnetic region, in which $\mathbf{M}$ is proportional to $\mathbf{H}$. Such feature is indeed consistent with experimental observations at T = 20, 50, 100, and 300 K reported in [9].

1.5.3 $Ba_2MnGe_2O_7$

$Ba_2MnGe_2O_7$ shows a tetragonal structure with space group P4-2_1m and lattice parameters with $a =$8.505 $\mathring{A}$ and $c =$5.528 $\mathring{A}$, thus also $Ba_2MnGe_2O_7$ is isostructural to $Ba_2CuGe_2O_7$. MnO_4 tetrahedra linked by GeO_4 tetrahedra forms a square lattice in the crystallographic c plane. The Mn^{2+}-Mn^{2+} distance is 6.014 $\mathring{A}$ which indicates that the exchange constant may be reasonably small. The square lattice is separated by Ba^{2+} ions in the crystallographic c direction.

The staggered antiferromagnetic order is certainly realized in the (0,0,1) plane below T_N = 4 K in $Ba_2MnGe_2O_7$ [14, 57] (Fig. 1.13). In the case of $Ba_2CoGe_2O_7$ the interplane magnetic coupling is ferromagnetic ($J_c < 0$), while in $Ba_2MnGe_2O_7$ the interplane magnetic coupling is antiferromagnetic ($J_c > 0$).

Also in this case, in literature is reported the magnetic-field dependence of electric polarization $\mathbf{P}_c$ with various magnetic field directions. The observation of the finite electric polarization in the fully spin-polarized ferromagnetic state in the high magnetic field is a strong evidence for the d-p hybridization mechanism because the other mechanisms of the magnetically induced ferroelectricity are irrelevant in this magnetic state.

While the magnetic field variation of ferroelectricity is qualitatively similar to

that in $Ba_2CoGe_2O_7$, it should be noted that the shape of the *P-H* curve is slightly different [9], reflecting the inequivalent magnetic sites generated by the interplane antiferromagnetic interaction.

As in $Ba_2CoGe_2O_7$, the electric polarization is induced by the external magnetic field even above $T_N = 4$ K; $\mathbf{P}_c \sim H^2$ in the high-temperature region. The temperature and magnetic-field dependencies can again be explained well by the spin-dependent *d-p* hybridization mechanism.

$M = Mn$
canted G-AFM

$M = Co$
canted C-AFM

$M = Cu$
helical $\approx$ C-AFM
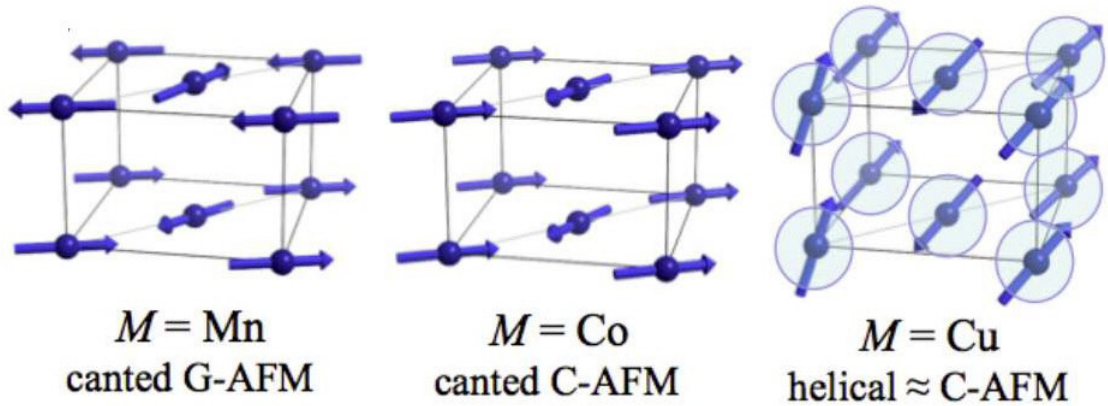
Figure 1.13: Magnetic orderings as reported for Mn, Co and Cu samples, from left to right, illustrating AFM−G, AFM−C and the helical modulation of the AFM−C configurations. A small canting arising from relativistic Dzyaloshinskii−Moriya interaction has been reported for the first two configurations. The estimated exchange couplings are also schematically shown.[9]

1.5.4 $Ba_2(Ni,V)Ge_2O_7$

$Ba_2MGe_2O_7$ with (M=Ni,V) are proposed as class of oxides where Jahn−Teller (JT) distortions can lead the appearance of electric polarization [65].

The lack of inversion symmetry of the local tetrahedral environment allows for odd ionic displacements to couple with the degenerate electronic states and, therefore, for the symmetry allowed appearance of local dipole moments. On the basis of general symmetry considerations, this study shows that polar JT distortions may locally develop in this structure when JT-active transition-metal ions are considered. Density functional theory (DFT) calculations are then used to propose melilite oxides where such polar JT effects can appear, possibly leading to ferroelectric, antiferroelectric, or ferrielectric phases. The

analysis starts from the experimental crystal structure of $Ba_2CoGe_2O_7$ belonging to the P-42_1m space group and fully optimizes it by substituting Co with the JT-active ion Ni^{2+} while imposing different magnetic configurations of the transition metal magnetic moments. Also, V^{2+} is considered, whose electronic configuration is physically equivalent to Ni^{2+}, but with occupied majority spins only.

By combining symmetry-based JT analysis and density functional theory calculations, a lowering the crystal structure symmetry is found to the C$mm2$ space group.

It is found that both Ni and V oxides display an antiferromagnetic ground state, and therefore they can be considered as proper multiferroic materials. The in plane exchange constant J_{ab} appears to be the dominant antiferromagnetic interaction, while the out of plane exchange J_c changes from a ferro to antiferromagnetic interaction when Ni is replaced by V, leading to C$-$type and G$-$type AFM configurations, respectively.

It's clear that the physical properties of the insulating oxides BMGO mainly depend on the nature of the transition metal ion and along the series there is complete variation of electronic configuration, spin state, polarization and d - p hybridization as well as cell parameters. Due to the substantially local nature of some proposed mechanisms, interesting ferroelectric$-$multiferroic properties could emerge in mixed melilite oxides.

From the literature, quite surprisingly an almost complete absence of reports on the $Ba_2NiGe_2O_7$ and $Ba_2VGe_2O_7$ is evinced.

The synthesis of this material is therefore very interesting but challenging issue.

Furthermore, regardless of the existence of pure $Ba_2NiGe_2O_7$ phase, also the partial substitution of copper with nickel in the $Ba_2CuGe_2O_7$ structure can be a fascinating topic of investigation, this replacement could lead to strong changes in the magnetic phase diagram and eventually to multiferroicity.

However, it should be kept in mind that, if $Ba_2NiGe_2O_7$ has a different crystalline structure, even the formation of mixed samples could not be trivial. In general, the members of melilite family can form solid solutions with each other for any composition, as the end compounds are isostructural, but this should not occur with $Ba_2NiGe_2O_7$.

In other words, considering the system $Ba_2Cu_{(1-x)}Ni_xGe_2O_7$ a miscibility gap should exist for some intermediate values of x.

All these aspects will be discussed and studied in deep in the following chapters.

1.6 Magnetic phase diagram of Ba$_2$CuGe$_2$O$_7$

Main features of Ba$_2$CuGe$_2$O$_7$ are discussed in section (1.5.1), below the complex magnetic properties are discussed showing magnetic phase diagrams reported in literature [18].

Ba$_2$CuGe$_2$O$_7$ is an example of a helimagnet suitable for experimental investigation thanks to a fortunate combination of physical properties. This system is a type of helimagnet where in addition to 1D spin spirals, the ground states can form a vortex (skyrmion) lattice, as predicted by Bogdanov et al. in a number of related models [70, 71, 72].

Due to the low tetragonal symmetry, the corresponding Heisenberg Hamiltonian involves an interesting combination of antisymmetric (DM) as well as symmetric exchange anisotropies which lead to a rich magnetic phase diagram. Originally, the magnetic properties of this quasi 2-dimensional (2D) antiferromagnet were investigated as part of the ongoing search for new singlet ground state compounds, triggered by the discovery of a spin transition and other extraordinary magnetic properties of CuGeO$_3$, CaCuGe$_2$O$_6$ and BaCuSi$_2$O$_6$. The basic feature of Ba$_2$CuGe$_2$O$_7$ is a square arrangement of Cu^{2+} ions in the (a,b) plane (Fig. 1.14). Nearest neighbour in plane AF exchange along the diagonal of the (a,b) plane is the dominant magnetic exchange interaction (J∥∼ 0.96 meV per bond) while the interaction between Cu atoms from adjacent planes is weak and ferromagnetic (J⊥∼ -0.026 meV) [73, 64]. Below T$_N$ = 3.2 K an almost AF cycloid is observed, this is due to DM vector along the diagonal of the basal (a,b) plane. A schematic diagram of the cycloidal spin structure is given in Fig. 1.14; for the propagation vector **q** along (1,1,0), spins are confined in (110) plane, the rotation angle β relative to a perfect antiparallel alignment is 9.7° per unit cell. Note that for a single domain sample, a small ferroelectric polarization is indeed observed [67].

Muhlbauer et al. [18] report the evolution of magnetic phases of this system proved through neutron diffraction in combination with bulk measurements of magnetization and specific heat.

Complex magnetic behaviour of Ba$_2$CuGe$_2$O$_7$ in canted magnetic fields is showed in magnetic phase diagrams (Fig. 1.15). Figure 1.15(a) shows the phase diagram for magnetic field H confined in the (1,1,0) plane, Fig. 1.15(b) for the (1,0,0) plane. The salient features of the different phases and phase transitions are summarized in the following. At zero field, an almost AF cycloidal spin structure is observed, the ideal cycloidal spin structure is slightly distorted due to the Kaplan-Shekhtman-Entin-Wohlman-Aharony (KSEA) interaction [73]. Increasing magnetic field applied along the c axis
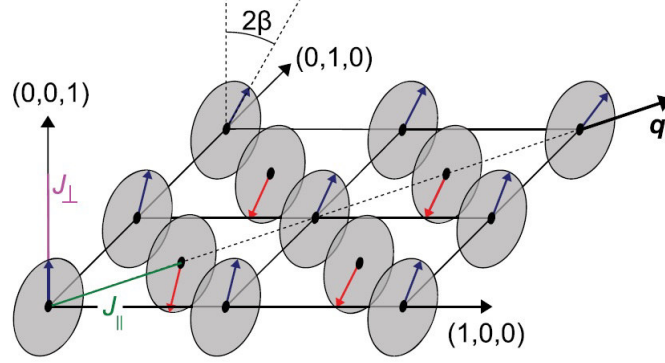
Figure 1.14: Almost AF cycloidal magnetic structure of $Ba_2CuGe_2O_7$. The dominant exchange paths $J_{\parallel}$ and $J_{\perp}$ are indicated by the green and magenta colored line, respectively.[18]

[74], distortion of cycloid is observed, this distortion becomes a soliton lattice for $2 < H < 1$ T. Close to the I−C transition, an AF cone phase is found closely aligned to the c axis.

Applying a magnetic field strongly tilted with angle $\alpha > 10°$ with c axes, a crossover from the soliton lattice to a distorted incommensurate phase is seen in neutron diffraction and magnetization. Finally, the I-C transition can be continuously followed in magnetic susceptibility up to $H_c = 9$ T for magnetic field in the (a,b) plane, both along the $(1,0,0)$ and $(1,1,0)$ directions ($\alpha = 90°$)(Fig. 1.15).

Fig. 1.16 shows (H,T) phase diagram containing the data obtained in the neutron diffraction experiments, measurements of magnetization and specific heat.

Below a temperature T_N, applying a magnetic field higher than 3T along c axis (Fig. 1.16(a)) the structure is commensurate. In the low field region, the structure is incommensurate, from AF cone phase in a short range of H$\sim$ 2T to soliton phase and finally almost cycloid phase, with decreasing field.

The (H,T) phase diagram for tilted field is shown in Fig. 1.16(b)). The grey area around the transition line at $\sim$2 T denotes the crossover from the almost AF cycloidal phase at low field to the distorted phase at high fields, as measured by magnetic susceptibility. Compared to the phase diagram obtained for magnetic field along the c axis, the main differences resulting in a slightly increased critical field and absence of the AF cone phase.

A similar trend is observed for the (H,T) phase diagram for magnetic field parallel to the (110) direction (Fig. 1.16(c)). Here, the critical field is shifted to $\sim$9 T, consistent with magnetic susceptibility. The crossover from the

almost AF cycloidal phase to the distorted phase is completely smeared out and hence featureless in magnetic susceptibility.

Most of current research is focused on the search of suitable systems where to study the helimagnetic or skyrmionic magnetic order. Because of combination of magnetic properties just discussed, $Ba_2CuGe_2O_7$ is identified as a good candidate. This work focuses on optimization of crystal growth to realize large and pure single samples which can be used to determine magnetic domain structure.
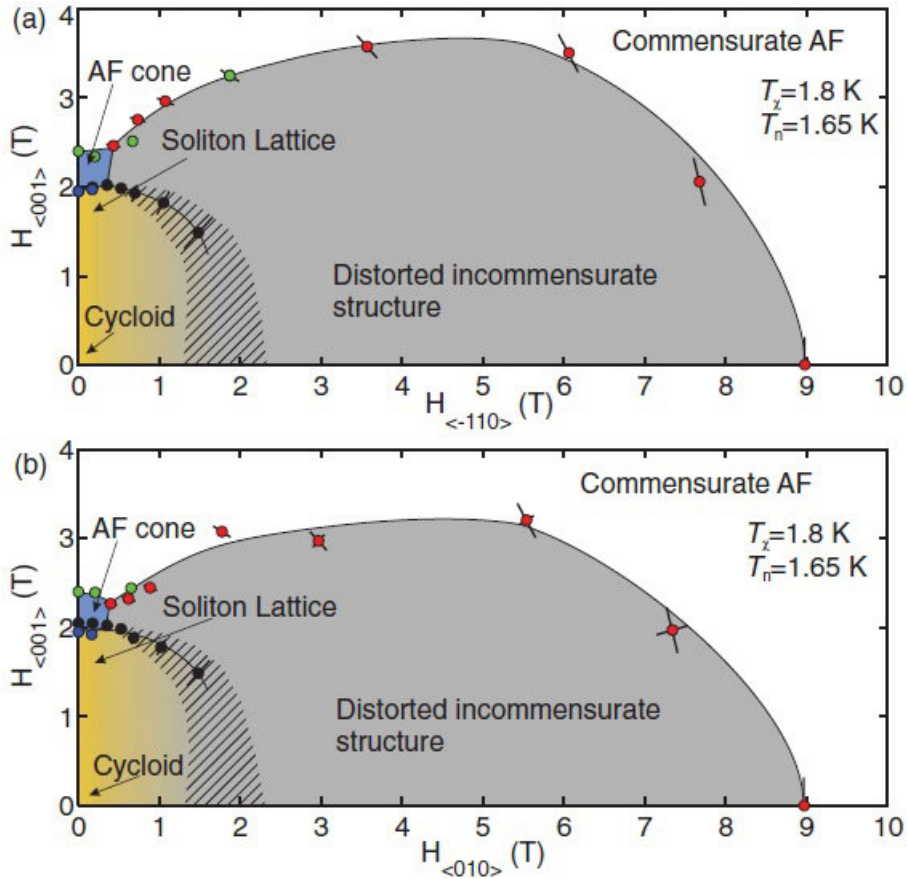
Figure 1.15: Phase diagrams of $Ba_2CuGe_2O_7$ for magnetic field confined in the (1,1,0) a) and the (1,0,0) b) planes. Green and blue markers indicate the I−C transition at H_C and the phase transition from the soliton lattice to the AF cone phase at H_1 as seen by neutron diffraction, respectively. Black points stand for H_1 as obtained by magnetic susceptibility. The hatched area thereby corresponds to the region where a broad crossover is observed. Red markers indicate the I−C transition at H_C, seen by magnetic susceptibility. Neutron data points have been taken at T = 1.65 K, magnetic susceptibility at T = 1.8 K, respectively. The lines serve as guide to the eye.[18]
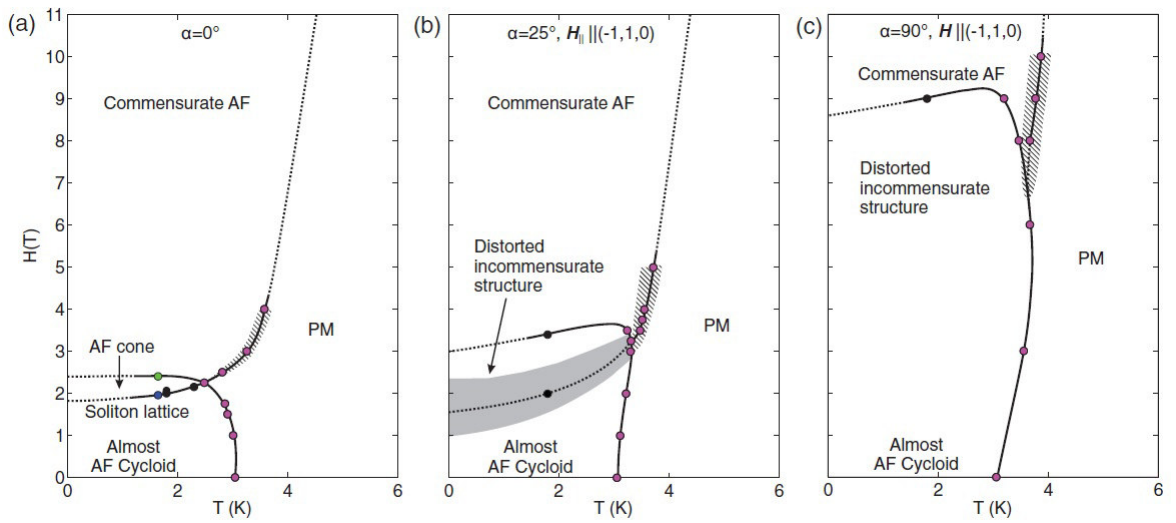
Figure 1.16: Phase diagram of $Ba_2CuGe_2O_7$. The same color code as for Fig. 1.15 is used. Data points obtained by measurements of the specific heat are shown in magenta. a) shows the phase diagram for magnetic field aligned along the c axis. b) shows the phase diagram for $\alpha = 25°$, confined in a (1,1,0) plane. c) shows the phase diagram for magnetic field along the (1,1,0) direction. Solid lines serve as guide to the eye. Dashed lines represent the assumed continuation of the phase transition lines, based on our model of the magnetic structure.[18]

1.7 $Cu_3Nb_2O_8$

Considerable efforts are required to realize the coexistence of electric polarization and long-range magnetic order. Practically, functional devices that incorporate multiferroic materials are yet to be realized. However, research in this field is extremely active given the potential for creating new technology such as energy-efficient, electrically written magnetic memories. Multiferroics and in particular those with spin of spiral origin are also targets for fundamental research in the quantum properties of matter. Such magnetic ordering below a given temperature lowers the symmetry group from a nonpolar parent phase to a polar magnetic phase. Magneto-structural coupling to the crystal structure gives rise to an electrically polar state, inducing ferroelectricity.

As shown in the section (1.3.2), three mechanisms are responsible of ferroelectricity of spin origin. The spin current model is studied in many systems, indeed this mechanism is reported in helimagnet $LiCu_2O_2$ [75, 47], in $MnWO_4$[41, 42] etc., instead there are few systems with electric polarization induced by $p-d$ hybridisation. Despite this difference, there are many aspects to clarify for the first mechanism.

Indeed, surprisingly, innovative systems show an electric polarization almost perpendicular to the plane of rotation of spins ($CaMn_7O_{12}$ [76, 77], MnI_2[78] and $CuFeO_2$ [39]), while the polarization is expected in the spin plane. Controversial hypotheses are discussed to explain this feature which is in contradiction with model [10, 79].

$Cu_3Nb_2O_8$ is an example of above systems. It is one of only two multiferroic known with centrosymmetric triclinic crystal structure with P -1 space group. The other one is $FeVO_4$ [80]. Triclinic multiferroics provide a unique paradigm for theoretical studies. Any complex long-range magnetic order is likely to break inversion symmetry, giving rise to a polar phase with no symmetry constraints on the direction of the electric polarization.

There are many open questions, for example why of **P** is observed only when the magnetic structure becomes non-collinear. This makes crucial the growth of single crystals with millimetric size to realize anisotropic electric polarization measurements. The most of research on this compound has been done on polycrystalline samples with the exception of only one investigation by Johnson et al. [10] on $Cu_3Nb_2O_8$ single crystals.

$Cu_3Nb_2O_8$ orders magnetically at $T_N \sim 26{,}5$ K, and shows an electrical polarization below a second magnetic transition at $T_2 \sim 25$ K. In the polar phase below T_2, a coplanar helicoidal magnetic structure is stabilized with propagation vector **q** = (0.4876, 0.2813, 0.2029).

Triclinic crystal structure shows at room temperature lattice parameters a=5.1829Å, b=5.4857Å, c=6.0144Å,α =72.58°, β =83.421°, γ =65.71°. There are two distinct Cu^{2+} sites in the unit cell, located at Wyckoff positions 1a (Cu1, on an inversion center) and 2i (Cu2). The magnetic Cu^{2+} sites (S= $\frac{1}{2}$) form sawtooth chains parallel to the a-axis with 3-atom Cu2-Cu1-Cu2 steps sharing the edges of their CuO_4 squares, linked by Cu2-Cu2 risers (jumps), sharing the edges of the triangular faces of the pyramids (Fig. 1.17). The key element of the structure is Cu_3O_8 which forms the staggered Cu-O chains along the a axis, and further, the chains extend to become the Cu-O layers, separated by the non magnetic Nb atoms in between these layers (Fig. 1.18). The electric polarization is determined through the integration of a pyroelectric current with E = 2 kVcm^1. Reference [10] reports that P is along (1,3,2) direction with a magnitude of 17.8 μ C m^{-2} at 10 K. As mentioned, the most important feature is that the electrical polarization is nearly perpendicular to the plane of rotation of the spins ($\sim$ 14° to the vector normal to the spin rotation plane), in contradiction with the predictions of the cycloidal multiferroics model[10].

Very probably the electrical polarization in $Cu_3Nb_2O_8$ must arise through coupling of the chiral component of the magnetic structure with the crystal structure with very low symmetry.

In cycloidal magnets, local DM vectors D_{ij}, associated with pairs of magnetic atoms i and j separated by the bond vector r_{ij}, are decomposed in components parallel and perpendicular to r_{ij} by:

$$D_{i,j} = P_{i,j} \times r_{i,j} + \sigma_{i,j} r_{i,j} \qquad (1.5)$$

where $P_{i,j}$ is a polar vector and $\sigma_{i,j}$ is a pseudoscalar (both quantities are time-reversal even). $P_{i,j}$ can be taken to be the local polarization, so that the macroscopic polarization is $\mathbf{P} = \sum P_{i,j}$.

$\sigma_{i,j} = 0$ and $P_{i,j} = 0$, respectively, when a cycloidal structure is not chiral. Instead, in the case of a generic helicoidal structure, both $\sigma_{i,j}$ and $P_{i,j}$ are present, but only the latter, which is always within the rotation plane of the spins, is considered in the cycloidal multiferroics model. On the other hand the chiral term $\sigma_{i,j}$ cannot in itself produce a polarization, but it can do so through coupling with the crystal structure, it provides that the paramagnetic phase supports a macroscopic axial vector $\mathbf{A}$, so that $\mathbf{P} = \gamma \sigma \mathbf{A}$ (γ being a purely structural coupling constant). Note that the electrical polarization in this case is always parallel to $\mathbf{A}$. Macroscopic axial vectors represent collective rotations of one part of the structure with respect to another, and are only allowed in certain crystal classes (as P-1 of $Cu_3Nb_2O_8$) called ferroaxial classes.
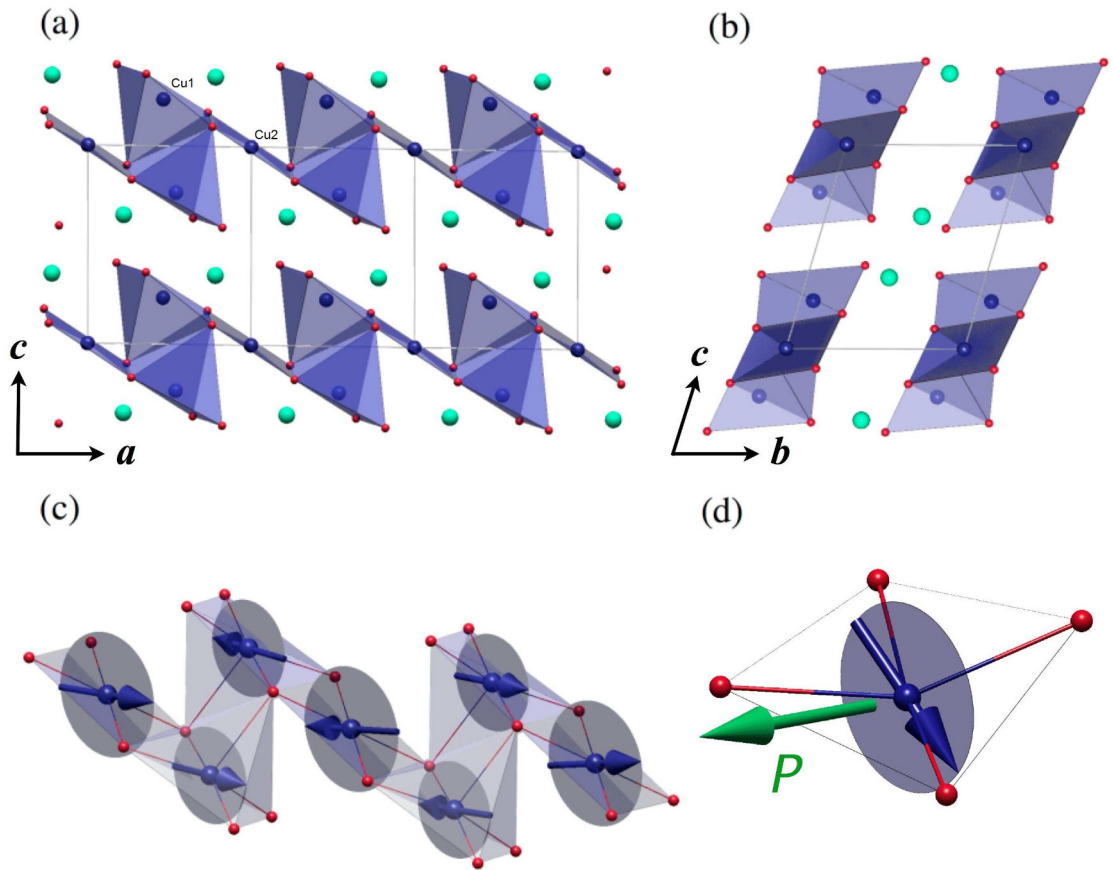
Figure 1.17: (a) and (b): The crystal structure of $Cu_3Nb_2O_8$ in the ac- and bc-plane, respectively. Cu^{2+} ions form saw-tooth chains parallel to the a-axis with steps of three edge sharing CuO_4 squares. The steps are linked via Cu2-O-Cu2 *risers*. Nb^{5+} atoms separate the chains along the b-axis. (c): The magnetic structure of the Cu^{2+} chains. The envelope of the spin rotation is shown by grey circles. (d) **P** (green arrow) perpendicular to the spin rotation plane.[10]
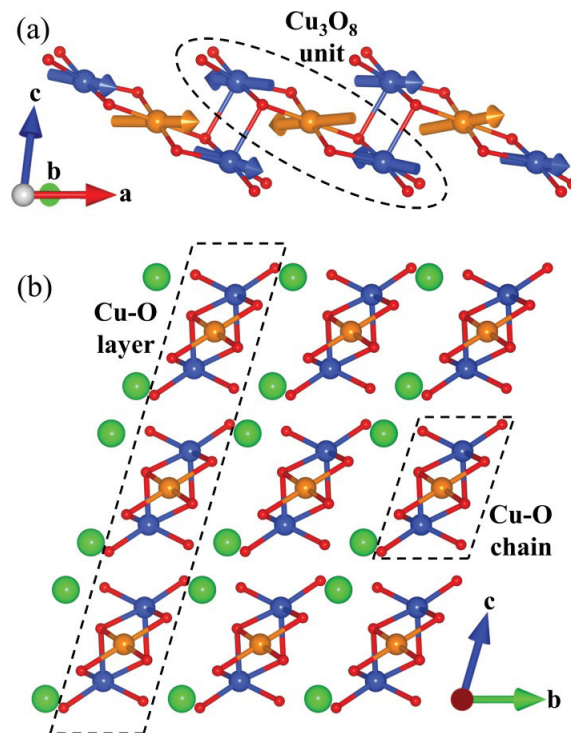
Figure 1.18: (a) The Cu_3O_8 units connect to form the Cu-O chain. The Cu1 atoms that are at the inversion center are in brown, and the Cu2 atoms are in blue. The magnetic structure is approximately given by the FM-u and AFM-c arrangements. (b) Cu-O chains stacked to form Cu-O layers, separated by nonmagnetic Nb atoms. The Nb-O bonds are not shown.[79]

Chapter 2

Synthesis of $Ba_2MGe_2O_7$ (M=Cu,Ni,Mn) and $Cu_3Nb_2O_8$

As mentioned in the previous chapter, this work focuses on two systems: $Ba_2MGe_2O_7$ (M=Cu,Ni,Mn) and $Cu_3Nb_2O_8$. Single crystal samples are vital to study the physical properties exhibited by compounds which have high magnetic\ferroelectric anisotropy where significantly different behaviour is seen along different crystallographic directions.

Therefore, this chaphter is concerned on the growth of large and pure single crystals which can be used for many types of investigations.

In this work the procedures to synthesize polycrystalline samples are described in detail and the conditions of the crystal growths by floating zone technique are discussed.

2.1   The floating zone technique

In crystalline solids, atoms are arranged in a regular manner. In an ideal single crystal, *Bravais lattice* specifies the periodic array in which the repeated units of the crystal are arranged. The units themselves may be single atoms, groups of atoms, ions etc. but the Bravais lattice summarizes only the geometry and the periodic structure [81]. From the definition a single crystal is free of lattice imperfections. In crystals, strong connection between the optical, electrical and mechanical responses with the crystal structure is often observed, and these features are used in many current technologies.

Crystal growth refers to the artificial synthesis of crystals and can be roughly classified into three groups: solid-solid, liquid-solid and gas-solid processes, depending on which phase transition is involved in the crystal formation. Among these three categories liquid-solid process is one of the oldest and most widely used techniques to get pure samples. Crystal growth from melt is undoubtedly the most popular method for growing single crystals at large scale.

Melt growth can be achieved by a variety of techniques (e.g. free melt surface of confined configurations) depending on the specific properties of the material (e.g. contraction or expansion during solidification) and requirements. The growth from melt can be subgrouped into various techniques. The main techniques are: Czochralski, Bridgman-Stockbarger, Verneuil, zone melting technique, skull melting process, shaped crystal growth technique.

Single crystals discussed in this work are grown by floating zone technique. The most obvious advantages of the floating zone technique are that: no crucible is necessary, oxides melting as high as 2500°C can be grown, the growth can be conduced at high pressure (up to 10 atm) and in specific atmosphere. On the other hand, this method is not suitable for materials with high vapor pressure, low surface tension, high viscosity.

The floating zone method is the subject of extensive development such that current furnaces are appreciated for their adaptability, compactness of design and high efficiency, which sees them extensively utilized to grow single crystals of an ever increasing variety of materials [82, 83, 84, 85, 86].

Three types of floating zone furnace are commercially avaible, with one, two and four ellipsoid mirrors. In this work the samples are realized through floating zone technique using image furnaces with different features (Tab. 2.1). Early designs of furnaces for floating zone melting had one or two mirrors, but in the last years some image furnaces are realized with four mirrors to both increase the power of the furnace and also to obtain more uniform sample heating.

Below, floating zone method to grow a single crystal is summarized briefly. The first step is a typical powder synthesis. The batch of weighed appropriate powders is carefully prepared by ceramic method.

In all image furnaces, the basic concept is that either ellipsoidal or parabolic mirror(s) (or combination of the two) [86] is used to focus the light from halogen or xenon lamp(s) onto a vertically held rod shaped sample (feed rod) to produce a molten zone, which is then moved along the sample in order to grow a single crystal (Fig. 2.1). Inside a quartz chamber, the feed rod is suspended above a crystal of the same compound or similar (the seed). Feed and seed rods are brought close to each other at the centre of the furnace. The light from halogen (or xenon) bulbs is focused by ellipsoidal mirrors in the centre of quartz tube, creating a small region of high temperature. The temperature in this point is gradually increased until both rods reach their melting points. They are brought together to make a molten zone, held together by the surface tension of the material. The rods rotate in opposite direction to mix materials. The rods (or the mirrors) are then both lowered through the hot region such that the length of the feed rod is transformed from polycrystalline to a molten state, and then into a single crystal as it leaves the high temperature zone and resolidifies upon slow cooling.

The use of light heating makes the technique suitable for both conducting and non-conducting materials, a feature that distinguishes image furnace growth from float zoning using induction or electron beam heating, both of which are limited to use with conductors. Although light heating is not suited to all materials (it struggles, for example, with those metallic samples that exhibit a high reflectivity in the infrared region), it is particularly convenient and efficient for those oxides and semiconductors that absorb infrared easily.

Using the floating zone method, crystals up to 80 mm in length and 8 mm in diameter are grown.

The stability of the growth process and the quality of crystal obtained depend strongly on the quality of the ceramic rod which acts as the source of material for crystallization.

Experimental parameters need to be controlled when growing crystals in order to optimize both the stability of the molten zone and the crystal quality. Experimental parameters include materials properties (chemical composition, thermal conductivity, volatility and viscosity) and setting parameters (translation speed, gas pressure, rotation rate, power of lamps).

To realize single crystal with high quality, different parameters are optimized during a growth experiment:

Feed rod characteristics. Well compacted, homogeneous in composition,
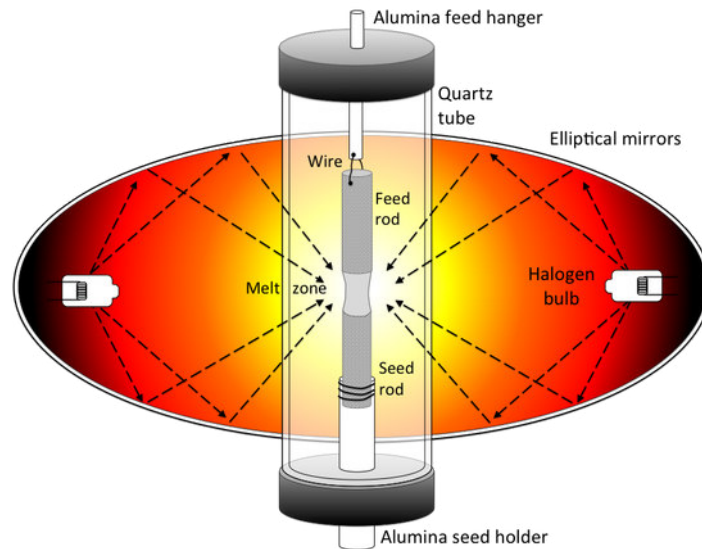
Figure 2.1: Schematic of the floating zone technique.

straight and constant diameter feed rod is required to achieve and keep a perfectly stable molten zone.

Growth translation. It is one of the most critical parameters which can affect crystal quality. Changes of this parameter show effects on final crystal in terms of size, formation of secondary phases or inclusions, cracks, composition, low angle grain boundaries, twin formation, bubbles and also influences the liquid/solid interface and molten zone stability.

Growth atmosphere and gas pressure. These parameters are selected according to the phase stability of the sample and thermodynamic data. In general, for oxides the growth atmosphere is selected to be pure oxygen (or oxygen mixed with argon) while for metallic samples selected atmosphere is argon or vacuum due to potential oxidation at higher temperatures. Usually, increasing the gas pressure increases the lamp power needed to melt the sample, leading to the general assumption that the melting point of the material increases under higher gas pressure. The other significant and functional effect of increasing the gas pressure is to reduce vaporization of volatile components from the sample.

Temperature gradient. A large temperature gradient along the growth direction can cause thermal stresses in the growing crystal which result in cracks. Temperature gradient along a sample depends on several factors such as the type of image furnace (number of mirrors or lamps

Specifications	Nec Machinery IM	Crystal Systems Inc.IM
Model	SC1-MDH11020	F-ZT-10000-H-IV-VPS
Type of lamp	Halogen	Halogen
Elliptical Mirrors	Two	Four
Power Lamp	2000 W	500 W
Max Temperature	2200°C	2200°C
Max pressure	10 bar	10 bar

Table 2.1: Specifications of the image furnaces (IM) used in this work.

around the sample, type of the lamps, xenon or halogen, power of the lamps, lamp alignment) and crystal properties (thermal conductivity, anisotropic thermal expansion).

Rotation rate. Rotation is usually used to ensure efficient mixing in the molten zone (liquid homogeneity) and a more homogeneous temperature distribution within the melt. To use higher rotation rate, which enhances forced convection in the molten zone by transporting the heat absorbed on the melt surface, is an effective way to lower the convexity of the interface during growth.

In this work, the furnaces used for crystal growth are the NEC SC1-MDH11020 (Fig. 2.2), and the Crystal Systems Inc. F-ZT-10000-H-IV-VPS (Fig.2.3) (Table 2.1).
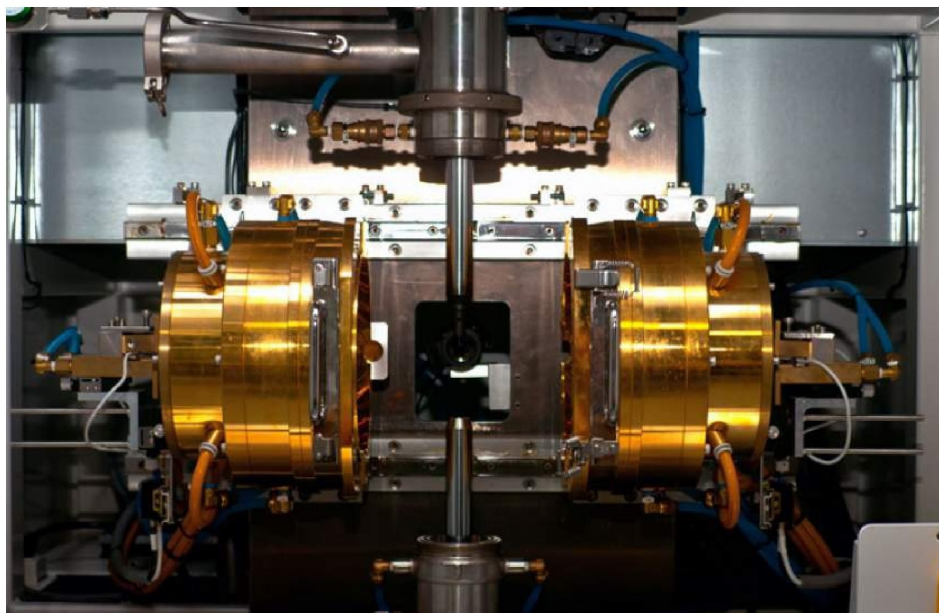
Figure 2.2: Two mirrors image furnace in inside view.
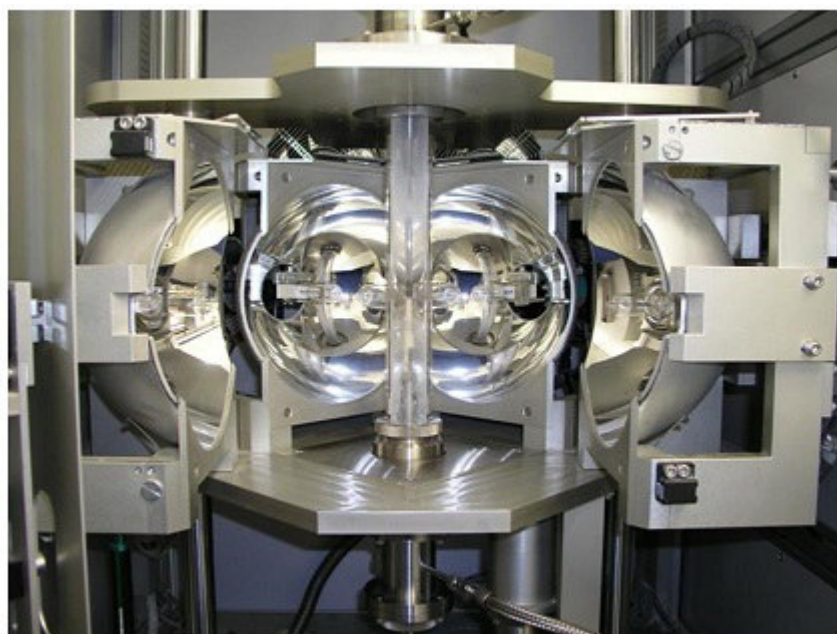
Figure 2.3: Four mirrors image furnace in inside view.

2.2 Ba$_2$CuGe$_2$O$_7$ preparation

2.2.1 Powder synthesis

The preparation of the polycrystalline feed rods is a delicate procedure which requires special attention. In literature, chemical phase diagram of this compound is not reported, therefore powder synthesis of phase Ba$_2$CuGe$_2$O$_7$ requires many attempts as reported in [87].

The starting materials for the preparation of feed and seed rods for growing Ba$_2$CuGe$_2$O$_7$ crystals are BaCO$_3$ (Sigma Aldrich 99.999 %); CuO (MVLaboratories 99.9999%)and GeO$_2$ (Alfa Aesar, 99.9999%).

The Ba$_2$CuGe$_2$O$_7$ polycrystalline rods are prepared by conventional solid state reactions at high temperature. We adopt two different methods, called *Method A* and *Method B* in the following, for making single phase polycrystalline rods. In both methods, before the reactions, BaCO$_3$ is pre−annealed at 500°C for 1h, and then mixed with the other starting materials, in stoichiometric proportions and heated. In *Method A* three thermal treatments at 850°C for 24h, 900°C for 24 h and 950°C for 15 h with intermediate grindings are performed. After cooling down, the synthesized powder is thoroughly reground and the powder is isostatically pressed for about 10min in water to a pressure of approximately 50 MPa. The resulting cylindrical rods are sintered in a furnace, in a vertical position, at 980°C in air for 15h.

In *Method B* both the BaCO$_3$, and the GeO$_2$ are pre-annealed, the latter at 800°C. The pre−annealing of both BaCO$_3$ and GeO$_2$ produces dried powders guaranteeing the mixing of the powders in the desired stoichiometry. Moreover, X-ray analysis on GeO$_2$ powder performed before and after the 800°C thermal treatment show a partial transition from α-quartz to the rutile-type structure. It is well known that GeO$_2$ exhibits several polymorphs that mainly differ in their chemical properties, especially solubility and densities. Hence the reaction of GeO$_2$ in our system, depending on the phase stability and microstructure, is favoured by the thermal treatment. Concerning the method B, after the pre-annealing, mixtures of starting materials in stoichiometric proportions are heated at 880° for 15 h, 950°C for 20h and 980°C for 60 h with intermediate grinding. Finally, the rods are prepared as in the method A. In both methods, the resulting sintered rods are typically 6 or 7 mm in diameter and 60−90 mm in length and their densities is determined to be about 85% of the theoretical density of Ba$_2$CuGe$_2$O$_7$.

Steps of method A and of methos B are summarized in Tab. 2.2.

Method A	Temperature (C)	Duration (h)
Pre-annealing of $BaCO_3$	500°	1
Calcination 1	850°	24
Sintering 1	900°	24
Sintering 2	950°	15
Sintering 3, preparation of feed rod	980°	15
Method B	**Temperature(C)**	**Duration (h)**
Pre-annealing of $BaCO_3$	500°	1
Pre-annealing of GeO_2	800°	12
Calcination 1	880°	15
Sintering 1	950°	20
Sintering 2	980°	60
Sintering 3, preparation of feed rod	980°	15

Table 2.2: Methods A and B sample heating procedures for $Ba_2CuGe_2O_7$.

2.2.2 Crystal Growth

As discussed in section (1.5), investigations on $Ba_2CuGe_2O_7$ show a great number of interesting properties. The study of all complex anisotropic phenomena requires the availability of good crystals. Many studies are realized on single crystals of this compound; however, the procedure of crystal growth is not reported. For the first time, we report procedure of single crystal growth in reference [87].

For growing single crystals in this study, we employ the floating zone method using two types of optical image furnaces with elliptical mirrors. One has double-elliptical mirrors (NEC Machinery,model SC1-MDH11020 at CNR-SPIN Salerno) with two 2.0 kW halogen lamps. The other has four elliptical mirrors (Crystal System, model F-ZT-10000-H-IV-VPS at the University of Warwick) with four 500W halogen lamps. After several attempts of crystal growth, varying the growth conditions, including the speeds of the feed rod and the seed crystal, the counter-rotation speeds and the gas atmosphere, large single crystals with high crystalline quality are obtained.

The entire set of growth parameters attempted are summarized in Table 2.3. We can see that the rods from method A give mixed phase (batches No.1 and 2) or small crystals (batches No.3-6) for low growth speed. Improving the quality of the starting polycrystalline rods with method B, as discussed later, we get bigger and purer crystals (batchesNo.8-13). Moreover, from the results summarized in Table 2.3 we can deduce that the rotation speed, responsible

for mixing of material and for the shape of the crystallization front, and the furnace type, strictly related to the temperature distribution with in the molten zone, greatly influence the size and the colour of the crystals. Infact, comparing the results for batches No.7 and No 8 we can see that for the same growth conditions only increasing the rotation speed we change the crystal size.

From a comparison of batch No.8, grown using a two mirror furnace with rotation speeds of 20 rpm,and batch No 13, grown using a four mirror furnace with a rotation speeds of 30 rpm, we can observe that they show a change in the colour of crystal and this may be related to a combination of two factors: different temperature gradient with in the molten zone, related to the different crystal growth furnace used, and to a change of the shape of the crystallization front, due to a change in the rotation speeds. The best results are obtained (Fig. 2.4) for a growth rate of 0.5mm\h, a rotation speed for both rods of $15-30$ rpm and an atmosphere of pure O_2 or dried air at a pressure of 3 or 5.5 bar, respectively. It is worth mentioning that the best crystals are obtained starting from feed rods obtained by method B. This method, as further discussed later, assures polycrystalline rods with the right $Ba_2CuGe_2O_7$ phase. This is an important factor in order to achieve a stable liquid zone producing large crystals.

Batch	Method	Growth speed	Rotation	Atmosphere	Comments
1	A	5 mm\h	40 rpm	Dried Air,1 bar	Polycrystalline mixed phases
2	A	5 mm\h	33 rpm	O_2,1 bar	Polycrystalline mixed phases
3	A	0.5 mm\h	30 rpm	O_2,1 bar	Small transparent yellowish crystals
4	A	1.5 mm\h	10 rpm	Dried Air,5.5 bar	Small transparent yellowish crystals
5	A	0.5 mm\h	20 rpm	Dried Air,5.5 bar	Small transparent yellowish crystals
6*	A	0.5 mm\h	30 rpm	O_2,3 bar	Small transparent yellowish crystals
7	B	0.5 mm\h	10 rpm	O_2,3 bar	Small dark yellow crystals
8	B	0.5 mm\h	20 rpm	O_2,3 bar	Large dark yellow crystals
9	B	0.5 mm\h	15 rpm	Dried Air,5.5 bar	Large transparent yellowish crystals
10	B	0.5 mm\h	25 rpm	Dried Air,5.5 bar	Large transparent yellowish crystals
11	B	0.5 mm\h	25 rpm	Dried Air,5.5 bar	Large transparent yellowish crystals
12	B	0.5 mm\h	25 rpm	Dried Air,5.5 bar	Large transparent yellowish crystals
13*	B	0.5 mm\h	30 rpm	O_2,3 bar	Large transparent yellowish crystals

Table 2.3: Summary of $Ba_2CuGe_2O_7$ crystal quality with varying growth conditions. The crystals labelled by the superscript* are grown using a four mirror furnace, while all the other growths are performed employing a two mirror furnace [87].
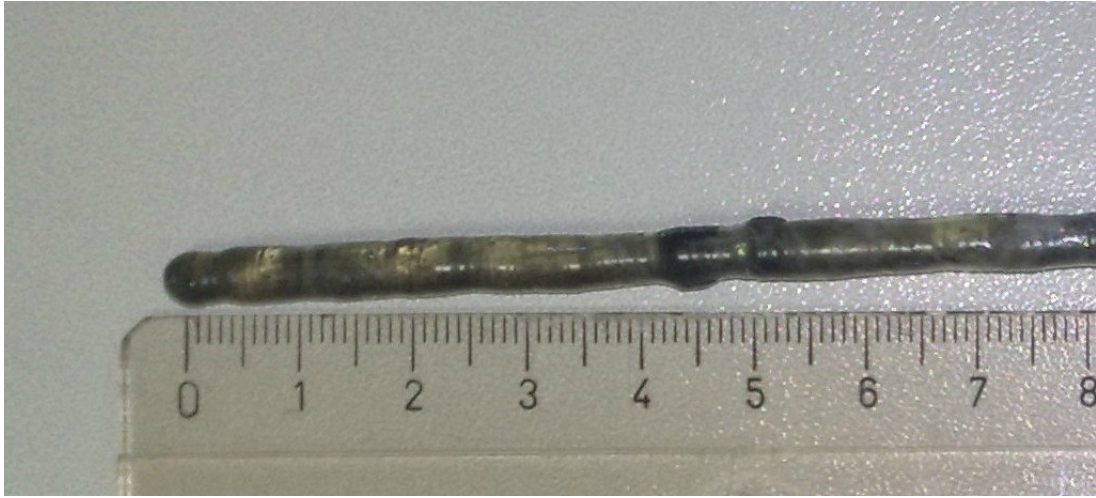
Figure 2.4: Photograph of a $Ba_2CuGe_2O_7$ single crystal grown in this work (batch No.10).

2.3 $Ba_2Cu_{1-x}M_xGe_2O_7$ preparation (M=Ni,Mn)

2.3.1 Powder synthesis

Physical properties of the insulating oxides $Ba_2MGe_2O_7$ (where M indicates a transition metal) mainly depend on the nature of the transition metal ion. Due to the substantially local nature of some proposed mechanisms, interesting properties could emerge in mixed melilite oxides.

In the following, it will be described the synthesis of polycrystalline samples with the partial substitution of copper with nickel or manganese in the $Ba_2CuGe_2O_7$ structure.

$Ba_2Cu_{(1-x)}Ni_xGe_2O_7$ (BCNGO) are prepared as polycrystalline powder by heat treatments of starting materials: $BaCO_3$ (Sigma Aldrich, 99.999%); GeO_2 (Alfa Aesar, 99.9999%); NiO (Sigma Aldrich, 99.99%); CuO (MV Laboratories, 99.9999%). Samples are prepared with x in the range from 0.05, to 1.

Similarly, to the synthesis of $Ba_2CuGe_2O_7$, at first $BaCO_3$ is pre-annealed at 500°C for 1 h and GeO_2 is pre-annealed at 800°C for 12 h. After that, the powders are stoichiometrically mixed, pressed and heated at 880°C for 15 h, at 950°C for 20 h and at 980°C for 60 h in a muffle furnace, with intermediate grinding after any step.

For all BCNGO ceramics, the thermal steps described above are performed. For Ni0.05, Ni0.006, Ni0.08, Ni0.1 and Ni0.2 (samples with x=0.05, 0.06, 0.08,

0.1 and 0.2, respectively) a successive thermal process is added at 980° for 30 h while for Ni0.3, Ni0.4, Ni0.5 (x=0.3, 0.4 and 0.5) two thermal treatments are added at 980°C of 30h and 60h, respectively. Finally, for Ni0.6, Ni0.7, Ni0.8, Ni0.9 (x from 0.6 to 0.9) three thermal steps are added, the first one at 980°C of 30h and the last two at 980°C for 60h .

To prepare polycrystalline sample of $Ba_2NiGe_2O_7$, pre-annealed $BaCO_3$ and GeO_2 are used. Two long thermal processes are executed at 1200°C for 60 h. Powder melts over such limit temperature.

After cooling down, the synthesized powder is reground and the powder is isostatically pressed for about 10min in water to a pressure of approximately 50 MPa. The resulting cylindrical rods are sintered in a furnace, in a vertical position, at 980°C in air for 15h.
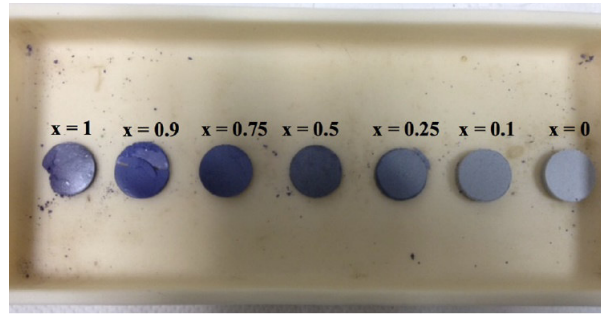
Figure 2.5: Photograph of $Ba_2Cu_{(1-x)}Mn_xGe_2O_7$ pellets synthesized. [88]

Polycrystalline samples (2g) of $Ba_2Cu_{(1-x)}Mn_xGe_2O_7$, with x=0, 0.1, 0.25, 0.5, 0.75, 0.9 and 1, are prepared by standard solid state reaction [88]. As starting materials, $BaCO_3$ (Sigma Aldrich 99.999%), CuO (MVLaboratories 99.9999%), $MnCO_3$ (99.99% AlfaAesar) and GeO_2 (Alfa Aesar,99.99%) are used. These starting materials are weighed out in a stoichiometric ratio and well mixed in an agate mortar. The $Ba_2Cu_{(1-x)}Mn_xGe_2O_7$ mixtures, pressed into pellets, are placed in an alumina crucible and heatedat 880°C, 950°C and 980°C for 15h each, with intermediate grindings. For x=0.75 an additional stepat 1050°C again for 15 h is also performed. The samples' color gradually changes with the composition from pale gray for $Ba_2CuGe_2O_7$ to blueviolet for $Ba_2MnGe_2O_7$,as can be observed in Fig. 2.5.

2.3.2 Crystal Growth

Peculiar physical properties of $Ba_2MGe_2O_7$ depend on the nature of the transition metal M, that therefore plays a central role. Considering that

in the periodic table, nickel is located exactly between cobalt and copper, it may be expected that also $Ba_2NiGe_2O_7$ (BNGO) should have interesting properties. While the other BMGO have been prepared since many years, BNGO is not synthesized yet. It has been theoretically proposed [65] that in BNGO, Jahn Teller effect could induce a structural distortion that lowers the symmetry from tetragonal to orthorhombic.

Regardless of the existence of pure BNGO phase, also the partial substitution of copper with nickel in the BCGO structure can be a fascinating topic of investigation. It be guessed that this replacement could lead to strong changes in the magnetic phase diagram and eventually to multiferroicity.

This work investigates about the crystal growth of $Ba_2Cu_{(1-x)}Ni_xGe_2O_7$ for the first time. As consequence of expected structural transition in BNGO, a miscibility gap should exist for some intermediate values of x in $Ba_2Cu_{(1-x)}Ni_xGe_2O_7$ system. As will be shown in the next chapter, this hypothesis is confirmed, therefore synthesis of single crystals of BNGO is not allowed.

In the following, crystal growth of $Ba_2Cu_{(1-x)}Ni_xGe_2O_7$ with $x = 0.05$, 0.06, 0.08, 0.1, 0.2, 0.3 is described. The growth is performed using floating zone method.

In literature, none previous report exists which describes the preparation of these single crystals, so the investigation starts from crystal growth results on pure $Ba_2CuGe_2O_7$.

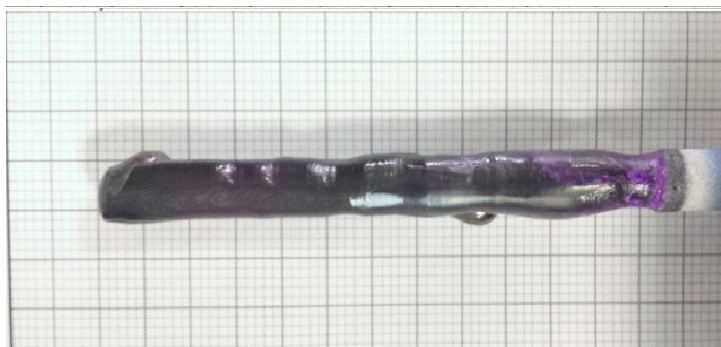Single crystals of $Ba_2Cu_{(1-x)}Ni_xGe_2O_7$, with x as indicated above, are produced using double elliptical mirrors (NEC Machinery, model SC1-MDH11020) image furnace. The growths are performed in dried air atmosphere of 5.5 bars. Crystals are grown at a rate of 0.5 mm/h and a rotation speed of 20-30 rpm, all growth experiments are summarized in Table 2.4. It shows that increasing nickel content the lamp voltage increases, so it deduces that samples with higher nickel doping melt at higher temperature.

The crystals obtained are around 5 mm in diameter and 60-70 mm in length (Fig. 2.6), with violet and transparent aspect (Fig. 2.7).

Batch	Sample	x	Voltage (V)	Rotation (rpm)	Comments
1	Ni0.05	0.05	27.1	25	Large transparent violet crystals
2	Ni0.06	0.06	27.4	25	Large transparent violet crystals
3	Ni0.08	0.08	27.6	25	Large transparent violet crystals
4	Ni0.1a	0.1	27.5	25	Large transparent violet crystals
5	Ni0.1b	0.1	27.6	25	Large transparent violet crystals
6	Ni0.2	0.2	28.7	20	Large transparent violet crystals
7	Ni0.3	0.3	31.1	20	Large transparent violet crystals
8	Ni0.5	0.5	32.0	25	Polycrystalline mixed phases

Table 2.4: Summary of $Ba_2Cu_{(1-x)}Ni_xGe_2O_7$ growth conditions. The crystals are grown in double elliptical mirrors image furnace, in an atmosphere of dried air (5.5 bars) with a speed of 0.5 mm\h.

Figure 2.6: As grown crystal of $Ba_2Cu_{(1-x)}Ni_xGe_2O_7$ with x=0.1.
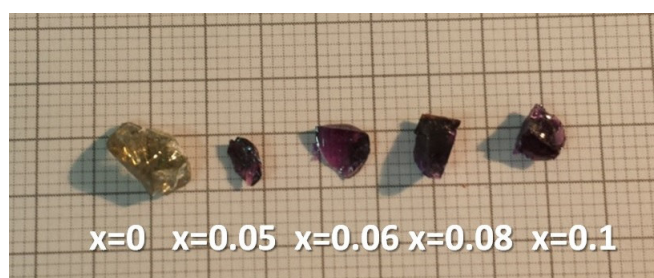
Figure 2.7: Crystal samples of $Ba_2Cu_{(1-x)}Ni_xGe_2O_7$.

2.4 $Cu_3Nb_2O_8$ preparation

2.4.1 Powder synthesis

Most of research on helimagnet $Cu_3Nb_2O_8$ investigates physical properties measured on powder samples. In literature, chemical phase diagram of $Cu_3Nb_2O_8$ is reported partially [89]. It shows that phase of $Cu_3Nb_2O_8$ is obtained by mixing CuO and Nb_2O_5 in stoichiometric ratio using the following reaction:

$$3CuO + Nb_2O_5 \rightarrow Cu_3Nb_2O_8 \qquad (2.1)$$
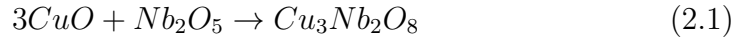
Reference [90] describes thermal steps to prepare polycrystalline powder of $Cu_3Nb_2O_8$. Therefore, starting from results reported in literature, we prepare $Cu_3Nb_2O_8$ as polycrystalline powder by heat treatments of starting materials CuO (MV Laboratories, 99.9999%) and Nb_2O_5 (Alfa Aesar, 99.9985%). They are mixed in agate mortar following the stoichiometric ratio shown above. Powder mixture is pressed into pellets and they are heated at 800°C for 36 h and at 950°C for 40 h with an intermediate grinding.
To perform a crystal growth, cylindrical rods with about 7mm in diameter and 70 mm long are realized through isostatic compression and heated at 950°C for 15 h in air.

2.4.2 Crystal Growth

As discussed in the section (1.7), there are many questions about helimagnet $Cu_3Nb_2O_8$. For example, it's not clear the cause of electric polarization **P** observation only when the magnetic structure becomes non-collinear. Moreover, it is expected that electric polarization **P** is in rotation plane of spin, but reference [10] shows that the electrical polarization is perpendicular to the plane of rotation of the spins and it develops below T∼25 K. Reference [10] is alone investigation on $Cu_3Nb_2O_8$ single crystal. This type of sample with millimetric size is vital to realize measurements along selected directions.
Crystal growth of $Cu_3Nb_2O_8$ is not reported in literature and this work investigates this topic for the first time. In the following, crystal growth of $Cu_3Nb_2O_8$ is described.
We employ the floating zone method using two types of optical image furnaces with elliptical mirrors. The first one is NEC Machinery (model SC1-MDH11020 at CNR-SPIN Salerno) with double-elliptical mirrors and two 2.0 kW halogen lamps. The second one has four elliptical mirrors (Crystal

System, model F-ZT-10000-H-IV-VPS at the University of Warwick) with four 500W halogen lamps. Several attempts of crystal growth are tried. Growth conditions are changed (including the speeds of the feed rod and the seed crystal, the counter-rotation speeds) to obtain large single crystals with high crystalline quality.

For all crystal growths, a polycrystalline powder rod is used as feed and a crystal from a previous growth with very quick rate (about 10 mm\h) is used as seed, all that make easy the production of a single crystal.

The entire set of growth parameters attempted are summarized in Table 2.5.

Batch	Growth speed	Rotation	Atmosphere (1 bar)	Comments
1*	3 mm\h	25 rpm	O_2 and $Ar^{\star\star}$	Polycrystalline powder
2*	2.5 mm\h	25 rpm	O_2 and $Ar^{\star\star}$	Small dark crystals
3*	2 mm\h	20 rpm	O_2 and $Ar^{\star\star}$	Large dark crystals
4*	2 mm\h	25 rpm	O_2 and $Ar^{\star\star}$	Large dark crystals
5	2 mm\h	20 rpm	Dried Air	Large dark crystals
6	2 mm\h	25 rpm	Dried Air	Large dark crystals

Table 2.5: Summary of $Cu_3Nb_2O_8$ crystal quality with varying growth conditions. The crystals labelled by the superscript* are grown using a four mirror furnace, while all the other growths are performed employing a two mirror furnace. ** growth is performed in a flux of 0,1 l\min of Ar and 12.7 cc\min of O_2.

We can see that crystal growth with translation speeds of 3 or 2.5 mm\h give polycrystalline powder (batches No.1) or small crystals (batches No.1-2). Using a lower translation speed, we get bigger and purer crystals (batches No.3-6). Moreover, from the results summarized in Table 2.5 we can deduce that the rotation speed doesn't influence the size of the crystals. However, a rotation speed greater than 25 rpm is not used because it destabilizes the molten zone during the crystal growth. When we use a rotation speeds of 30 or 35 rpm, the shape of the crystallization front changes and the molten zone is not stable. Therefore, 25 rpm is the rotation speed limit for a crystal growth.

Comparing the results for batches No.3-5 and No.4-6 we can see that single crystals of $Cu_3Nb_2O_8$ can be grown in dried Air or in a flux of 0,1 l\min of argon and 12.7 cc\min of oxygen.

Cleaving surface is thin and shiny. The single crystals realized with an image furnace with two mirrors (batches No.5 and No.6) show the same morphological features of the other ones.

An example of crystal samples of $Cu_3Nb_2O_8$ is showed in Fig. 2.8.

Figure 2.8: Crystal samples of $Cu_3Nb_2O_8$ from batch No.3

Compositional and structural studies of polycrystalline and crystalline samples

Large single crystals of helimagnetic compounds ($Ba_2CuGe_2O_7$ and $Cu_3Nb_2O_8$) are grown, as described in the last Chapter. High purity and quality of the produced samples are checked by compositional and structural studies, as shown in this Chapter. The characterization of these crystals allows to understand in more detail the complex crystal structure of compounds.
Synthesis of large single crystals allows us to investigate the fundamental physics of these materials.

3.1 Experimental procedures

Several types of experimental procedures are used to investigate chemical composition and crystal structure of samples. The following section gives a brief overview of each experimental procedure.

3.1.1 X-ray spectroscopy

X-ray spectroscopy includes several techniques for characterization of materials by using X-ray excitation. Mainly, in this work are used: powder X-ray diffraction, Laue technique and high resolution X-Ray diffraction.
The phase composition of polycrystalline and crystalline samples is checked by X-ray diffraction using a Bruker D5005 (at Warwick University) and a Bruker

D2-PHASER-2nd-generation (at Salerno University), X-ray powder diffractometers with Cu K_{α} radiation ($\lambda \sim$1.54 $\mathring{A}$). The θ-2θ scans are recorded from 10° to 110° using a step size at 0.02° and counting time of 10s for each step. Analysis of the data is processed using PANalyticals HighScore Plus suite [91] and Inorganic Crystal Structure Database. Powder refinement is performed using Rietveld analysis with Full-Prof software, based on standard algorithms employed in Rietveld refinement [92].

In order to determine a model that is compatible with the observed diffraction data, a Rietveld refinement may be performed. Accidental overlapping because of limited experimental resolution, considerable background difficult to define with accuracy, non-random distribution of the crystallites in the specimen (generally known as preferred orientation) may be some of the difficulties during the analysis of X pattern. One of the methods to solve these problems is the Rietveld analysis [93]. The Rietveld method refines user-selected parameters to minimize the difference between an experimental pattern (observed data) and a model based on the hypothesized crystal structure and instrumental parameters (calculated pattern). Whole diffraction pattern is analysed (not only the integrated intensities), the results give information about chemical composition (quantitative phase analysis), structural parameters (lattice parameters, atomic positions and occupancies) and other information, as for example grain size and macro micro-strain. The main advantage of this method is the reduced sensitivity to errors of the model and of the experimental setup. On the other hand, Rietveld refinement requires a starting model, a high quality X-ray spectrum and some experience with Rietveld programs which are not easy to use.

In addition to compositional and structural analysis through X-ray powder diffraction, single crystal samples are characterized by X-ray Laue technique. Laue analysis is used to determine the single crystals quality, the orientation and to align them along selected directions.

The Laue diffraction experiments are conducted on a high-resolution X-ray Laue camera (Photonic-Science, at Warwick University). The system is equipped with a goniometer can be used to align the samples along selected directions.

An X-ray beam is focused onto the sample and the resulting diffracted beams form arrays of spots on the TeGaOS scintillator which has a peak emission of 500nm which matches that of the CCD camera. The beam is not monochromatic, but a range of wavelengths, therefore a *white beam*, is used. Thus, many diffraction events happen simultaneously and a whole plane of reciprocal space can be probed in a single measurement. In detail, a white beam hits the crystal sample from the centre of the scintillator. The wide range

of wavelengths are then back scattered onto a screen. Crystal orientation is determined from the position of the spots. Each spot can be indexed and attributed to a particular plane. If there are defects (strain, multiple crystals with a boule) in the crystal then spots become distorted. Thus, Laue technique is useful to determine also the quality of a sample.

High Resolution X-Ray Diffraction is a technique used to obtain structural information and to investigate on crystal defects (misorientation, mosaic spread, surface damage etc.) [94]. The structure and crystalline quality of the crystals are assessed by a high resolution X-ray diffractometer (Philips, model X Pert MRD, at CNR-Spin-Salerno), with a Cu K_α source and a four-circle cradle allowing the sample to be tilted in Ψ and rotated in Φ besides be moved in ω; 2θ, X, Y and Z. The angles ω, 2θ, Φ and Ψ are used according to the standard definition in XRD: ω represents the angle between the sample surface and incident beam, 2θ the angle between the incident and diffracted beams, Φ the rotation angle around the sample surface normal, and Ψ the tilt angle about a line in the sample surface normal to the ω and 2θ axes [95]. The incident beam is defined by an asymmetrical four-crystal $Ge(2,2,0)$ monochromator coupled with a mirror so that the resultant beam has an angular divergence less than 12 arcsec in the diffraction plane [96].
This system can also map regions in reciprocal space around the Bragg reflections which can be useful to characterize relaxation of strained epitaxial films and carry out pole figure maps.
Different types of scans are available for high Resolution X-Ray diffraction. When a single crystal is investigated, the Rocking Curve (a plot of X-ray intensity vs. ω) is primarily used to study defects such as dislocation density, mosaic spread, curvature, misorientation, and inhomogeneity.

3.1.2 Electron spectroscopy

Scanning Electron Microscope (SEM) scans a sample with a focused electron beam and delivers images with information about sample's topography and composition. This examination gives information about morphology, composition and crystalline structure, through specific detectors applied to the instrument [97]. The resolution (depending on the application) that can approach 1nm.
Several types of electrons are generated as the result of specimen's bombardment by the electronic primary beam. These genereted electrons carry distinct structural information about the sample and differ from one another in origin, energy, and traveling direction. For example, *secondary electrons* are generated at a close proximity from the impact point and therefore they carry

high-resolution, surface-sensitive (topographic) information of the sample. They are low energy electrons ($<$50eV), while *backscattered electrons* are high energy electrons ($>$50eV) which result from elastic interactions between the incident electrons and the target specimen [98].

Moreover, the incident electrons on the sample surface produce also the emission of X-rays with discrete energies. Energy dispersive X-ray spectroscopy (EDS or EDX) and Wavelength dispersive X-ray spectroscopy (WDS or WDX) are powerful techniques that reveal what chemical elements are present in a particular specimen. Basically, they consist of detecting the characteristic X-rays produced by each element after bombarding a sample with high energy electrons. These techniques are used in combination and provide information about the elemental composition of a sample.

For the studies presented herein, a morphological study of crystal samples is performed by scanning electron microscopy (SEM, LEO EVO 50 at CNR-Spin-Salerno). This instrument has a large multi-ported specimen chamber with a 5-axis motorized sample stage. The vacuum system uses an oil-free turbomolecular pump. In this work, Sem morphological analysis is performed with electron accelerating voltages of 20 kV and with a working distance of 8,5 mm.

Integrated with the Zeiss SEM are an EDS system (Oxford INCA Energy 300) and an WDS system (Oxford INCA Wave 700). Both X-ray microanalysis systems have software for calculating sample composition. EDS can detect all elements with atomic number greater than or equal to 5 and with EDS system is also possible to perform elemental mapping and compositional line scans. EDS analysis is used to investigate volumes with dimensions of around 1 micron with a sensitivity of about 0.2wt%. The WDS system advantages are a lower limit of detection (about 100ppm) and a higher spectral resolution (FWHM$\sim$10eV) than EDS system.

Electron backscatter diffraction (EBSD) is a SEM based method that provides crystallographic data regarding the microstructure of a sample [99, 100]. EBSD allows to detect crystallographic orientations, misorientations, texture measurement, grain size and boundary types and chemical phases.

This method is based on the interaction between an electron beam and a slanted crystalline sample. Electrons are backscattered and diffracted according to Bragg's law, giving rise to diffraction patterns or Kikuchi bands. The diffracted electrons create a pattern (Kikuchi bands) that can be identified with a fluorescent screen (Fig. 3.1). The positions of the Kikuchi bands can thus be utilized to determine the orientation of the diffracting crystal, comparing the diffraction pattern that is collected with a simulated pattern [101].

Sem LEO EVO 50, is equipped also with EBSD detector (Inca Crystal 300).

In this work, this technique is used to detect the crystallographic orientation of cleaved pieces from crystals boules. Moreover, after careful mechanical polishing, the same crystals oriented by Laue technique, are also inspected by EBSD. During EBSD analysis, SEM works with electron accelerating voltages of 20 kV and with a working distance of 18,5 mm.
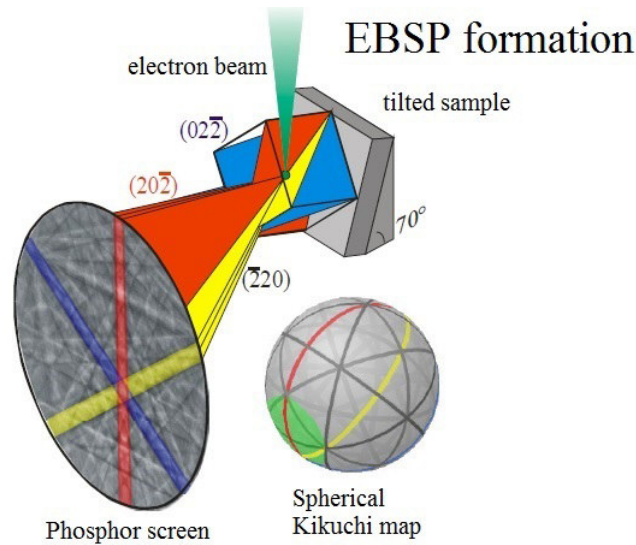
Figure 3.1: Electron backscatter pattern (EBSP) formation. The electron beam strikes the specimen and the scattering produces backscatter electrons in all directions. Electrons that travel along a crystallographic plane trace generate Kikuchi bands whose widths are dictated by the Bragg Law and specimen-to-phosphor screen distance. The electrons hit the screen phosphor and produce light which is detected by a CCD/SIT camera and converted to an digital image. This image is indexed and it allows to determine the orientation of sample.

3.2 Characterisation of polycrystalline samples

3.2.1 $Ba_2CuGe_2O_7$

Polycrystalline samples of $Ba_2CuGe_2O_7$ are prepared with two different methods, called A and B, (Section 2.2.1) [87]. In both methods, before the reactions, $BaCO_3$ is pre−annealed at 500°C for 1h, and then mixed with the other starting materials (GeO_2 and CuO), in stoichiometric proportions and heated. In method A, three thermal treatments at 850°C for 24h, 900°C for 24 h and 950°C for 15 h with intermediate grindings are performed. In method B both the $BaCO_3$ and the GeO_2 are pre-annealed, the latter at 800°C. After the pre-annealing, mixtures of starting materials in stoichiometric proportions are heated at 880° for 15 h, 950°C for 20h and 980°C for 60 h with intermediate grinding.

The XRD patterns of the samples produced by both processes are refined with a P -4 2_1m space group of tetragonal $Ba_2CuGe_2O_7$ [102], the Fig. 3.2 a) and the Fig. 3.2 b) show a comparison of the results [87].

Obtained pattern from powder of method A fits with $Ba_2CuGe_2O_7$ quite well, but X-ray spectrum shows some spurious peaks. A full profile matching is performed with FULLPROF [92, 106] code combining the major phase $Ba_2CuGe_2O_7$ with the possible unreacted starting oxides ($BaCO_3$, GeO_2 and CuO) or mixed phases ($CuGeO_3$, $BaGeO_3$, $Ba_3Ge_3O_9$, Ba_2CuO_3, $BaCu_2Ge_2O_7$, $BaCuO_2$). Spurious peaks have very low intensity, therefore several attempts to extract quantitative results about the amount of spurious phases are failed. Nevertheless, through a careful qualitative analysis of spectra, peaks of CuO, $Ba_3Ge_3O_9$ and $BaCu_2Ge_2O_7$ are indexed. It is concluded that method A synthesizes small amount of mentioned spurious phases together main phase of $Ba_2CuGe_2O_7$ (Fig. 3.3 a)).

Undesired phases are not found in X-ray spectrum of powder coming from method B, which shows only $Ba_2CuGe_2O_7$ phase (Fig. 3.3 b)).

Polycrystalline insulating samples are polished and coated with 20 nm layer of silver to perform EDS analysis. Comparing EDS compositional maps of method A (Fig. 3.4) and method B (Fig. 3.5) powders, emerges confirmation that method B powder does not contain spurious phases.

The distribution of chemical elements is not uniform in EDS compositional maps of method A powder. In the samples the stoichiometric ratio of the elements is different that the stoichiometric ratio in samples of method B. In Fig. 3.4 are shown the elemental maps acquired on a polycrystalline sample obtained via method A. There are large areas with a homogeneous composition

of $Ba_2CuGe_2O_7$ and few small domains rich in Cu or with $BaCu_2Ge_2O_7$,in agreement with the X-ray data. While in EDS maps of powder of method B (Fig. 3.5), there are not stoichiometric domains and distribution of Ba, Cu, Ge and O is uniform with the ratio expected namely. For these reasons, powder realized with method B is pure phase of $Ba_2CuGe_2O_7$.
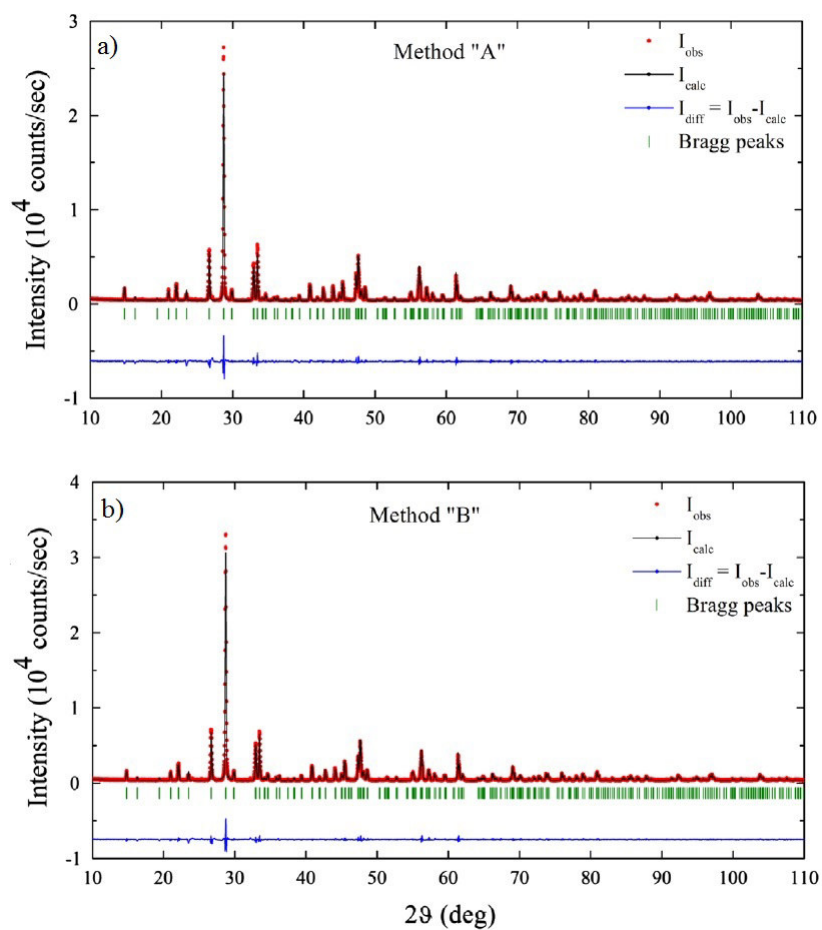
**Figure 3.2:** XRD data refinement of the powder from method A a) and method B b) [87]
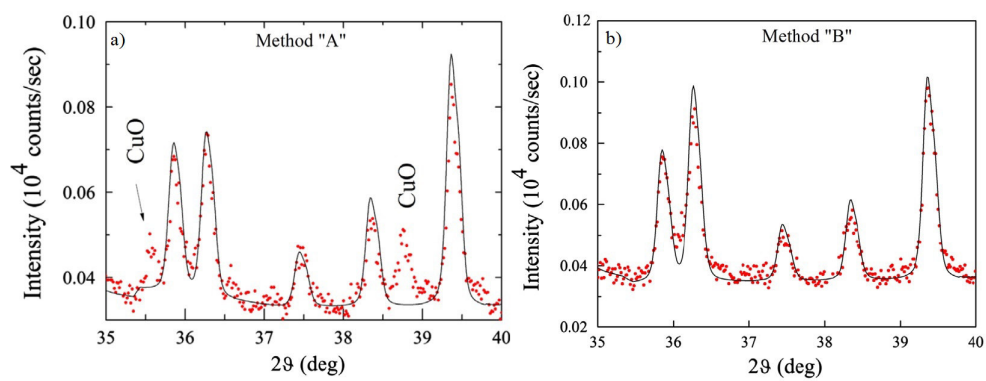
Figure 3.3: A zoom of the observed X-ray diffraction pattern of the powder from method A a) and method B b). No spurious peaks from unreacted CuO phase can be seen in method B [87].
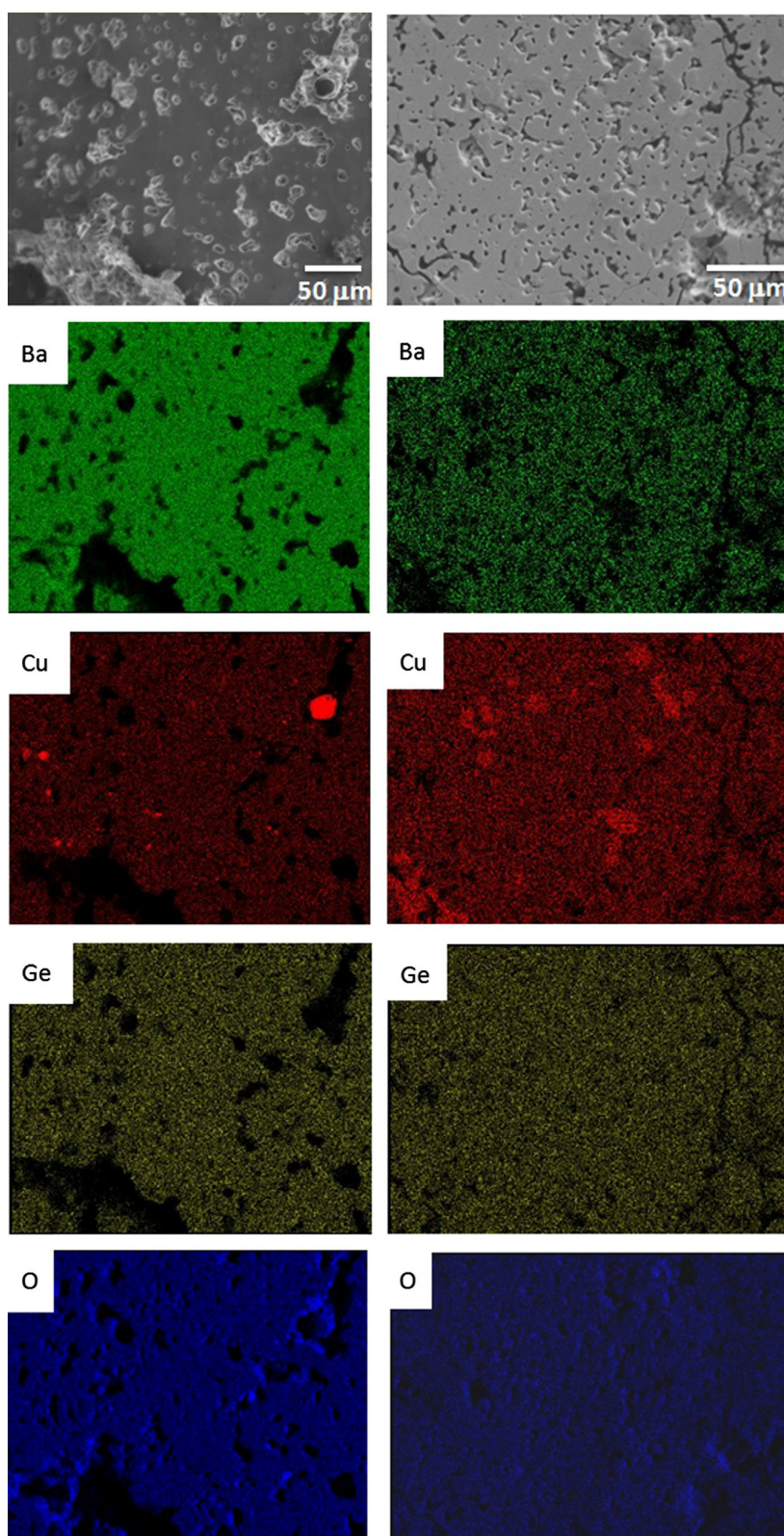
Figure 3.4: SEM image and EDS compositional map of $Ba_2CuGe_2O_7$ polycrystalline samples synthesized using method A. Left panels: small regions with deficiency of Ba and Ge and rich in Cu are visible. Right panels: in the regions rich in Cu a deficiency of Ba is observable, while Ge and O are homogeneous. Quantitative EDS results of these off stoichiometric domains gave the composition of $BaCu_2Ge_2O_7$ [87].
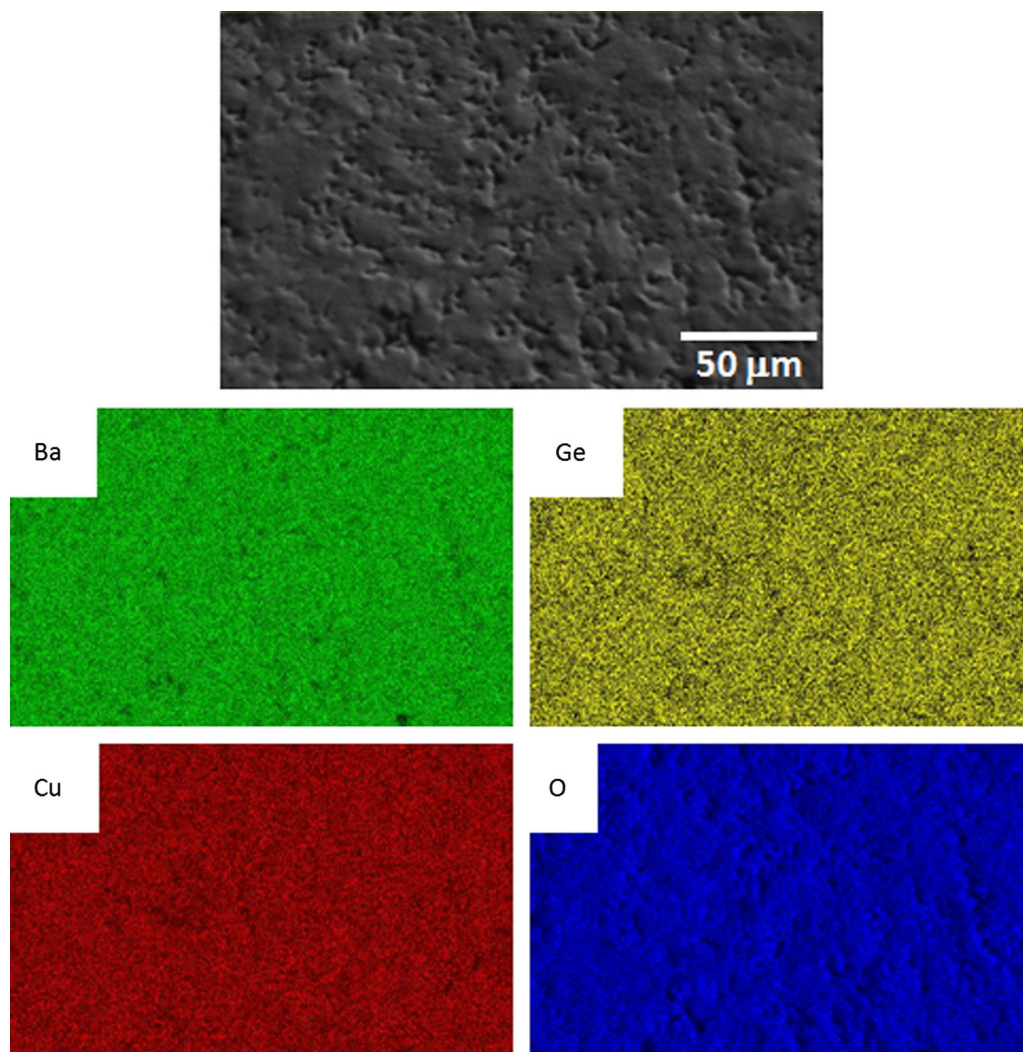
Figure 3.5: SEM image and EDS compositional map of a $Ba_2CuGe_2O_7$ polycrystalline sample synthesized via method B. A uniform distribution of the elements Ba,Cu,Ge and O, corresponding to the expected atomic ratio of 2:1:2:7 is observed [87].

3.2.2 $Ba_2Cu_{(1-x)}Ni_xGe_2O_7$

Polycrystalline samples of $Ba_2Cu_{(1-x)}Ni_xGe_2O_7$ (BCNGO) are prepared by method illustrated in the Section 2.3.1. It has been theoretically proposed [65] that Jahn Teller effect could induce a structural distortion that lowers the symmetry from tetragonal ($Ba_2CuGe_2O_7$, $x=0$) to orthorhombic ($Ba_2NiGe_2O_7$, $x=1$). As will be discussed below, the consequence of expected structural transition in $Ba_2NiGe_2O_7$ is that a miscibility gap exists for some intermediate values of x in $Ba_2Cu_{(1-x)}Ni_xGe_2O_7$ system. The results of this work show that the limit of solubility is $x \sim 0.3$.

Powders are analysed by X-ray powder diffraction and the profiles are shown in Figure 3.6. In all cases, except for $x = 1$, the peaks are easily recognized and they are indexed using the space group P-42$_1$m. In X-ray patterns, the peaks shift in a systematic way, therefore a solid solution $Ba_2Cu_{(1-x)}Ni_xGe_2O_7$ forms for any composition x. For $x \leq 0.3$, all diffraction peaks are indexed using ones of $Ba_2CuGe_2O_7$ phase with a systematic shift on 2θ. This result indicates that the powders contain only solid solution $Ba_2Cu_{(1-x)}Ni_xGe_2O_7$ without secondary phases. For $x \geq 0.4$, the X spectra of samples show peaks of $Ba_3Ge_3O_9$, NiO and $BaCu_2Ge_2O_7$ in addition to main phase, with different intensity depending of x.

X-ray patterns are analysed using Rietveld refinement, two examples of fit are shown in Fig.3.7 a) (sample Ni0.05) and in Fig.3.7 b) (sample Ni0.6). Below, a quantitative analysis of composition of samples is discussed.

For powders with $x \leq 0.3$, Rietveld results confirm that no spurious phases are detected. All peaks of X patterns have Bragg positions of $Ba_2CuGe_2O_7$ with a systematic shift on 2θ, no peak shows a different Bragg position, therefore Rietveld code is written with alone $Ba_2Cu_{(1-x)}Ni_xGe_2O_7$ phase.

At $x=0.4$, main phase is $Ba_2Cu_{(1-x)}Ni_xGe_2O_7$, but just small amounts of secondary phases ($Ba_3Ge_3O_9$ and $BaCu_2Ge_2O_7$) are observed. For higher doping, the $Ba_2Cu_{(1-x)}Ni_xGe_2O_7$ solid solution is still present, but its quantity decreases, while the concentration of the secondary phases greatly increases. For $x=0.6$ and for $x=0.8$, the amount of $Ba_2Cu_{(1-x)}Ni_xGe_2O_7$ is about 75% and 50% of total weight, respectively; while $Ba_3Ge_3O_9$ and unreacted NiO are detected in both cases. These spurious phases show higher percentage in powder with $x=0.8$. Finally, for $x = 1$ the X pattern is completely different and the main phase is $Ba_3Ge_3O_9$. Quantitative results are reported in Table 3.1.

We conclude that for the $Ba_2Cu_{(1-x)}Ni_xGe_2O_7$ phase, the higher nickel content reduces purity of polycrystalline samples. $Ba_2Cu_{(1-x)}Ni_xGe_2O_7$ is a solid solution with solubility limit x$\sim$ 0.3.

Since a complete solid solution along the entire range of compositions does

Sample	BCNGO(%)	$Ba_3Ge_3O_9$(%)	NiO (%)	$BaCu_2Ge_2O_7$ (%)
Ni0.05	100.00	——	——	——
Ni0.1	100.00	——	——	——
Ni0.3	100.00	——	——	——
Ni0.4	89.13(2)	9.14(1)	——	1.73(1)
Ni0.6	75.24(1)	19.73(4)	5,03(3)	——
Ni0.8	49.93(1)	38.08(4)	12.00(1)	——

Table 3.1: Quantitative phase results from Rietveld analysis.

Sample	$a = b(\mathring{A})$	$c(\mathring{A})$	χ^2	GOF
Ni0.05	8.4597(2)	5.4445(8)	1.68	1.2
Ni0.1	8.4592(1)	5.4517(9)	1.64	1.5
Ni0.2	8.45247(8)	5.4553(3)	2.37	1.5
Ni0.3	8.44749(2)	5.46170(2)	1.71	1.5
Ni0.4	8.4485(9)	5.4643(1)	1.61	1.3
Ni0.6	8.4467(7)	5.4645(2)	1.93	1.4
Ni0.8	8.4494(7)	5.4683(1)	12.7	4.9

Table 3.2: XRD refinement data of $Ba_2Cu_{(1-x)}Ni_xGe_2O_7$ samples. χ^2 and parameter of Goodness Of Fit (GOF) increase with nickel amount, infact for higher x the fit is not perfect, due to spurious phases.

not form, this could confirm the phase of $Ba_2NiGe_2O_7$ would have a different crystal structure from the other $Ba_2MGe_2O_7$ compounds. As mentioned in Chapter 1, the phase formation of $Ba_2NiGe_2O_7$ is theoretically expected, but it is not yet observed experimentally [65]. In the XRD profile of x=1, there is no evidence of any phase that could put in relation with the $Ba_2CuGe_2O_7$ structure. However, it is not possible to realize a satisfactory fit of the experimental diffractogram, which on the contrary shows only the presence of $Ba_3Ge_3O_9$ and unreacted NiO. There is not clue of the presence of $Ba_2NiGe_2O_7$, that likely could not be synthesized, at least by standard solid state route.

Analysis through Rietveld refinement allows to estimate cell parameters (summarized in Table 3.2). Fig. 3.8 shows such parameters of $Ba_2Cu_{(1-x)}Ni_xGe_2O_7$ as a function of Ni content.

Addition of nickel to structure involves a linear stretching of c-axis and a parallel shortening of a-axis. For x>0.3, the cell parameters keep constant indicating that the solubility limit of nickel in $Ba_2CuGe_2O_7$ is around this value.
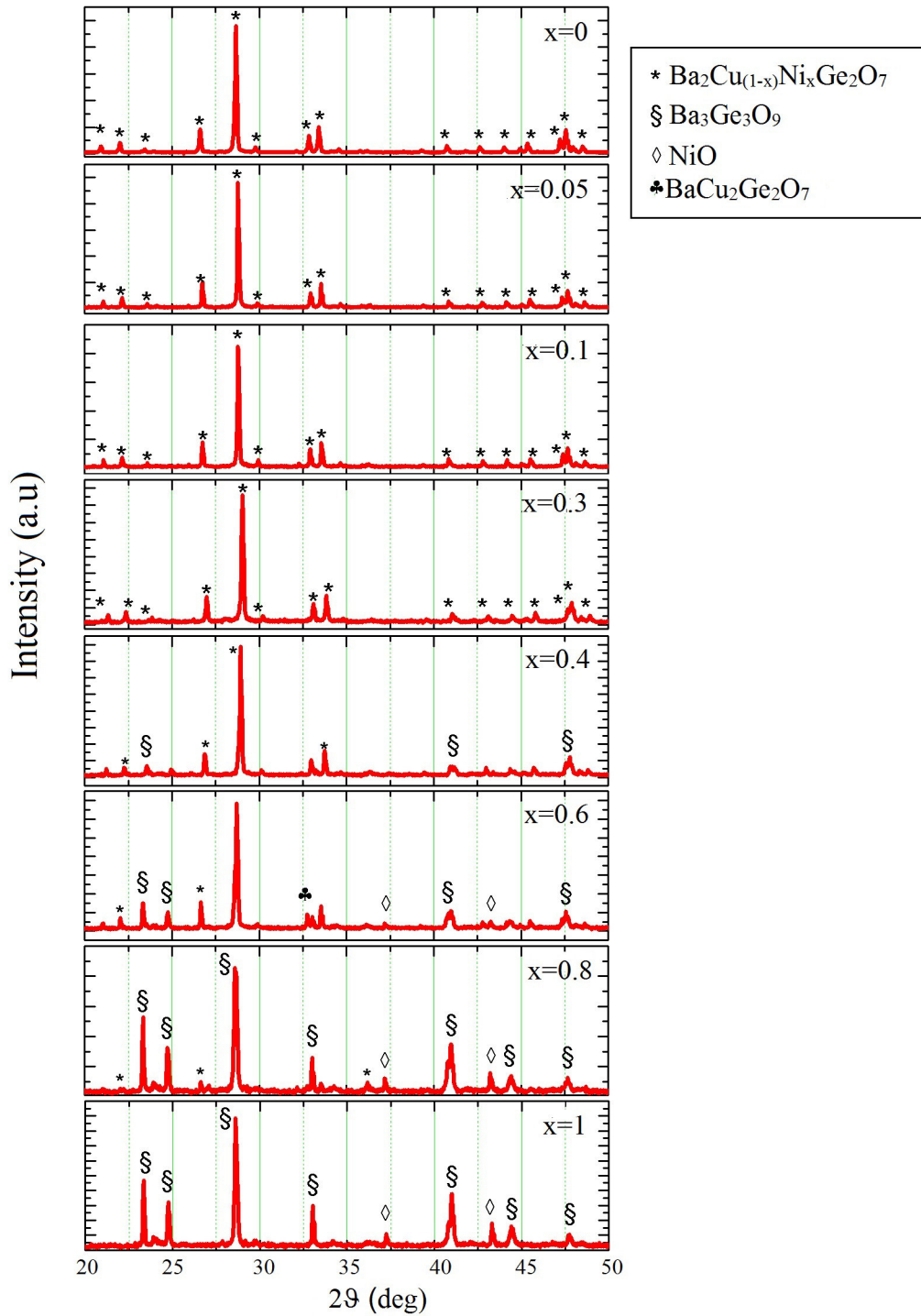
Figure 3.6: XRD patterns of $Ba_2Cu_{(1-x)}Ni_xGe_2O_7$. Zero of Instrument is corrected through profile matching analysis between $Ba_2Cu_{(1-x)}Ni_xGe_2O_7$ expected phase and experimental data. Increasing Ni content a shift of the BCNGO peaks is observed, for $x \geq 0.4$ $Ba_3Ge_3O_9$ and unreacted NiO appeared in XRD pattern. Their intensity increased with Ni percentage.
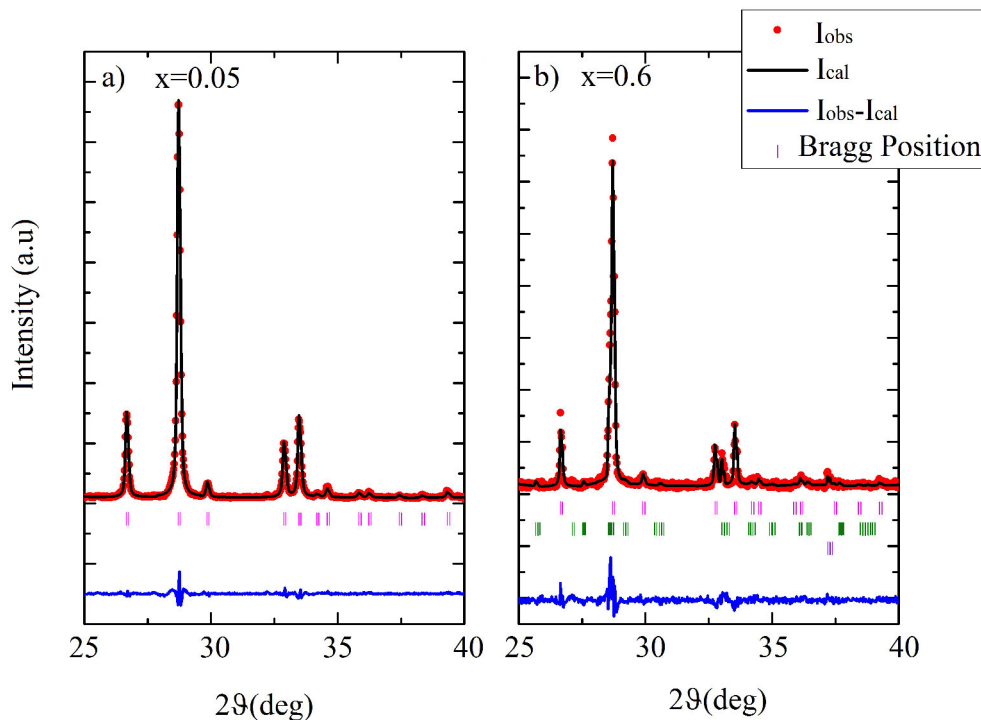
Figure 3.7: Observed (red points) and refined (black curve) X-ray powder diffraction pattern of Ni0.05 (a) and Ni0.6 (b) samples. Colored bars below the patterns mark the Bragg peak positions. a) The best fit results for an analysis with a single phase ($Ba_2Cu_{0.95}Ni_{0.05}Ge_2O_7$, space group P-$42_1m$) b) Spectrum shows a good refinement using three phases: $Ba_2Cu_{0.4}Ni_{0.6}Ge_2O_7$, $Ba_3Ge_3O_9$, NiO, their Bragg positions are indicated in the Rietveld patterns with bars respectively from top to bottom. Intensity is not fitted perfectly, it is an index that powder contained an amount of different phases.
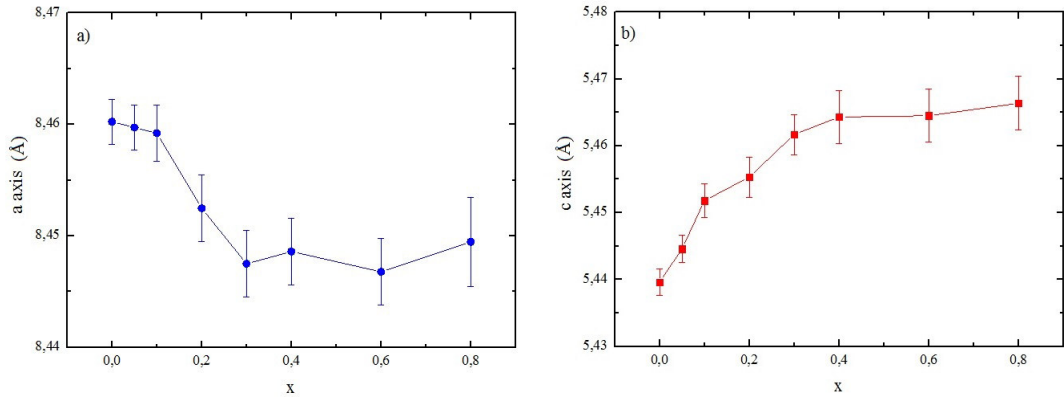
Figure 3.8: Cell parameters (blue for a-axis and red for c-axis) of $Ba_2Cu_{(1-x)}Ni_xGe_2O_7$ as a function of substituted Ni content.

3.2.3 $Ba_2Cu_{(1-x)}Mn_xGe_2O_7$

Fig. 3.9 shows the XRD patterns of $Ba_2Cu_{(1-x)}Mn_xGe_2O_7$ polycrystalline samples prepared as described in Section 2.3.1 [88].

$Ba_2Cu_{(1-x)}Mn_xGe_2O_7$ solid solution forms for any doping x as results from analysis of patterns which are indexed as belonging to the expected phase. Peaks shift in a systematic way (Fig. 3.9). Such result is in agreement with literature which reports only $Ba_2CuGe_2O_7$ [59] (x=0) and $Ba_2MnGe_2O_7$ [57] (x=1), these are the extremes of solid solution $Ba_2Cu_{(1-x)}Mn_xGe_2O_7$.

Since all peaks are indexed in all $Ba_2Cu_{(1-x)}Mn_xGe_2O_7$ solid solutions in the x range (0,1), no rietveld analysis is performed. Fig. 3.10 shows the dependence of the cell parameters as function of the content of the manganese. Cell parameters a and c obtained are in agreement with the ones reported in literature for $Ba_2CuGe_2O_7$ [59] (x=0) and for $Ba_2MnGe_2O_7$ [57] (x=1).

The obtained cell parameters of the pure ends (x=0 and x=1) are a=8.467 $\mathring{A}$, c=5.441$\mathring{A}$ and a=8.479$\mathring{A}$, c=5.527$\mathring{A}$, respectively. In Fig.3.10 a-axis shows a constant behaviour while c-axis shows an increasing trend. As consequence, also the cell volume increases as function of x, in agreement with the Vegard's law.

EDS analysis is performed on samples coated with a layer of 20 nm silver, the results are summarized in Table 3.3 and confirm the chemical composition expected.
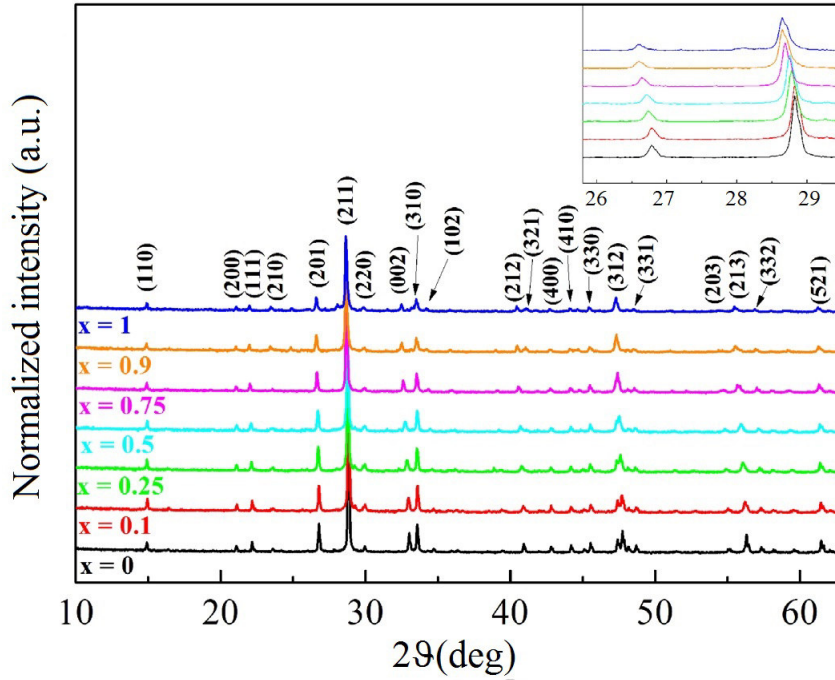
Figure 3.9: XRD patterns of $Ba_2Cu_{(1-x)}Mn_xGe_2O_7$ compounds. In the upper panel a zoom of XRD data shows the systematic shift of the peaks. [88]
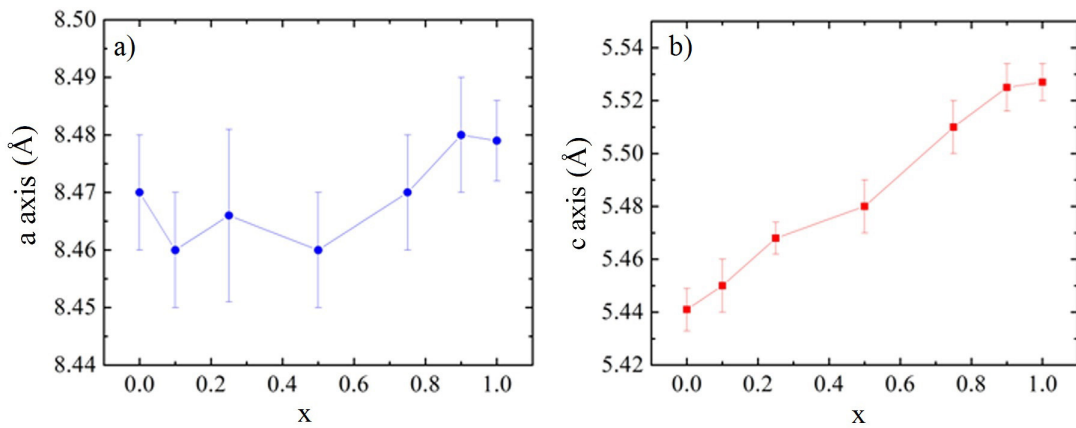
Figure 3.10: Evolution of the cell parameters of $Ba_2Cu_{(1-x)}Mn_xGe_2O_7$ compounds as a function of substituted Mn content(x). Changes of (a) a-axis and (b) c-axis with doping [88].

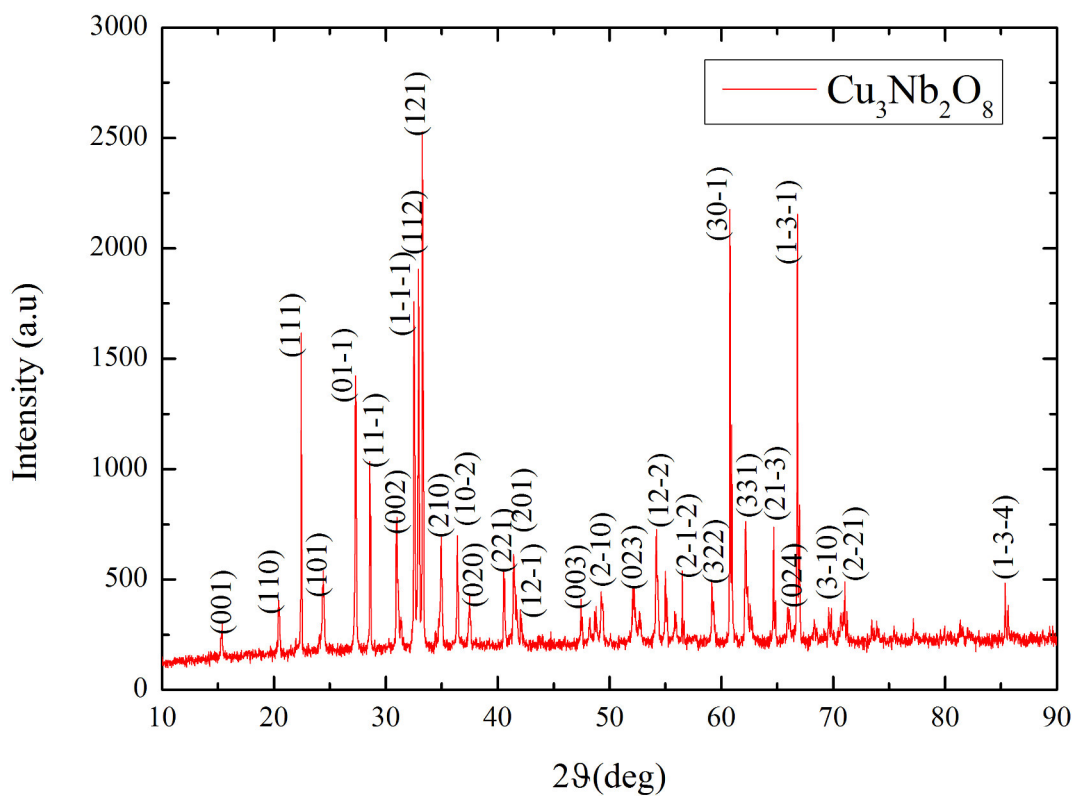| Composition	EDS results
x=0	$Ba_{2.0\pm0.1}Cu_{0.95\pm0.05}Ge_{2.0\pm0.2}O_{6.6\pm0.7}$
x=0.1	$Ba_{1.9\pm0.5}Cu_{0.8\pm0.2}Mn_{0.07\pm0.02}Ge_{2.0\pm0.7}O_{6.2\pm0.6}$
x=0.25	$Ba_{2.0\pm0.4}Cu_{0.6\pm0.2}Mn_{0.3\pm0.08}Ge_{2.0\pm0.4}O_{6.2\pm0.8}$
x=0.5	$Ba_{2.1\pm0.4}Cu_{0.5\pm0.1}Mn_{0.49\pm0.08}Ge_{2.0\pm0.4}O_{6.9\pm0.4}$
x=0.75	$Ba_{1.8\pm0.6}Cu_{0.25\pm0.11}Mn_{0.60\pm0.15}Ge_{2.0\pm0.9}O_{7.2}$
x=0.9	$Ba_{2.2\pm0.2}Cu_{0.12\pm0.02}Mn_{0.80\pm0.15}Ge_{2.0\pm0.2}O_{6.7}$
x=1	$Ba_{1.8\pm0.7}Mn_{0.8\pm0.2}Ge_{2.0\pm0.8}O_{7.7\pm0.4}$

Table 3.3: Compositional results obtained by EDS analysis

3.2.4 $Cu_3Nb_2O_8$

Polycrystalline samples of $Cu_3Nb_2O_8$ are prepared by method illustrated in the Section 2.4.1. X-ray diffraction pattern is acquired by Bruker D2 diffractometer.

The XRD pattern of a sample is indexed through the P -1 space group of triclinic $Cu_3Nb_2O_8$ [10] (Fig. 3.11).

All peaks belong to the expected phase and no spurious phase is detected. Polycrystalline samples of $Cu_3Nb_2O_8$ are analysed also by EDS analysis. Therefore, the insulating surfaces are polished and coated with 20 nm layer of silver. The ratio averages to 3:2 for Cu:Nb, confirming high purity of samples.

Figure 3.11: Indexed XRD patterns of $Cu_3Nb_2O_8$.

3.3   Compositional and structural study of single crystals

3.3.1 $Ba_2CuGe_2O_7$

As discussed in Section 3.1.2, results of analysis on $Ba_2CuGe_2O_7$ polycrystalline powder of method B show that this powder is purer than $Ba_2CuGe_2O_7$ polycrystalline powder of method A.

$Ba_2CuGe_2O_7$ crystal samples grown by floating zone technique are listed in Table (2.3) of the previous Chapter. Samples are realized using different conditions of crystal growth. Below, a compositional and structural characterization of samples is provided to identify the best growth parameters of $Ba_2CuGe_2O_7$.

Looking at the last column Table (2.3) it is evident that the best crystals are achieved starting from feed rods obtained using method B. To check the quality of grown crystals, a careful inspection by optical microscopy of all crystal batches is performed.

As mentioned, for fast growth speed (batches No. 1 and 2) no single crystals are observable.

Optical microscopy inspection of crystals batches from No.3 to No.6 reveals the presence of small transparent yellowish crystals surrounded by a darker outer layer. Rectangular crystals are isolated with size of about 4mm in length and 2×1 mm^2 in cross section. For batches from No.9 to No.13, optical microscopy investigation reveals the presence of large transparent and homogeneous yellowish crystals.

The XRD pattern of powdered crystals from batches No. 1 and 2, show many diffraction peaks not belonging to the $Ba_2CuGe_2O_7$ phase. Some of the peaks are indexed with Cu_2O phase, observable in some areas of the as grown boule as small red patches.

In the case of crystals from No.3 to No.6 the mentioned darker outer layer is object of interest. XRD experiments performed on these crushed crystals show only diffraction peaks of $Ba_2CuGe_2O_7$ phase, confirming the single phase nature of these batches.

Crystals from batches No.7 and 8 are characterized by a dark yellow coloured boule. In these cases, XRD patterns on powder coming from crystals show diffraction peaks matching with of $Ba_2CuGe_2O_7$. As mentioned, it is concluded that dark colour of the boule does not arise due to a secondary phase but may be due to a slight off stoichiometry of oxygen.

The Rietveld refinement of XRD pattern of crushed transparent yellowish crystals from the batch No.12 show diffraction peaks, all of them could

be indexed to the $Ba_2CuGe_2O_7$ phase, meaning that transparent yellowish $Ba_2CuGe_2O_7$ crystals are the pure phase. Since there are no reported values of the anisotropic thermal displacement parameters available for the $Ba_2CuGe_2O_7$ phase, the refinement code of such parameters starts from parameters of $Ba_2CoGe_2O_7$ [103].

A careful analysis of our Rietveld refinement shows that the mismatch between the calculated and the measured intensities comes mostly from the limit in the definition of the thermal displacement parameters when refining a pattern obtained using a standard X-ray laboratory diffractometer. A more accurate evaluation of these parameters needs synchrotron or neutron diffraction patterns. In Table 3.4 are summarized the refined lattice parameters obtained for polycrystalline and single crystal samples. The crystallographic data are in agreement with reported values [102].

The compositional analysis of the crystals by WDS is carried out on various regions of selected crystals from different batches (No. 9-13).

The atomic percentage obtained normalizing WDS data to the stoichiometric value of Ba= 2 is $Ba_{2.00\pm0.03}Cu_{1.02\pm0.02}Ge_{2.04\pm0.03}O_{7.2\pm0.1}$.

WDS analysis on the dark yellow crystals (batches No. 7, 8) reveal an excess of oxygen in these crystals.

Natural preference for the crystal boule to cleave is not observed and crystals are orientated by Laue technique. In detail, samples of few mm^3 from batches No 6,10 and 11 oriented using the X-ray Laue technique are cut parallel to (0,0,1) or (0,1,0) planes and their surfaces are mirror polished. In Fig. 3.12(a) and (b) are shown the Laue photographs of two samples surfaces with (0,0,1) and (0,1,0) planes being orthogonal to the X-ray beam, respectively.

The excellent quality of the crystals is confirmed by high resolution X-ray diffraction measurements. In Fig. 3.13 is shown the rocking curve of the (0,0,2) reflection proving the high crystallinity of the grown $Ba_2CuGe_2O_7$ crystals . After careful mechanical polishing, the same crystals oriented by Laue technique, are also inspected by electron back scattered diffraction (EBSD) technique.

EBSD is used to further characterize the microstructure of our crystals and to identify, possibly, the presence of grains or of spurious phases. Fig. 3.14 shows an EBSD pattern of a crystal from batch No.10, the Kikuchi bands are bright and in good contrast against background. An example of EBSD micrographs is reported in Fig. 3.15. Fig. 3.15 b) reveals that all surface shows $Ba_2CuGe_2O_7$ chemical phase. Moreover, this technique enable to drawing the orientation maps for the selected surface.

The orientation maps (Fig. 3.15 c),d),e)) are based on the sample normal (ND), rolling (RD) and transverse (TD) directions. In each point of the map, the crystallographic direction corresponding to the particular sample direction

Sample	a=b ($\mathring{A}$)	c ($\mathring{A}$)	GOF
Method A	8.45930(5)	5.43940(4)	2.24
Method B	8.46023(5)	5.43962(4)	2.10
Powdered crystal (batch No.12)	8.46013(1)	5.44003(7)	3.67

**Table 3.4:** XRD refinement data of $Ba_2CuGe_2O_7$ samples.

is calculated, and a colour allocated according to its position in the inverse pole figure. Fig. 3.16 shows inverse pole figure of $Ba_2CuGe_2O_7$. The inverse pole figure is coloured by a mix of red, green and blue depending on the position in the stereographic triangle. This acts as a colour key to determine the colour of the ND, RD and TD orientation maps at the analysed point. The orientation maps of a crystal from batch No.10 are showed in Fig. 3.15 c),d),e). They reveal that there is the same crystallographic orientation on all surface. Moreover, the single crystal shows a and b axes on plane while c axis is perpendicular to surface.
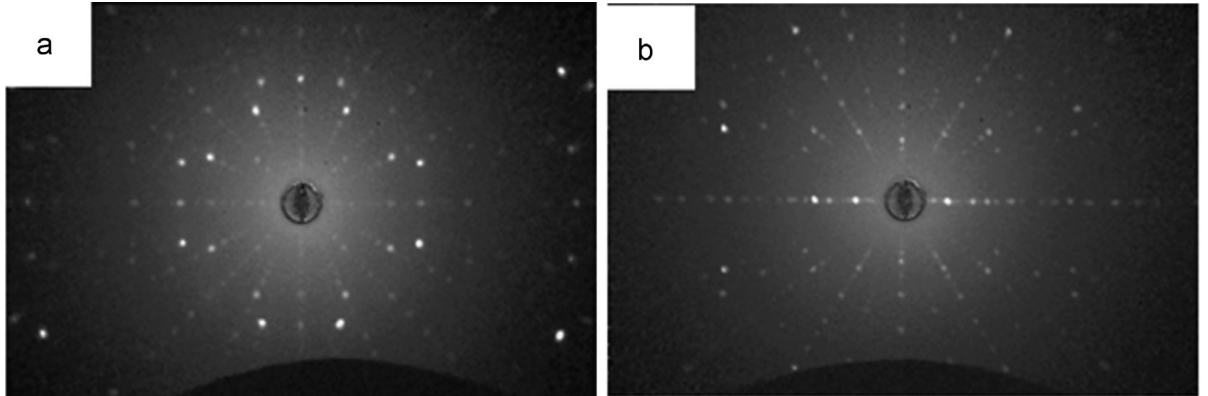

Figure 3.12: X-ray Laue patterns of $Ba_2CuGe_2O_7$ crystals oriented with the(a)[0,0,1](batch No.10) and (b)[0,1,0](batch No 11)direction orthogonal to the exposed surface.
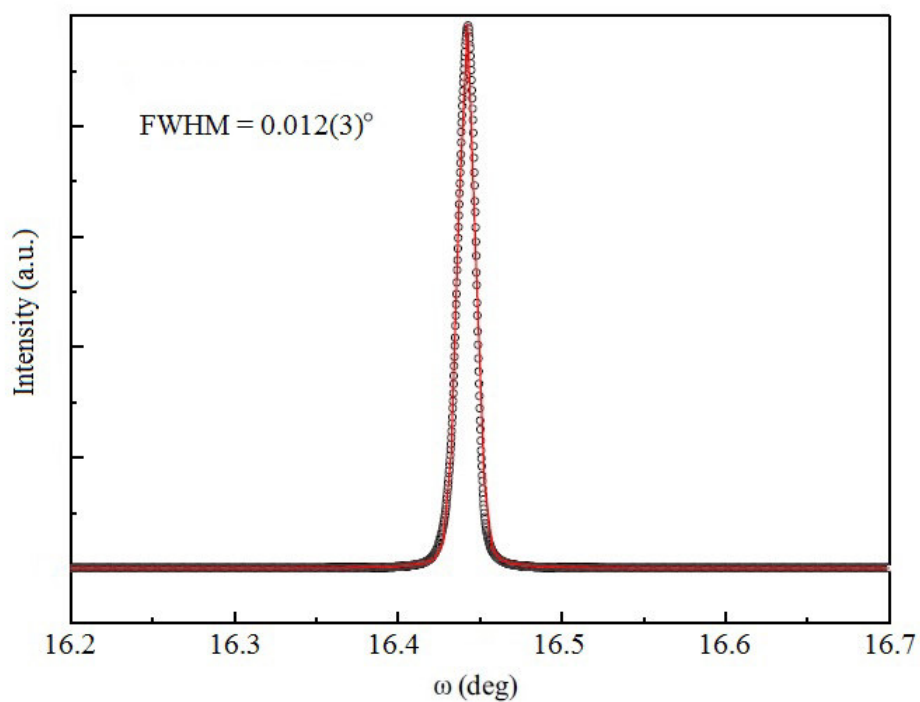
Figure 3.13: Rocking curve of the (0,0,2) reflection acquired on a $Ba_2CuGe_2O_7$ single crystal (batch No.10) The line is a fit with a pseudo-Voigt curve.
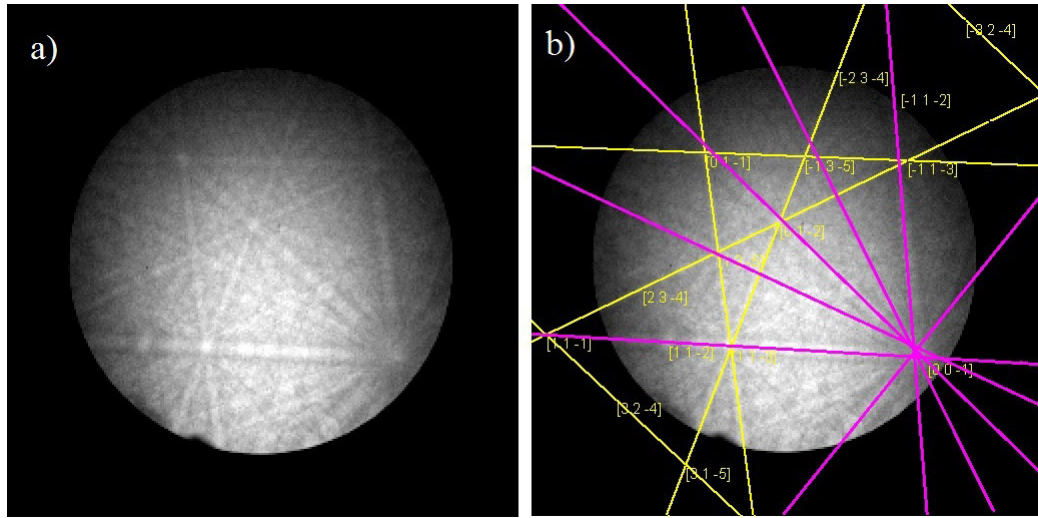
Figure 3.14: a) EBSD pattern acquired on a $Ba_2CuGe_2O_7$ single crystal (batch No.10). b) Indexed EBSD pattern. Yellow lines indicate the indexed Kikuchi bands while pink lines indicate revealed Kikuchi bands, but they are not indexed.
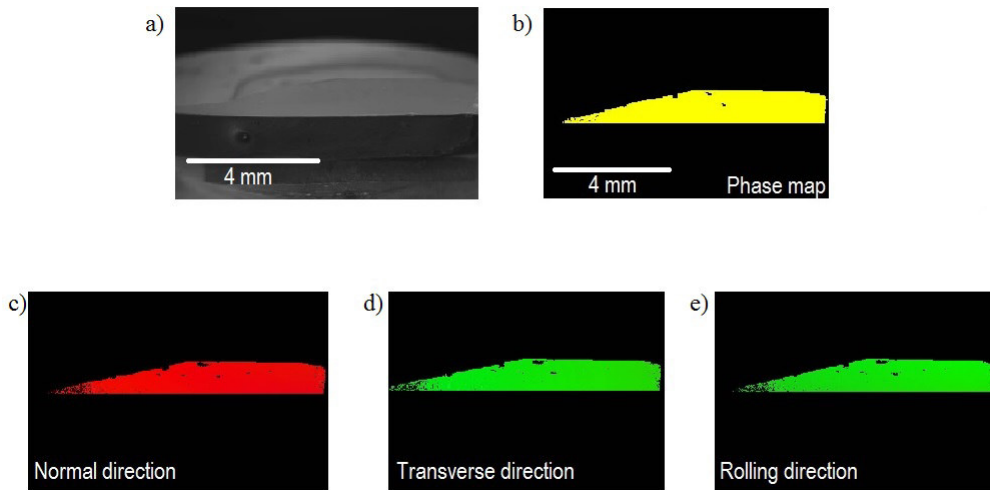
Figure 3.15: a) SEM image of $Ba_2CuGe_2O_7$ single crystal (batch No.10) where EBSD pattern is acquired. b) Phase map of crystal. Only $Ba_2CuGe_2O_7$ phase is revealed (yellow colour). c),d),e) Orientation maps along Normal, Transverse and Rolling directions, respectively.
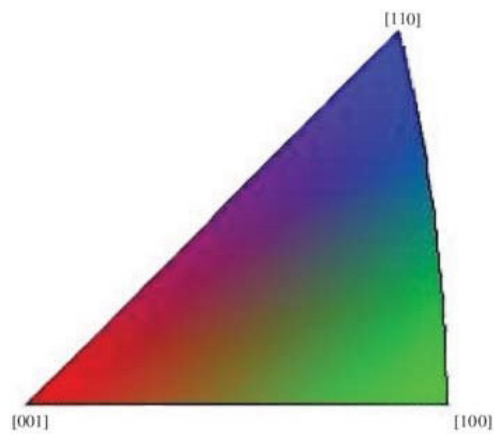
Figure 3.16: Inverse pole figure of $Ba_2CuGe_2O_7$. The inverse pole figure is colored by a mix of red, green and blue depending on the position in the stereographic triangle.

3.3.2 $Ba_2Cu_{(1-x)}Ni_xGe_2O_7$

As mentioned in Section 3.2.2, the results of study on polycrystalline powders of $Ba_2Cu_{(1-x)}Ni_xGe_2O_7$ show that not whole stoichiometry of x in (0,1) range is allowed being x=0.3 is the solubility limit of this solid solution. For these reasons, single crystals of $Ba_2Cu_{(1-x)}Ni_xGe_2O_7$ are grown by floating zone technique in x range from 0.05 to 0.3.
$Ba_2Cu_{(1-x)}Ni_xGe_2O_7$ single crystals are listed in Table (2.4).
Optical microscopy inspection of Ni0.05 to Ni0.8 crystals reveals the presence of large transparent violet crystals with dimensions similar to those of the parent compound. Rectangular crystals are isolated with size of about 4mm in length and 2×1 mm^2 in cross section. Some crystal samples from these batches are surrounded by a darker outer layer. Similarly to the $Ba_2CuGe_2O_7$ single crystals, XRD experiments performed on these crushed crystals confirm the single phase nature.
For samples Ni0.1a and Ni0.1b optical microscopy investigation reveals the presence of transparent violet crystals. In this case, crystals are isolated with size of about 3mm in length and 1×1 mm^2 in cross section.
From batches of Ni0.2 and Ni0.3 rectangular crystals are isolated similarly to Ni0.1 ones, microscopic analysis shows that some samples are surrounded by a darker outer layer.
More detailed morphological inspection is carried out using electronic microscope. SEM images are taken on several samples with different Ni doping. All surfaces investigated don't show grain boundaries, inclusions, or defects. Several SEM images are taken with variable magnification, some examples are showed in Fig. 3.17, 3.18. Cleaved surfaces illustrated show perfectly flat areas and smooth crystallographic terraces.
The XRD pattern Rietveld refinement of crushed transparent crystals from each batch, except for Ni0.5, shows diffraction peaks, all indexed with $Ba_2CuGe_2O_7$ phase, which means that crystals are pure phase of solid solution of $Ba_2Cu_{(1-x)}Ni_xGe_2O_7$.
In Table 3.5 are summarized the refined lattice parameters, these results confirm those obtained for polycrystalline samples. In fact, the study of polycrystalline samples shows that for $x \leq 0.3$ the addition of nickel to structure involves a linear stretching of c-axis and a parallel shortening of a-axis. The same behaviour is observed in single crystals, as shown in Fig. 3.19.
EDS analysis is performed on many areas of all the samples and their compositions are very close to the nominal ones, as reported in Table 3.6. Each sample is coated with a thin layer (20 nm) of silver to get a metallic surface. No spurious elements are detected, confirming the high quality of the obtained compounds.

Also, compositional WDS analysis (Tab. 3.7) is carried out on various regions of selected crystals with quantitative results that confirm EDS ones.

Samples of few mm^3 from crystals Ni0.05, Ni0.0.06, Ni0.08 and Ni0.1 oriented using the X-ray Laue technique, are cut parallel to (0,0,1) or (0,1,0) planes and their surfaces are mirror polished. Fig. 3.20 shows the Laue photograph of (0,0,1) plane. Considering a selected crystallographic direction, the position of the spots in Laue pattern acquired on $Ba_2Cu_{(1-x)}Ni_xGe_2O_7$ single crystal is similar to that shown in Laue pattern acquired on $Ba_2CuGe_2O_7$. Indeed, Fig. 3.20 shows the Laue photograph of (0,0,1) plane acquired on Ni0.06 crystal. This Laue pattern is similar to that shown in the case of $Ba_2CuGe_2O_7$ (Fig. 3.12 of the previous Section). This result confirms that $Ba_2Cu_{(1-x)}Ni_xGe_2O_7$ compounds have a crystal structure with same space group of $Ba_2CuGe_2O_7$. High resolution X-ray diffraction measurements show the excellent quality of crystal samples. FWHM of rocking curve on (0,0,2) reflection proves the high crystallinity, indeed the values listed in Table 3.8 are similar of those reported for systems with a crystal structure less complex and used as commercial substrates [104, 105]. Fig. 3.21 shows rocking curve acquired on Ni0.08 sample, compared with rocking curve acquired on a single crystal of $Ba_2CuGe_2O_7$. Also in this case, X-ray diffraction measurement confirms the excellent quality of the crystal. The slight shift of curves along ω confirms slight structural distortion (distortion of crystalline axes) from $Ba_2CuGe_2O_7$ to $Ba_2Cu_{(1-x)}Ni_xGe_2O_7$.

Moreover, also pole figures prove the presence of a single grain in volume interaction examined by X diffraction. Fig. 3.22 reports a polar figure acquired on sample Ni0.06. To perform the pole figure measurements, the sample is tilted in Ψ and rotated in Φ. The data are collected by using the (0,0,2) reflection obtained at a fixed value $2\theta = 32.87°$.

After careful mechanical polishing, the same crystals oriented by Laue technique and other samples cleaved, are also inspected by electron back scattered diffraction technique. This measurement confirms the absence of any misorientation on a microscopic scale.

Sample	$a = b(\mathring{A})$	$c(\mathring{A})$	χ^2	GOF
Ni0.05	8.4629(5)	5.4480(2)	1.80	1.5
Ni0.06	8.4607(3)	5.4483(9)	1.85	1.5
Ni0.08	8.4597(1)	5.4488(7)	1.80	1.7
Ni0.1a	8.4572(5)	5.4517(8)	2.50	1.8
Ni0.2	8.4547(7)	5.4570(5)	2.00	1.5
Ni0.3	8.4498(1)	5.4580(0)	1.80	1.5

Table 3.5: XRD refinement data of $Ba_2Cu_{(1-x)}Ni_xGe_2O_7$ samples.

Composition	EDS results
$x=0.05$	$Ba_{2.0\pm0.3}Cu_{0.95\pm0.2}Ni_{0.04\pm0.02}Ge_{1.9\pm0.5}O_{7.2\pm0.4}$
$x=0.06$	$Ba_{1.9\pm0.4}Cu_{0.95\pm0.2}Ni_{0.06\pm0.04}Ge_{2.0\pm0.6}O_{6.3\pm0.7}$
$x=0.08$	$Ba_{2.1\pm0.5}Cu_{0.91\pm0.3}Ni_{0.09\pm0.03}Ge_{1.9\pm0.4}O_{6.9\pm0.4}$
$x=0.10$	$Ba_{1.8\pm0.6}Cu_{0.90\pm0.3}Ni_{0.10\pm0.04}Ge_{2.0\pm0.7}O_{6.4\pm0.7}$
$x=0.20$	$Ba_{2.2\pm0.2}Cu_{0.78\pm0.3}Ni_{0.19\pm0.12}Ge_{1.9\pm0.2}O_{7.2\pm0.4}$
$x=0.30$	$Ba_{2.0\pm0.7}Cu_{0.67\pm0.4}Ni_{0.28\pm0.14}Ge_{1.8\pm0.2}O_{7.1\pm0.4}$

**Table 3.6:** Compositional results obtained by EDS analysis

Composition	WDS results
$x=0.05$	$Ba_{2.00\pm0.3}Cu_{0.96\pm0.02}Ni_{0.05\pm0.02}Ge_{2.02\pm0.03}O_{7.2\pm0.1}$
$x=0.06$	$Ba_{2.00\pm0.4}Cu_{0.95\pm0.1}Ni_{0.05\pm0.04}Ge_{2.03\pm0.02}O_{7.3\pm0.2}$
$x=0.08$	$Ba_{2.00\pm0.3}Cu_{0.92\pm0.3}Ni_{0.09\pm0.03}Ge_{2.02\pm0.03}O_{6.9\pm0.1}$
$x=0.10$	$Ba_{2.00\pm0.2}Cu_{0.91\pm0.3}Ni_{0.10\pm0.04}Ge_{2.04\pm0.03}O_{6.8\pm0.2}$
$x=0.20$	$Ba_{2.00\pm0.2}Cu_{0.80\pm0.3}Ni_{0.19\pm0.02}Ge_{2.04\pm0.02}O_{7.2\pm0.2}$
$x=0.30$	$Ba_{2.00\pm0.2}Cu_{0.79\pm0.4}Ni_{0.32\pm0.04}Ge_{2.01\pm0.04}O_{7.1\pm0.1}$

Table 3.7: Compositional results obtained by WDS analysis, normalizing WDS data to the stoichiometric value of Ba= 2

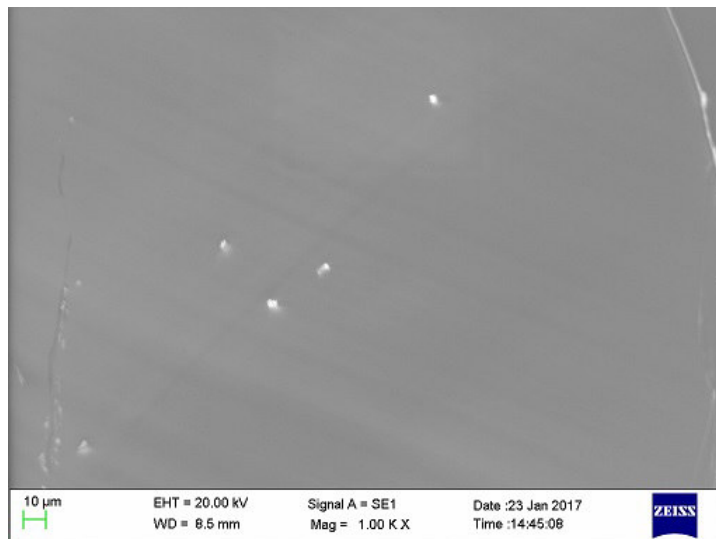| Sample	FWHM($°$)
Ni0.05	0.0121(8)
Ni0.06	0.0135(1)
Ni0.08	0.015(2)
Ni0.1a	0.0112(9)

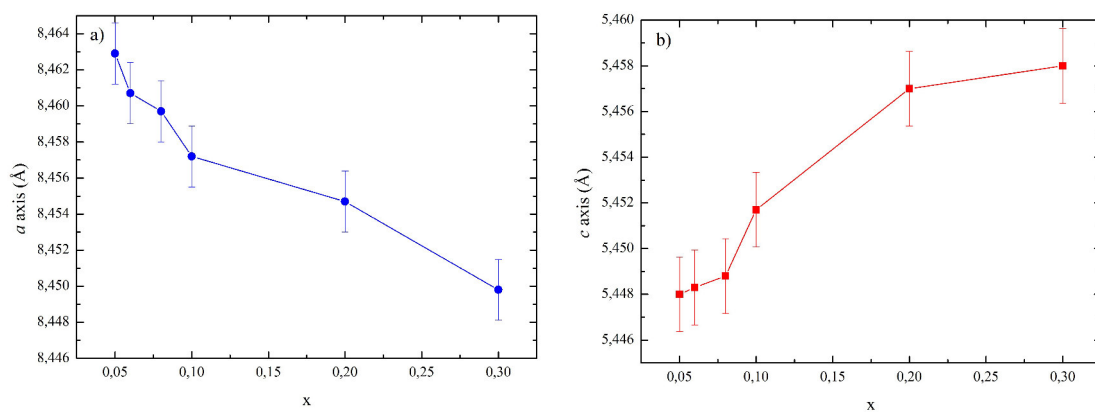**Table 3.8:** FWHM data of $Ba_2Cu_{(1-x)}Ni_xGe_2O_7$ samples of (0,0,2).
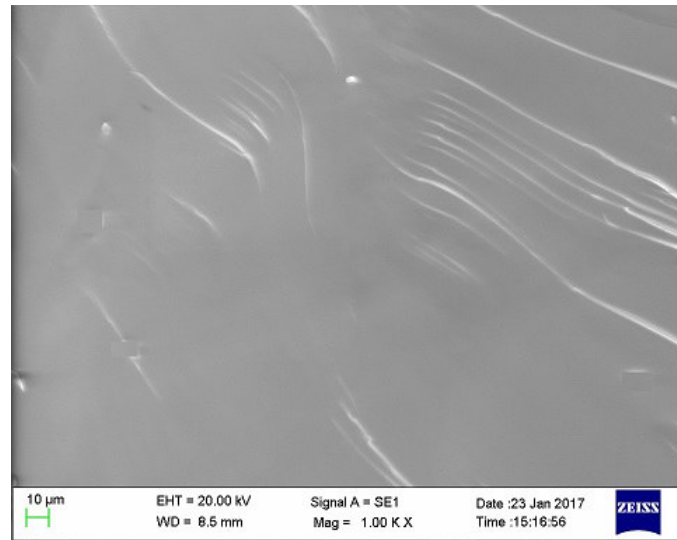
**Figure 3.17:** Sem image of cleaved surface of sample Ni0.3 with magnification 1kX

Figure 3.18: Sem image of cleaved surface of sample Ni0.3 with magnification 1kX

Figure 3.19: Evolution of the cell parameters of $Ba_2Cu_{(1-x)}Ni_xGe_2O_7$ compounds as a function of substituted Ni content(x). Changes of (a) a-axis and (b) c-axis with doping.
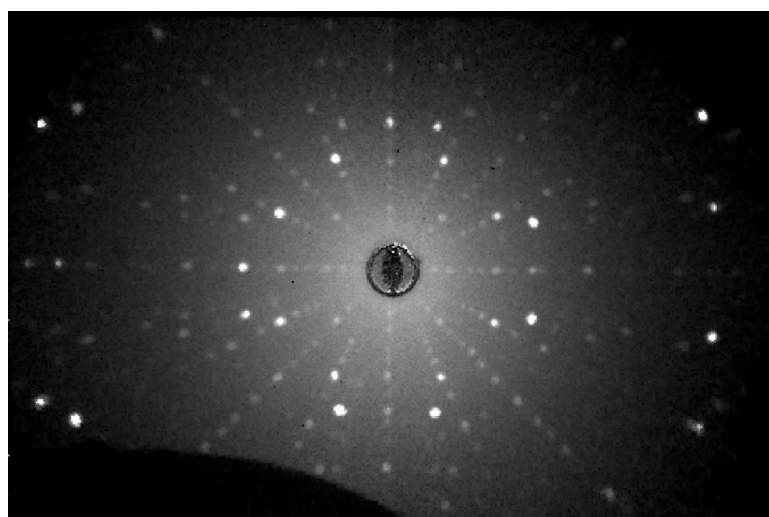
Figure 3.20: X-ray Laue patterns of Ni0.06 crystals oriented with the [001] direction orthogonal to the exposed surface.
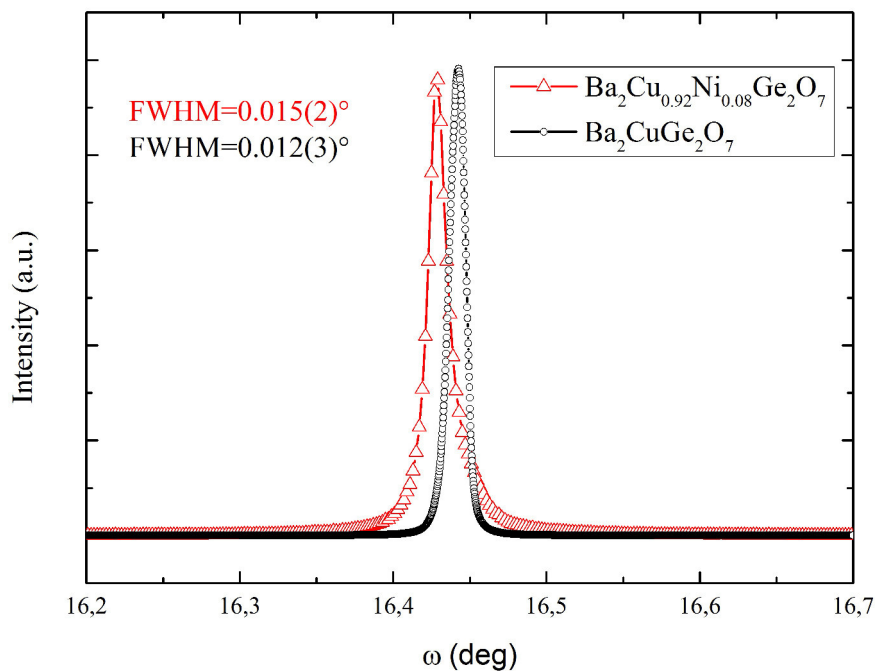
Figure 3.21: Rocking curve of the (002) reflection acquired on a $Ba_2CuGe_2O_7$ (black) single crystal (batch No.10) and on a $Ba_2Cu_{0.92}Ni_{0.08}Ge_2O_7$ (red) single crystal (Ni0.08).
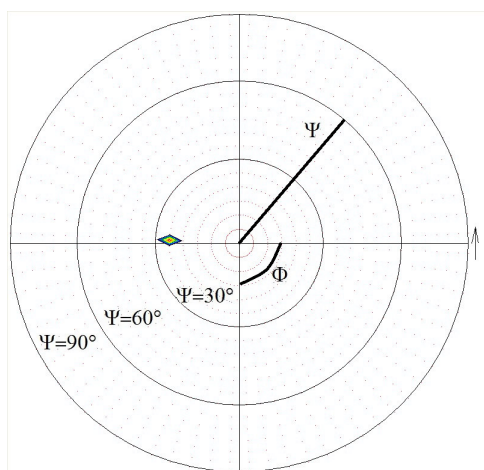
Figure 3.22: Polar figure taken by high resolution X-Ray diffraction on reflection (002) of crystal sample Ni0.06.

3.3.3 $Cu_3Nb_2O_8$

As mentioned in Section 2.4.2, single crystals of helimagnetic $Cu_3Nb_2O_8$ are grown by floating zone technique (Table 2.5). A careful study of the morphology, chemical composition and the crystal structure is carried out by the techniques illustrated above.

Optical microscopy inspection of batches No.1 and No.2 reveals the presence of small dark crystals with dimensions of about 2mm in length and 1×1 mm^2 in cross section. The cleaved pieces are extracted by a sort of polycrystalline matrix.

For batches No.3 and No.4 bigger crystals are isolated with size of about 5mm in length and 1×1 mm^2 in cross section. Cleaving surface is thin, shiny, and smooth.

The single crystals realized by an image furnace with two mirrors (batches No.5 and No.6) show the same morphological features of the samples realized by an image furnace with four mirrors.

Crushed crystals from each batch are analysed by X-ray powder diffraction and the patterns are processed by Rietveld refinement. The results are discussed below to compare the quality of samples. In XRD pattern all peaks are indexed with $Cu_3Nb_2O_8$ phase and no spurious phase is detected, this result underlines the high purity of crystals. Starting from crystal structure reported in literature [10], data are analysed by Rietveld refinement using triclinic symmetry of space group P -1. Qualitatively, refined spectra from $Cu_3Nb_2O_8$ crystals are similar and the blue curves of difference are flat in all cases. Below, we consider a crystal sample from the batch No. 4 (grown in a furnace with four mirrors and called CNO_4M) and one from batch No. 6 (grown in a furnace with two mirrors and called CNO_2M). Rietveld refinement performed on a X-ray pattern acquired on CNO_4M is shown in Fig. 3.23a) while Fig. 3.23b) shows Rietveld refinement performed on a pattern of CNO_2M. There are only slight differences between I_{obs} - I_{calc} curves of Rietveld profiles. Indeed, such curve for CNO_4M is flatter than curve of CNO_2M. Probably, this detail is related to quality of single crystal sample, which results slightly better in the first case. This slight difference is confirmed by χ^2 of fit, (Tab. 3.9), indeed this value is higher for CNO_2M.

Quantitative results, listed in Table 3.9, clearly show that the refined parameters are in agreement with those ones reported into literature [10]. EDS analysis is performed on many areas of all samples and their compositions are very close to the nominal one. The average is $Cu_{3.1\pm0.1}Nb_{2.0\pm0.1}O_{8.2\pm0.1}$. No different elements from those expected are detected, confirming the high quality of the obtained compounds.

EBSD analysis is performed on many cleaved surfaces. $Cu_3Nb_2O_8$ crystal

Sample	$a(\mathring{A})$	$b(\mathring{A})$	$c(\mathring{A})$	α	β	γ	χ^2
CNO_4M	5.1815(4)	5.4871(5)	6.0096(4)	72.5762(2)	83.4261(5)	65.7086(5)	1.8
CNO_2M	5.1785(4)	5.4801(5)	6.0074(7)	72.5790(9)	83.4222(3)	65.7091(2)	2.1

Table 3.9: XRD refinement data of $Cu_3Nb_2O_8$. CNO_4M is a sample realized by a furnace with 4 mirrors, while CNO_2M by a furnace with 2 mirrors .

cleaves without a natural favourite crystallographic direction.

An example of EBSD pattern is reported in Fig. 3.24. Pattern is acquired on a single crystal from batch No.5. EBSD pattern shows bright Kikuchi bands and a good contrast against background, thus single crystal shows a high crystallinity.

From processing of this pattern by software, the orientation maps are elaborated together to pole figure (Fig. 3.25). In the example, the single crystal has only c axis on surface plane with inclination of $\alpha = 25°$ to rolling direction RD. Moreover, phase map shows only $Cu_3Nb_2O_8$ phase along all surface.

Results discussed below show that $Cu_3Nb_2O_8$ crystal grows without a natural favourite crystallographic direction.

Crystal batches of $Cu_3Nb_2O_8$ (No.3, No.4, No.5) are cut through a diamond saw perpendicularly to the direction of growth. These slices are finely polished with polycrystalline diamond suspension down to 0.3 μm in grain size. EBSD analysis is performed also on these crystalline slices. Normal direction ND (detected with EBSD) corresponds to the crystal growth direction. ND orientation map shows a different colour in each slice, therefore we conclude that the $Cu_3Nb_2O_8$ grows with a random crystallographic direction.

Three samples of few mm^3 from batch crystal No.3 are oriented using the X-ray Laue technique. The first sample is oriented with a-axis normally to the surface of sample. Similarly, the second one is oriented with b-axis perpendicularly to the plane of sample. Finally, the last crystal is oriented with c-axis orthogonally to surface. These samples are used for an investigation about magnetic behaviour which will be discussed in the next Chapter.
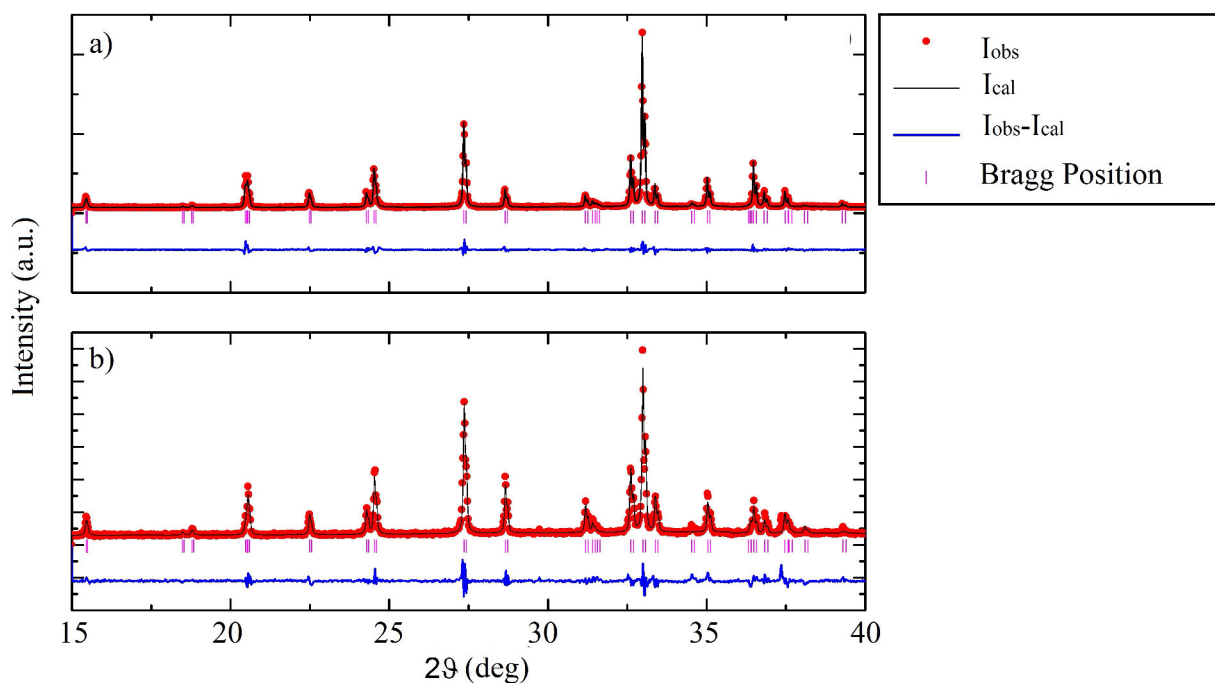
Figure 3.23: Simulated diffraction pattern of $Cu_3Nb_2O_8$ against experimental XRD data. a)Rietveld refinement on CNO_4M, grown by a furnace with 4 mirrors. b)Rietveld refinement on CNO_2M, grown by a furnace with 2 mirrors.
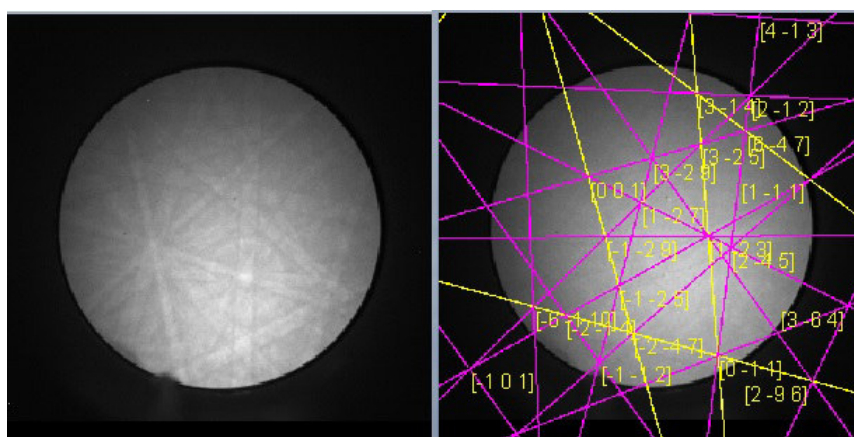
Figure 3.24: EBSD pattern taken on single crystal of $Cu_3Nb_2O_8$ No.3 with indication of crystallographic direction of each Kikuchi band.
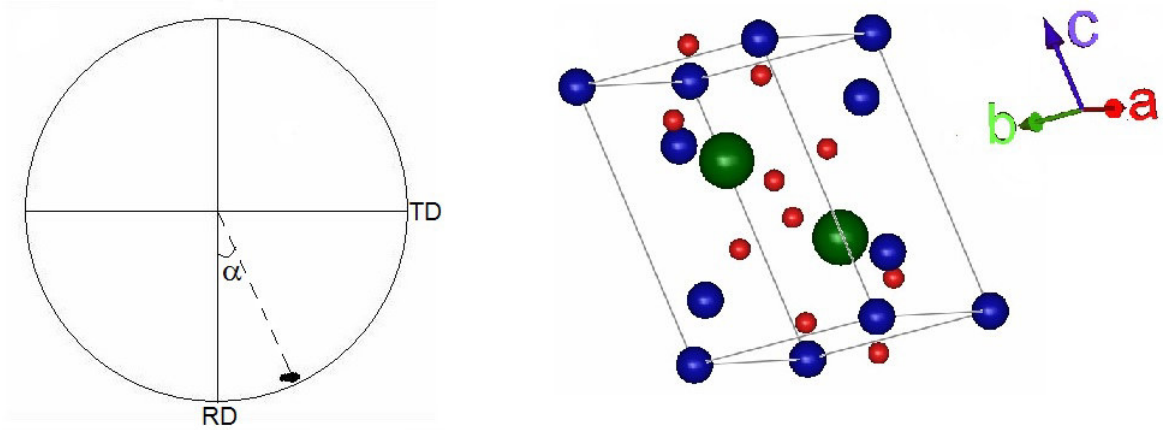
Figure 3.25: (0,0,1) Pole figure and simulation of crystal cell in single crystal.

Chapter 4

Low temperature magnetometry and lattice dynamics of single crystals

In this work, the successful growth of $Ba_2CuGe_2O_7$ and $Cu_3Nb_2O_8$ single crystals is discussed. High quality samples are grown using the floating zone technique, in different gas atmospheres and pressures.

The X-ray Laue back reflection and EBSD techniques are used to orient single crystals specifically for selected crystalline directions.

To study the magnetic phase diagrams of grown crystals, magnetization measurement as function of the temperature (M(T)) is performed in different ranges of temperature. Also, measurement of magnetic dc susceptibility (χ(T)) is discussed below. Moreover, low temperature magnetometry study is performed on oriented single crystal of $Ba_2CuGe_2O_7$. The results show the presence of different magnetic transitions for 0.5K<T<5K.

While magnetoelectric properties of $Ba_2CuGe_2O_7$ have been extensively discussed in past research [18, 9, 107], no investigation is reported on its lattice dynamics. In this Chapter, infrared and Raman phonon spectra of $Ba_2CuGe_2O_7$ are shown.

Finally, last Section shows the reflectivity in the ab plane and along the c axis of a single crystal of $Ba_2CuGe_2O_7$. The resulting optical conductivity $\sigma(\omega)$ is compared with the results of calculations of its electronic band structure based on Density Functional Theory (DFT).

4.1 Experimental procedures

4.1.1 Magnetic measurements

In this work, magnetic magnetization of $Ba_2CuGe_2O_7$ crystal is measured using a SQuID (Superconducting Quantum Interference Device) magnetometer, part of Quantum Design's Magnetic Property Measurement System (MPMS). The SQuID is an instrument which is very sensitive to magnetic fields, making it ideal for measuring subtle changes in the magnetic behaviour of a sample when it is subjected to different temperatures, magnetic fields or pressures [108].

A zero-field cooled (ZFC) measurement involves the sample being cooled from the high temperature state to base temperature before a magnetic field is applied to the sample, and in a field cooled (FC) measurement the field is applied beforehand. There can be a significant difference between the ZFC and FC data depending on the nature of the magnetic order present in a material.

$Ba_2CuGe_2O_7$ samples of few mm^3 are oriented using the X-ray Laue technique, then they are cut parallel to selected planes and their surfaces are mirror polished.

The magnetization measurements on single crystals of $Ba_2CuGe_2O_7$, in the temperature range 1.5K-300 K, are carried out in a Quantum Design MPMS system at Warwick University. Data are recorded in zero field cooled (ZFC) and field cooled (FC) modes in an applied magnetic field of 0,1 T.

To explore the magnetic phase diagram of $Ba_2CuGe_2O_7$ at low temperature, different magnetic fields in the range 0 to 5 T are applied along the a or c crystallographic axes for 0.5K<T<5K.

Moreover, this work reports the magnetic characterization of $Ba_2Cu_{(1-x)}Ni_xGe_2O_7$ for the first time. Measurements are carried out using a vibrating sample magnetometer (VSM, Oxford Instruments, Maglab 9T, at CNR-Spin-Napoli). The magnetization is measured as a function of temperature in a constant field of 0,1 T with range 2K -120K, using ZFC mode and FC mode.

Finally, this work reports the magnetic characterization of single crystals of helimagnet $Cu_3Nb_2O_8$. Also, these measurements are performed using by using Quantum Design MPMS system at Warwick University. Measurements are performed on main axes a, b and c. Magnetization M in ZFC mode and in FC mode is recorded versus temperature in the range 2K-300K with field H=0.1 T.

4.1.2 Infrared and Raman spectroscopy

Infra-red (IR) and Raman spectroscopy can provide information about the molecular composition, the bonds, the chemical environment, the phase and the crystal structure of the samples.

Fundamentals of these techiniques are discussed below, but a full description of experimental methods is rather complex and it is beyond the aim of this work. However, further details are well illustrated in the references [109, 110]. When light (or a photon) interacts with a molecule, it can either be elastically or inelastically scattered. In the first case, the absorbed photon has the same wavelength with the emitted one (Rayleigh scattering), but in the second case, the photon has lost or gained an amount of energy related to the vibrational energy spacing in the molecule. This amount corresponds to the wavelength of the Stokes and anti-Stokes lines which are equally displaced from the Rayleigh line in the Raman spectrum. Infra-red spectroscopy also measures the vibrational energies of molecules. The absorption of light in the infrared region of the electromagnetic spectrum, gives a spectrum that corresponds to specific vibrational modes and is unique to each molecular structure examined.

The main difference between the two techniques lies in the nature of the molecular transitions taking place. For a transition to be Raman active there must be a change in the polarizability of the molecule during the vibration. This means that the electron cloud of the molecule must undergo positional change. On the other hand, for an IR detectable transition, the molecule must undergo dipole moment change during vibration. So, when a molecule is symmetrical, e.g. O_2, we cannot observe any IR absorption lines, since the molecule cannot change its dipole moment. It has been observed that molecules with a strong dipole moment are typically hard to polarize.

Regarding the excitation wavelength, the Raman technique uses a monochromatic beam or laser, in the visible, near-infrared, or near ultraviolet range of the electromagnetic spectrum. In IR spectroscopy, a monochromatic beam is used in the infrared region of the electromagnetic spectrum. The wavelength here increases or decreases over time, in order to observe all the absorption lines within a specific range of the infrared region.

Another difference can be observed in the resulting spectra. The IR technique shows irregular absorbance (or transmittance) lines, depending on the material investigated. The Raman spectrum mainly comprises the elastic scattered light line (Rayleigh) and two equally distanced lines Stokes and anti-Stokes, with the second being rather weak and difficult to detect.

$Ba_2CuGe_2O_7$ crystals used for IR and Raman measurements show the

largest surface with the a (or b) and the c- axes. This surface is finely polished with polycrystalline diamond suspension down to 0.3 μm in grain size. The dimensions of the crystals employed in this work are approximately $3 \times 2 \times 1$ mm^3.

Measurements of Infra-red and Raman spectra are acquired by Calvani's group at Roma University.

To acquire Infra-red spectra, the reflectivity R(ω) of the surface is measured with a rapid-scanning Michelson interferometer from 7 K to 300 K. Two different polarizations of the radiation field are used, one along the c axis and the other one perpendicular to the c axis (the latter belongs to the ab plane). The Raman spectra are measured with a Horiba LabRAM HR Evolution micro spectrometer in backscattering geometry. Polarization rotators, properly located along the internal optical path, allow us to align the electric field **E** of the incident beam either along the crystalline axis a or along c.

The Raman spectra are detected at temperatures varying from 300 K to 80 K. Raman spectra in the $10 - 1000$ cm^{-1} range are thus collected by a Peltier-cooled charge-coupled device (CCD) detector with a spectral resolution better than 1 cm^{-1}.

4.1.3 Electronic bands and optical conductivity

Ba$_2$CuGe$_2$O$_7$ electronic bands are investigated. Optical spectra are taken at different temperatures from the mid-infrared (MIR) to the visible.

Measurements are acquired by Calvani's group at at Roma University by a Michelson interferometer with a Mercury-Cadmium-Tellerium detector.

The reflectivity is measured in the ab plane and along the c axis of a single crystal of the Ba$_2$CuGe$_2$O$_7$, from 20 to 300 K and from 700 to 24000 cm^{-1}.

4.2 Magnetic measurements

4.2.1 Ba$_2$CuGe$_2$O$_7$

Ba$_2$CuGe$_2$O$_7$ crystal samples grown by floating zone technique are listed in Table (2.3).

Magnetization measurements carried out from room temperature down to 1.5K on single crystals (batch No.6) in zero field cooled and field cooled conditions, in a magnetic field of 0.1 T are shown in Fig. 4.1.

These show paramagnetic behaviour of Ba$_2$CuGe$_2$O$_7$ samples at room temperature as reported in literature [111]. Moreover, two separate features are

visible in the inset of Fig. 4.1 a broad peak below T=10K, centred at T=8.5 K, and a cusp like minimum at $T_N = 3.3$ K.

The broad peak is related to short range antiferromagnetic 2D correlations in the basal (a,b) plane [9], while the increase in the magnetization at low temperature is due to the long-range helimagnetic ordering occurring at T_N. The observed magnetization in our crystal is consistent with the phase diagram of $Ba_2CuGe_2O_7$ outlined recently by neutron diffraction study [18, 107, 111]. It is worth mentioning that the same magnetic behaviour is observed for the dark yellow crystals (batches No. 7 and 8). The same magnetic behaviour is observed in the transparent crystals obtained from batches No 9 to 13 and the dark yellow crystals obtained from batches No.7 and 8, confirming that the different colour of the crystals does not affect their magnetic behaviour.

To explore the magnetic phase diagram of $Ba_2CuGe_2O_7$, different magnetic fields in the range 0 to 5 T are applied along the a or c crystallographic axes. The temperature range is from 0.5 K to 5 K.

A selection of representative magnetometry data is reported in Fig. 4.2. The data sets referring to fields applied along the two different directions show a qualitatively similar behaviour. However, the transition related to helimagnetic transition at $T_N = 3.3$ K is more evident for H parallel to b [Fig. 4.2(a)], where a cusp like feature signals the para- to quasi-AF magnetic phase transition. When magnetic field is applied along c-axis, the same transition is observed mostly as a change in the curvature of magnetometry data (flection point). The magnetism of $Ba_2CuGe_2O_7$ is clearly sensitive even to low applied fields. Indeed, as shown in Fig. 4.2(a), below $T_N = 3.3$ K there is a drastic change in the system's magnetic response at ca. H=0.01T: for fields below this threshold (including zero fields) the system behaviour is dominated by internal magnetic interactions.

For intermediate applied fields, and independent of their orientation [see Fig. 4.2(a), (b)], the magnetic susceptibility displays a field dependent minimum, whose value shifts monotonously to higher temperatures as the field value increases. In this regime, the magnetic Cu^{2+} ions become progressively less coupled among themselves and respond increasingly to the externally applied field. Finally, besides the known magnetic phase boundary at $T_N = 3.3$ K, the low-temperature data hint at a new transition at 0.6 K [left arrow and inset in Fig. 4.2(a)]. This second transition, characterized by a bump (or by susceptibility oscillations) in the proximity of the critical zone, is clearly seen in the magnetometry data. In the low-applied-field regime, the features at 0.6 K are made more prominent by plotting the derivative of the susceptibility, $\frac{d\chi}{dT}$, as shown in the inset of Fig. 4.2(a) for two typical cases.

By systematically plotting the field-dependent minima (maxima) for the

transition at 3.2 K (0.6 K), the low-temperature magnetic phase diagram of $Ba_2CuGe_2O_7$ is reconstructed. The results, shown in Fig. 4.3, clearly indicate the presence of three different magnetic phases.
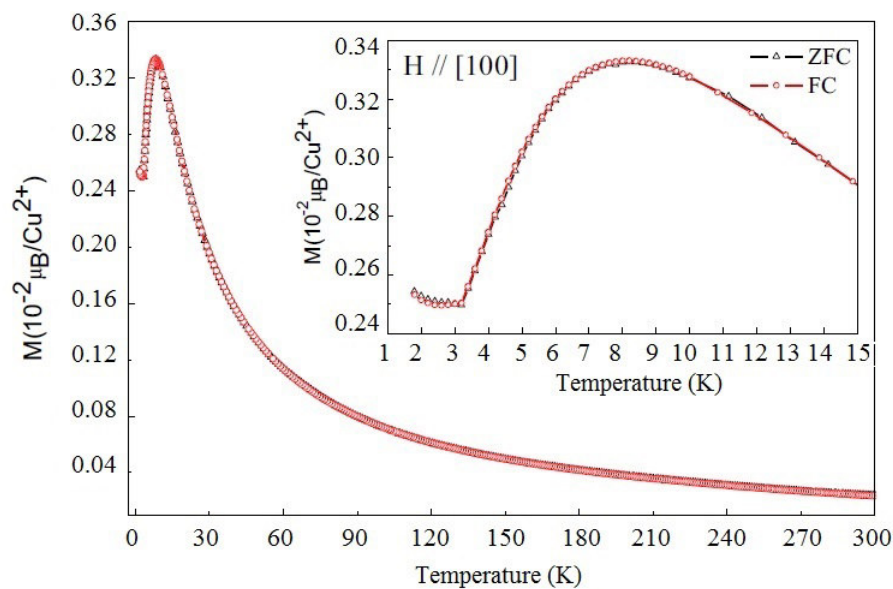
Figure 4.1: Magnetization versus temperature of $Ba_2CuGe_2O_7$ single crystal (batch No.6) for a field H=0.1T applied parallel to the [100] axis. Inset: en largement of low temperature magnetic behaviour.
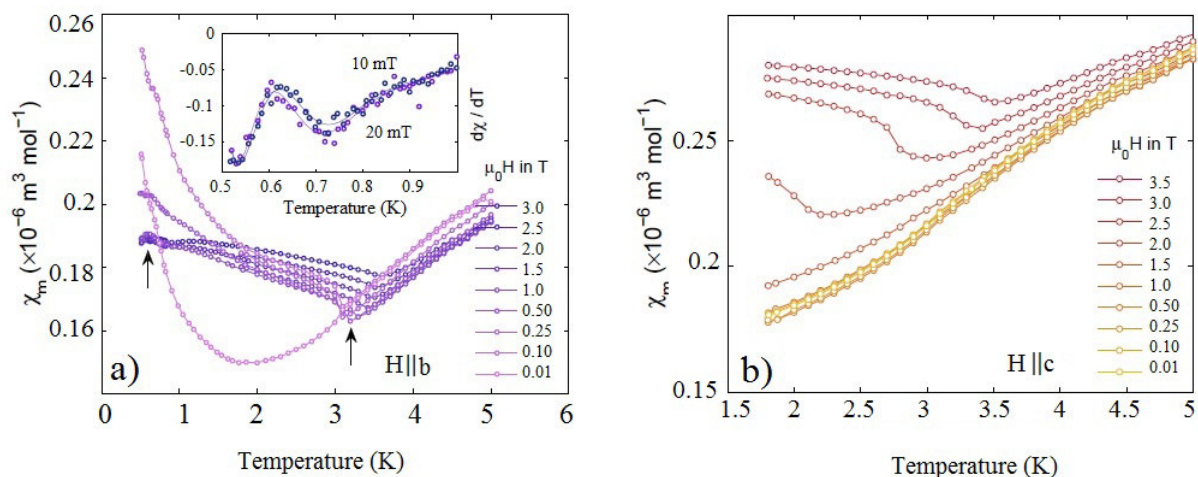
Figure 4.2: Magnetic susceptibility vs. temperature for $Ba_2CuGe_2O_7$ for different applied fields along the b axis (left) or along the c axis (right). Both data sets show a qualitatively similar behavior and hint at a complex magnetic phase diagram, with a (field-dependent) transition at 3.2 K. Measurements with H$\parallel b$, extending down to 0.5 K, indicate an additional phase transition at 0.6 K (see inset). The positions of both transitions are marked by arrows in panel (a).
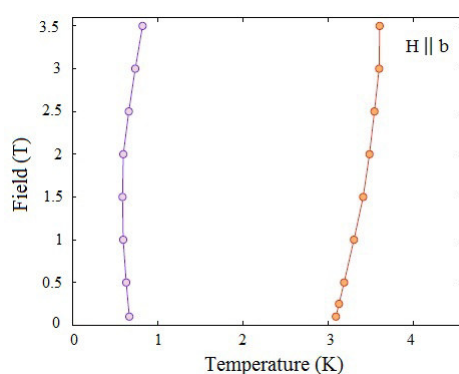
Figure 4.3: Magnetic (H, T) phase diagram of $Ba_2CuGe_2O_7$, as deduced from magnetometry measurements for H$\parallel b$. The two phase boundaries at ca. 0.6 and 3.2 K divide the (H, T) plane into three areas: a magnetically ordered phase (left), a yet unknown phase (center), and a paramagnetic phase (right).

4.2.2 $Ba_2Cu_{(1-x)}Ni_xGe_2O_7$

The magnetization is measured using the SQuID magnetometer between temperatures of 2K and 120K for polycrystalline and single crystals samples of $Ba_2Cu_{(1-x)}Ni_xGe_2O_7$ with changing x.
The resulting curves are shown in Figure 4.4. These curves show the behaviour of magnetization versus temperature for polycrystalline samples with composition $Ba_2Cu_{0.95}Ni_{0.05}Ge_2O_7$, $Ba_2Cu_{0.7}Ni_{0.3}Ge_2O_7$ and $Ba_2Cu_{0.5}Ni_{0.5}Ge_2O_7$.
The curve of compound with lower Ni doping ($Ba_2Cu_{0.95}Ni_{0.05}Ge_2O_7$) is very similar to that one of parent compound $Ba_2CuGe_2O_7$. At about T=7K, M(T) shows a rather broad peak.
Magnetization of $Ba_2Cu_{0.7}Ni_{0.3}Ge_2O_7$ shows a very different trend. First, the magnetization is stronger. Second, at the lower temperature the trend of compound decreases monotonically with a local minimum at T=3K. The trend doesn't show the broad peak of $Ba_2Cu_{0.95}Ni_{0.05}Ge_2O_7$ at T=7K. Qualitatively, magnetization of $Ba_2Cu_{0.7}Ni_{0.3}Ge_2O_7$ indicates a paramagnetic behaviour.
Similar considerations are valid for magnetization of $Ba_2Cu_{0.5}Ni_{0.5}Ge_2O_7$.
A brief explanation of the similar trend of magnetization of $Ba_2Cu_{0.5}Ni_{0.5}Ge_2O_7$ and $Ba_2Cu_{0.7}Ni_{0.3}Ge_2O_7$ is discussed below.
As discussed in Section 3.2.2, compositional study of solid solution of $Ba_2Cu_{(1-x)}Ni_xGe_2O_7$ shows that x=0.3 is the solubility limit, thus $Ba_2Cu_{0.7}Ni_{0.3}Ge_2O_7$ and $Ba_2Cu_{0.5}Ni_{0.5}Ge_2O_7$ are different stoichiometric compositions of solid solution apparently. Indeed, polycrystalline powder of $Ba_2Cu_{0.5}Ni_{0.5}Ge_2O_7$ and of $Ba_2Cu_{0.7}Ni_{0.3}Ge_2O_7$ contain the same composition of $Ba_2Cu_{(1-x)}Ni_xGe_2O_7$ (with limit solubility x=0.3), but $Ba_2Cu_{0.5}Ni_{0.5}Ge_2O_7$ contains higher additional spurious phases. Such spurious phases are $Ba_3Ge_3O_9$ and NiO, which do not affect magnetic behaviour. Thus, $Ba_2Cu_{0.5}Ni_{0.5}Ge_2O_7$ and $Ba_2Cu_{0.7}Ni_{0.3}Ge_2O_7$ show the same magnetic behaviour of $Ba_2Cu_{(1-x)}Ni_xGe_2O_7$ with x=0.3.

Since these investigations show that $Ba_2Cu_{(1-x)}Ni_xGe_2O_7$ changes its magnetic properties for lower doping, additional magnetic study is performed on single crystals of $Ba_2Cu_{(1-x)}Ni_xGe_2O_7$ with low x.
$Ba_2Cu_{0.95}Ni_{0.05}Ge_2O_7$ and $Ba_2Cu_{0.92}Ni_{0.08}Ge_2O_7$ samples are oriented using the X-ray Laue technique, then they are cut parallel to (0,0,1) or (0,1,0) planes and their surfaces are mirror polished.
Figure 4.5 shows the magnetization versus temperature measurements for a magnetic field H=0.1 T applied parallel to the a-axis acquired on single crystals of $Ba_2CuGe_2O_7$, $Ba_2Cu_{0.95}Ni_{0.05}Ge_2O_7$ and $Ba_2Cu_{0.92}Ni_{0.08}Ge_2O_7$.
They show paramagnetic behaviour of all samples at room temperature. For $Ba_2Cu_{0.95}Ni_{0.05}Ge_2O_7$ two features are visible, a broad peak below T=10K and a minimum at $T_N = 3.3$ K. The inset of Figure 4.5 shows that this

minimum is not similar to a cusp point, unlike the minimum of $Ba_2CuGe_2O_7$ magnetization.

Also $Ba_2Cu_{0.92}Ni_{0.08}Ge_2O_7$ shows a magnetization vs temperature with a minimum at $T_N = 3.3$ K, but with greater intensity.

Such magnetic investigations indicate that substitution of Nickel on Copper site induces considerable effects on magnetic and structural properties. They are a crucial step to further studies as for example neutron diffraction on single crystal samples to study the magnetism of this system.
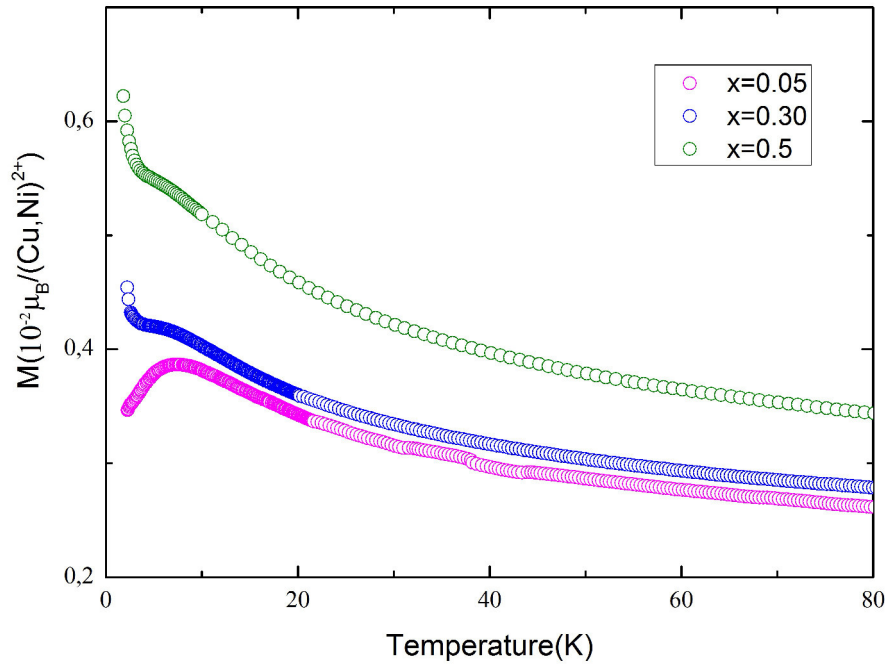
Figure 4.4: Magnetization versus temperature of $Ba_2Cu_{(1-x)}Ni_xGe_2O_7$ polycristalline powder applying a magnetic field H=0.1 T.
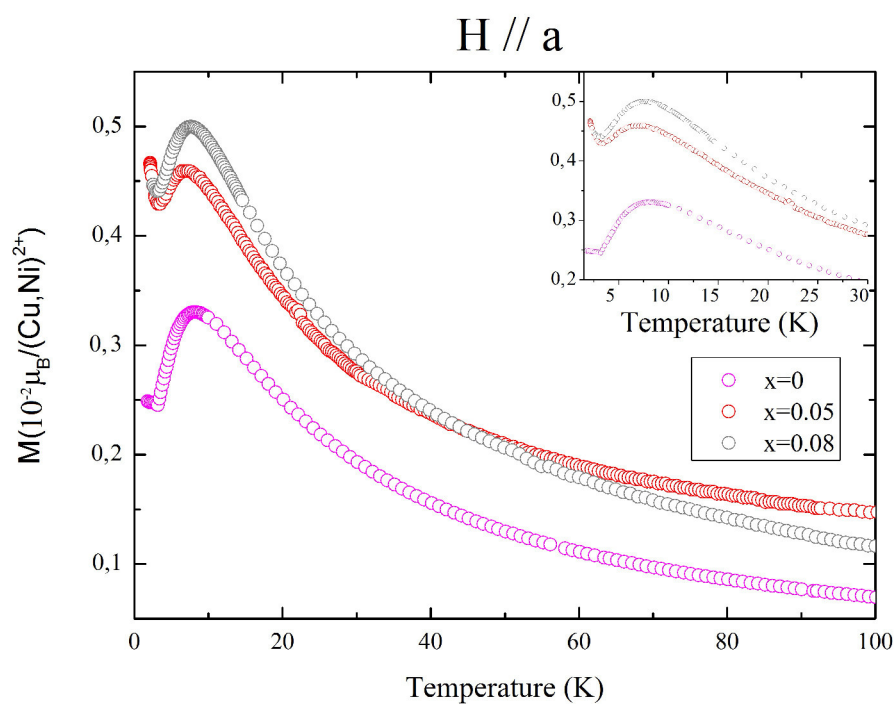
Figure 4.5: Magnetization versus temperature of $Ba_2Cu_{(1-x)}Ni_xGe_2O_7$ single crystal applying a magnetic field H=0.1T applied parallel to the a-axis. Inset: enlargement of low temperature region.

4.2.3 $Cu_3Nb_2O_8$

At present, the only magnetization data for $Cu_3Nb_2O_8$ in the literature consist of measurements on polycrystalline samples [90], and on single crystal data [10].

The following magnetization data are measured along the a-, b- and c-axes of $Cu_3Nb_2O_8$.

The resulting curves are shown in Figure 4.6. The magnetic properties in $Cu_3Nb_2O_8$ are anisotropic, with the magnitude and temperature dependence of the magnetization being significantly different along each axis.

At high temperature, the magnetizations M_a, M_b, and M_c show a broad peak centered at about 40K, confirming results reported in literature [10]. Such feature is explained by short-range magnetic correlations and is observed in others similar complex magnetic materials as $Ba_2CuGe_2O_7$.

M_b is significantly lower than M_a and M_c, this result is consistent with the crystal structure of compound. Indeed, along b axis, Cu-O chains are separated by the non-magnetic Nb atoms so the value of magnetization is lower.

At $T_N = 26.5$ K (inset of Fig. 4.6) an anomaly is showed in the curves in all crystalline directions. It indicates an antiferromagnetic transition as confirmed by measurement of specific heat [10], which shows an anomaly at the same temperature.

Moreover, dM/dT show a peak at $T_2 \sim 25$K (Fig.4.7). These divergences match to cusps in specific heat plot and with a ferroelectric transition reported in literature [10, 90].

For all orientations, above 50 K the susceptibilities $\chi = \frac{M}{H}$ follow Curie-Weiss law $\chi = \frac{C}{T+\theta_W}$. Results of fit are listed in Table 4.1. Value of estimated Weiss temperatures are slightly lower than previous reports, very probably this difference may be explained by the fact that our measurements are performed on an aligned crystal, along well-defined crystallographic axes, while the previous results are obtained from randomly oriented polycrystals.

Synthesis of large single crystals allows us to investigate the fundamental physics of this material in order to identify the mechanisms responsible for its peculiar helimagnetic properties.
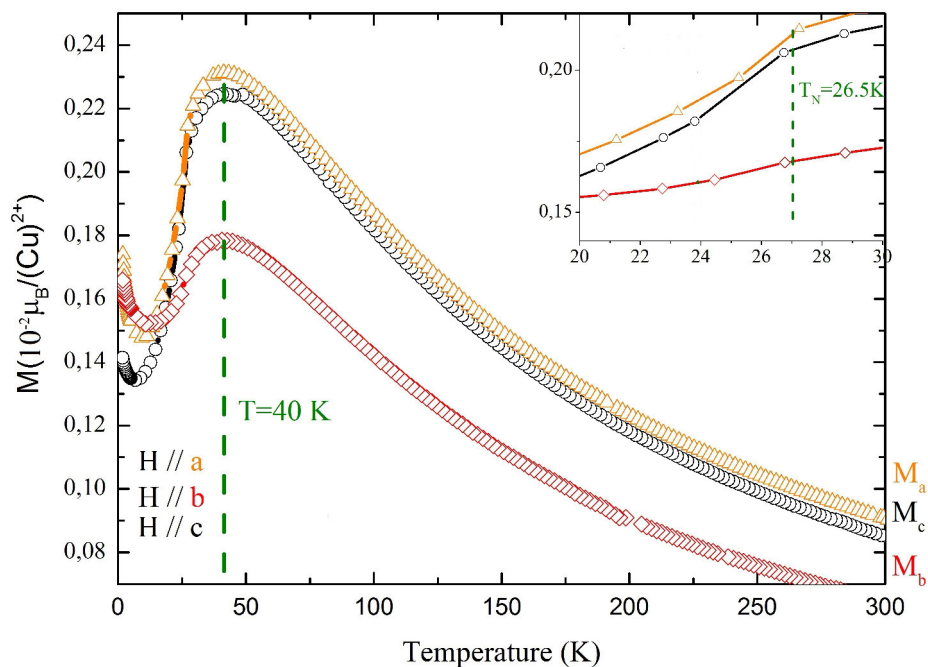
Figure 4.6: a)Temperature dependence of magnetization of $Cu_3Nb_2O_8$ single crystal with field applied parallel to different crystallographic axes.
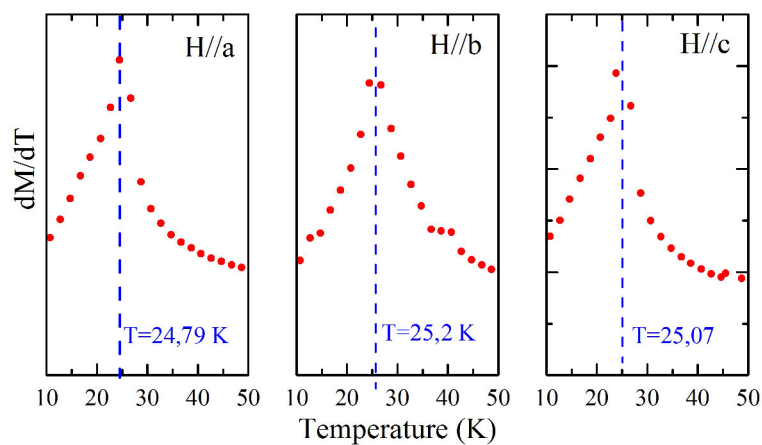
Figure 4.7: Divergences in the derivative dM/dT along different crystallographic axes of $Cu_3Nb_2O_8$.

	θ_W (K)	C (emu K/mole^{-1}Oe^{-1})
H$\parallel a$	-153,07 $\pm$ 0,02	2,42 $\pm$ 0,03
H$\parallel b$	-121,66 $\pm$ 0,02	1,60 $\pm$ 0,03
H$\parallel c$	-147,37 $\pm$ 0,02	2,3 $\pm$ 0,03

Table 4.1: Weiss temperature and Weiss constant values obtained for the fit of χ^{-1} versus T data collected on $Cu_3Nb_2O_8$ single crystals with H=0.1 T.

4.3 Infrared and Raman spectra of helimagnet Ba$_2$CuGe$_2$O$_7$

The lattice dynamics of helimagnet Ba$_2$CuGe$_2$O$_7$ is studied by measuring the infrared reflectivity of a single crystal with the radiation polarized both in the ab plane and along the c axis of its tetragonal cell, from 7 K to 300 K [112]. The raw reflectivity data of Ba$_2$CuGe$_2$O$_7$ are shown in Fig. 4.8. No interesting effects are shown by the spectra at intermediate temperatures. Both spectra look very similar to the corresponding reflectivity spectra of Ba$_2$CoGe$_2$O$_7$, as reported in the same frequency range [103].

The optical conductivity extracted from the data of Fig. 4.8 is shown in Fig. 4.9 in the far infrared region, both at the lowest and highest measured temperatures. Fourteen transverse optical (TO) phonon modes are detected with the radiation polarized in the ab plane, out of the eighteen E modes predicted by a factor-group analysis of the P-42$_1$m unit cell, and all the ten B$_2$ modes predicted along the c axis. The absence of line frequencies common to both polarizations confirms that the polarizer is correctly oriented and that the sample is a single crystal.

In order to understand the complex phonon spectrum of Ba$_2$CuGe$_2$O$_7$, a shell model (SM) is used which enabled us to perform lattice dynamical calculations and to compare the results with the measured $\sigma_1(\omega)$. The theoretical frequencies $\Omega_j(th)$ of the transverse optical (TO) infrared phonons obtained with the model are calculated for the ab plane and for the c axis. There is a good agreement, within the experimental linewidths, between the observations and the theoretical predictions, as far as the phonon frequencies are concerned [112].

Only few modes are systematically higher than the theoretical values. The discrepancy may be due either to anharmonic effects, not taken into account in the model, or to an overestimation of the shell-shell repulsive interactions. The number of the observed phonon lines is lower (for the ab plane) or equal (for the c axis) to that predicted for Ba$_2$CuGe$_2$O when cooling the sample to 7 K. Therefore, spectra confirm that the tetragonal symmetry is conserved down to the lowest temperatures, with no appreciable orthorhombic distortion.

The work [113] is aimed at completing the description of the lattice dynamics in Ba$_2$CuGe$_2$O$_7$ by presenting its Raman phonon spectrum.

The Raman spectrum is detected at temperatures varying from 300 to 80 K in a single crystal, with the radiation polarized either in the ab plane or along the c axis of its tetragonal cell.

The results of Raman scattering in Ba$_2$CuGe$_2$O$_7$ are shown in Fig. 4.10 a)-b) for the radiation polarized along the a axis and in Fig. 4.10 c)-d)
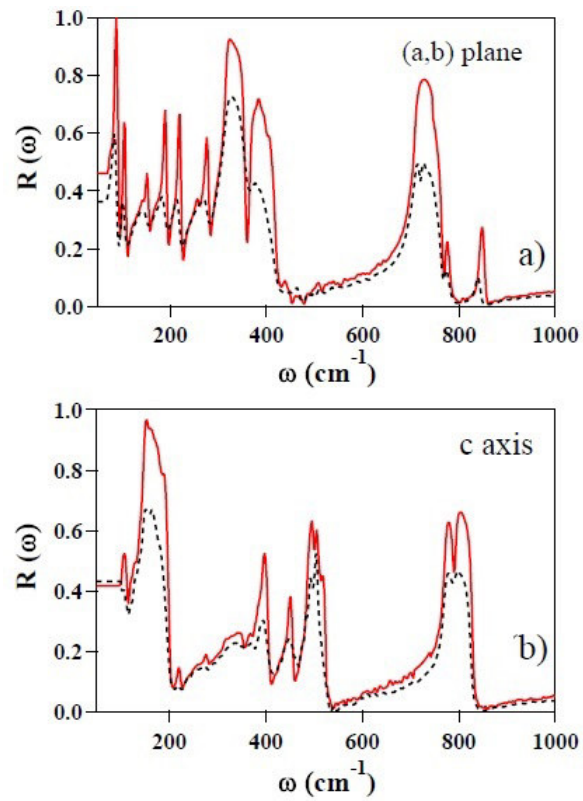
Figure 4.8: Reflectivity of $Ba_2CuGe_2O_7$, in the far-infrared range of frequencies at 7 K (solid line) and 300 K (dashed line), with the radiation polarized in the ab plane (a) and along the c axis (b).
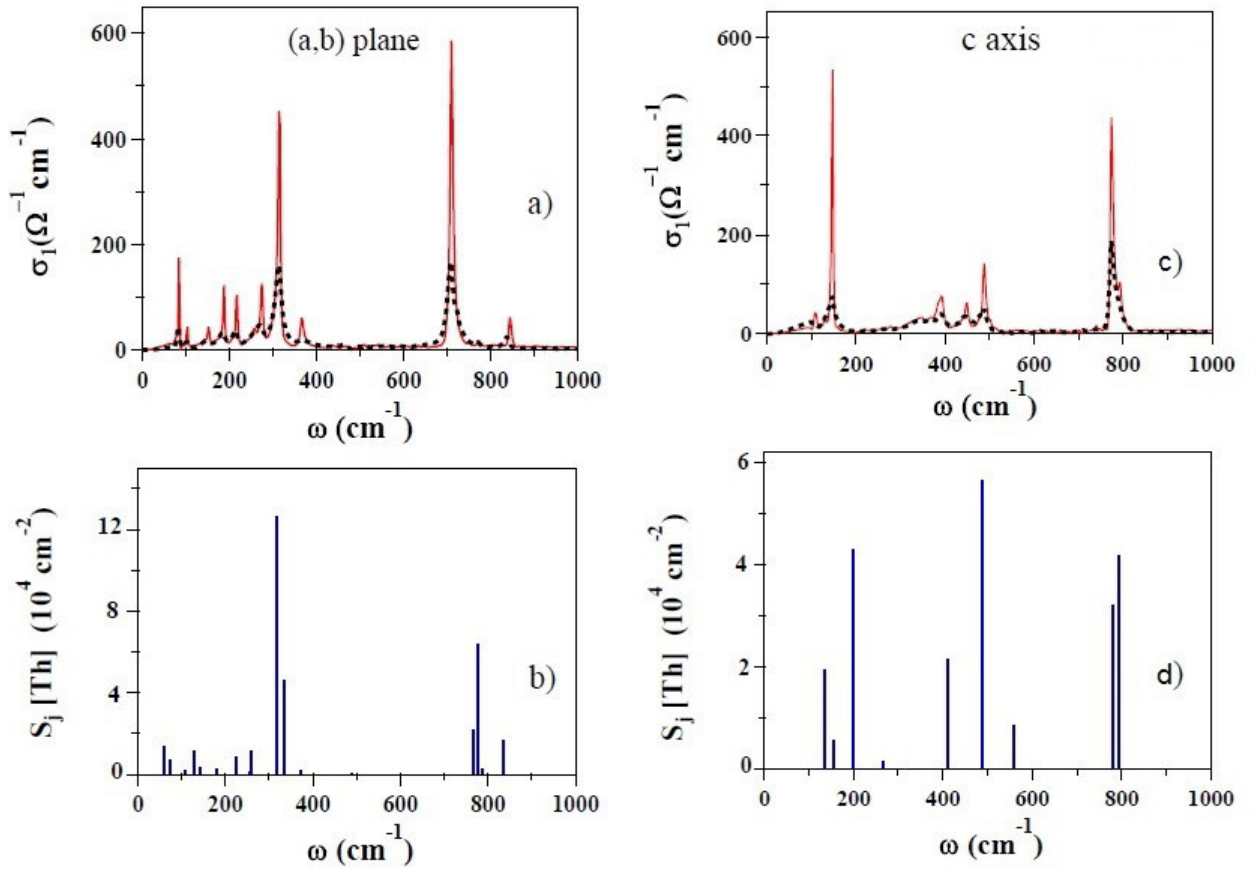
Figure 4.9: a) Optical conductivity of $Ba_2CuGe_2O_7$, in the far infrared range of frequencies at 7 K (solid line) and 300 K (dashed line), with the radiation polarized in the *ab* plane. b) Shell-model results for the vibrational modes of the *ab* plane. c) Optical conductivity of $Ba_2CuGe_2O_7$, in the far infrared range of frequencies at 7 K (solid line) and 300 K (dashed line), with the radiation polarized in *c* axis. d) Shell-model results for the vibrational modes of the *c* axis.

for the electric field along the c axis. Only spectra taken at 80 and 300 K are reported, as no major effects are found to affect the phonon lines at intermediate temperatures. 29 Raman lines are observed which, once combined with our previous infrared observations, provide the frequencies, widths, and relative intensities at different temperatures of 40 phonon modes out of the 45 predicted by group theory for this crystal. In Fig. 4.10, at 80 K, 24 lines are detected with **E** along a (two of which are extracted from a couple of asymmetric lines by fitting to the data a sum of Lorentzians), while 17 lines are observed with **E** along the c axis in Fig. 4.10.

Among the latter ones, however, only five are not replicas of those of the ab plane.

These results provide an exhaustive description of the lattice dynamics in $Ba_2CuGe_2O_7$.
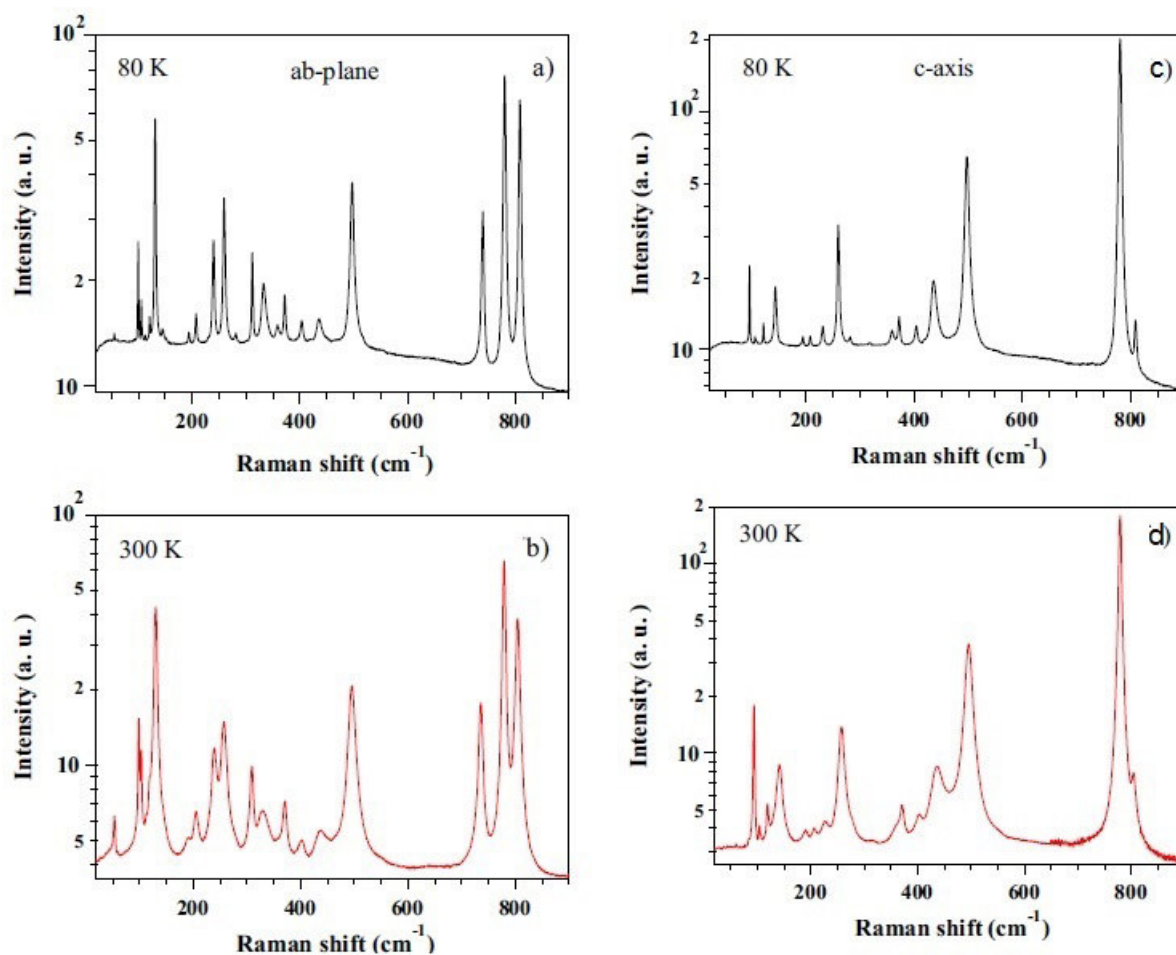
Figure 4.10: Raman spectrum of $Ba_2CuGe_2O_7$ at (a) 80 K and (b) 300 K, with the incident radiation polarized along the a axis. The spectra are not corrected for the temperature.c)Raman spectrum of $Ba_2CuGe_2O_7$ at (c) 80 K and (d) 300 K, with the incoming radiation polarized along the c axis. Nine of these lines also appear in the spectra of Fig. 4.10. The spectra are not corrected for the temperature.

4.4   Electronic bands and optical conductivity of $Ba_2CuGe_2O_7$

In previous Section the infrared and Raman spectra of $Ba_2CuGe_2O_7$ are shown and successfully compared with shell-model calculations of its vibrational dynamics.

In this Section, $Ba_2CuGe_2O_7$ electronic bands are investigated [114]. Optical spectra are taken at different temperatures from the mid-infrared (MIR) to the visible with the radiation polarized in the ab plane and along the c axis. The reflectivity is measured in the ab plane and along the c axis of a single crystal of the $Ba_2CuGe_2O_7$, from 20 to 300 K and from 700 to 24000 cm^{-1}. The reflectivity of $Ba_2CuGe_2O_7$ is shown at different temperatures, for both polarizations, in Fig. 4.11 a)- b).

There in one may remark the low absolute values of R(ω), which overcomes 0.2 in the visible range only. This is due to a sharp increase of the reflectivity, better shown in the insets, which at room temperature is observed around 13000 cm^{-1} in the ab plane (a), around 14000 cm^{-1} along the c axis (b). Both insets also show the temperature dependence of the edge of that absorption band, which unusually softens for decreasing temperature. In the main figure, both spectra also exhibit a MIR band between about 2000 and 4000 cm^{-1}. It also exhibits a strong temperature dependence, but in the opposite way. The features around 1500 cm^{-1} in both panels, enhanced by the overall low reflectivity of the sample, may be tentatively ascribed to overtones of the highest-frequency strong phonons of $Ba_2CuGe_2O_7$.

The real part $\sigma(\omega)$ of the optical conductivity is shown in Fig. 4.11 c)- d) for the whole spectral region of the present experiment.

The narrow peaks in the far infrared are due to the highest-frequency phonon modes. In Fig. 4.11 c)-d), the lowest-energy broad feature is a MIR band, which in the ab plane hardens between 300 and 20 K by more than 1000 cm^{-1}. On the contrary, the corresponding band measured along the c axis does not shift appreciably, while its intensity grows smoothly for decreasing temperature. The already mentioned behavior with temperature of the edge of the near infrared (NIR) band, in both polarizations, is confirmed in Fig. 4.11 c)- d). When cooling the sample from 300 to 20 K, it softens by about 1500 cm^{-1} in the ab plane, by even 2000 cm^{-1} along the c axis. As already remarked, this behavior is unusual, if compared for example with that of the optical gap in most semiconductors.

In conclusion, of this optical study three groups of absorption bands, rather weak, have been identified, in the mid infrared, near infrared and
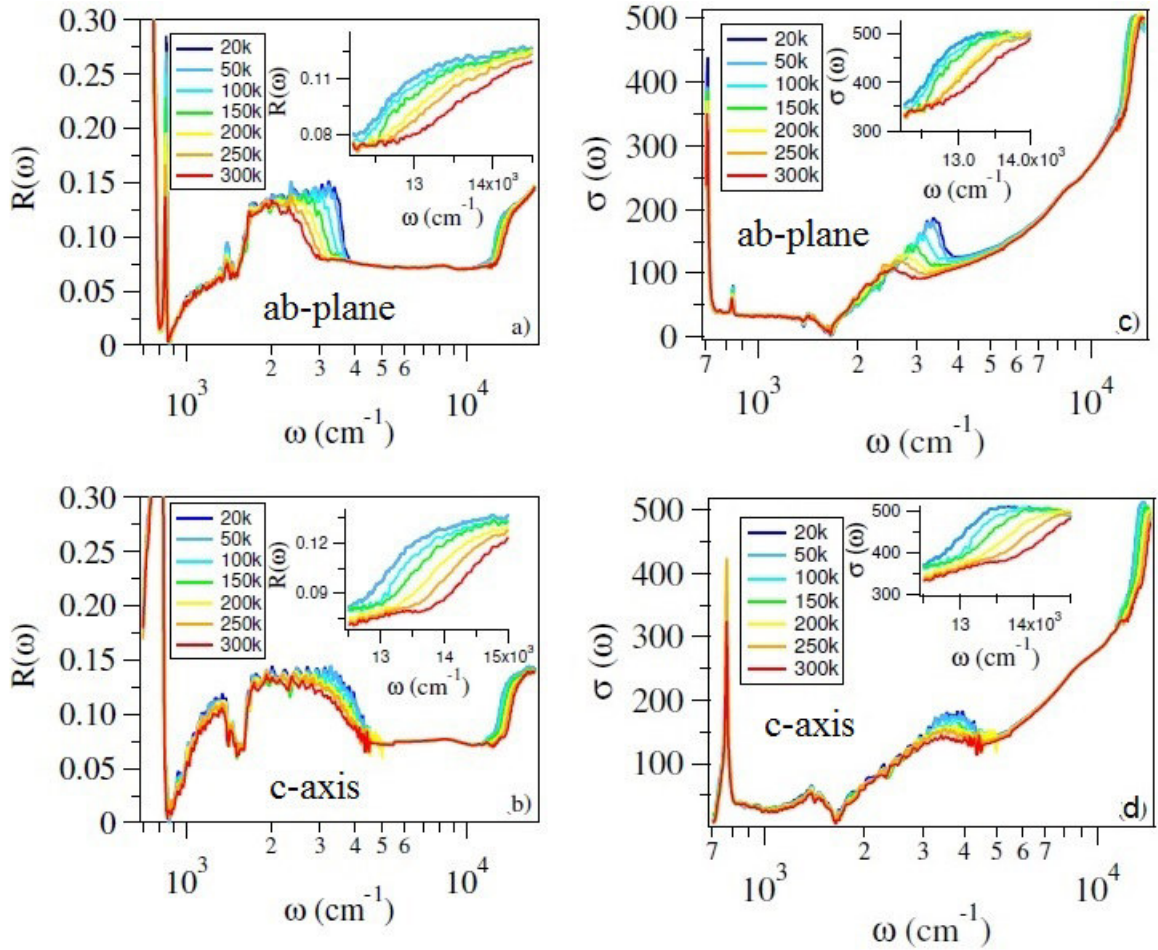
Figure 4.11: Reflectivity of $Ba_2CuGe_2O_7$ from the far infrared to the visible, with the radiation polarized in the ab plane (a) and along the c axis (b), at different temperatures. In the insets, the spectral region of the near infrared is enlarged to highlight the temperature dependence of the highest-energy band edge. c) Optical conductivity of $Ba_2CuGe_2O_7$ from the far infrared to the visible spectral region, with the radiation polarized along the a axis (c) and along the c axis (d), from 300 K to 10 K. In the insets, the spectral region of the near infrared is enlarged to better show the temperature dependence of the highest-energy band edge.

visible range.

The band structure has then been determined for the *ab* plane by a DFT approach and the resulting optical conductivity has been calculated by the Kubo-Greenwood formula. Also the resulting, theoretical $\sigma(\omega)$ exhibits three groups of bands, whose frequencies are in substantial agreement with the observations.

The experiment also shows that, interestingly, both the MIR band of the ab plane and those for both polarizations in the visible range, are strongly temperature dependent.

Even if our DFT calculations cannot provide T-dependent results, the observed effects could be due to a distortion of the Cu-O bond angles in the CuO_4 tetrahedra. Indeed, both the calculated MIR band and the edge of the band in the visible are extremely sensitive to those parameters. The observed band shifts can indeed be qualitatively reproduced by variations in the Cu-O bond angle α by less than 3°. Probably, the main effect of temperature on the $Ba_2CuGe_2O_7$ lattice is such distortion.

Conclusions

This thesis is focused on helimagnets $Ba_2CuGe_2O_7$ and $Cu_3Nb_2O_8$. It is well known that helimagnets can host a number of interesting anisotropic properties. These studies require the preparation of high quality samples.

$Ba_2CuGe_2O_7$ single crystals are successfully grown by the floating zone technique using both two and four mirror optical floating-zone furnaces. The synthesis procedure of the polycrystalline rods is found to be a critical factor for the crystal growth.

Several crystal growth conditions are attempted and the optimized conditions to produce the best crystals are described in detail.

The excellent crystallinity of the crystals obtained is confirmed by the FWHM value of X-ray rocking curve.

The magnetic ground state is investigated via dc magnetometry measurements. The experiments show the existence of different magnetic phases, the transition at 0.6 K is new and rather unexpected. Given this complexity, further low-field low-temperature studies are needed to fully understand the role of antisymmetric exchange interactions in establishing new types of magnetic order.

While magnetoelectric properties of $Ba_2CuGe_2O_7$ have been extensively discussed in past research, no investigation is reported on its lattice dynamics. In this thesis, infrared and Raman phonon spectra of $Ba_2CuGe_2O_7$ are also shown.

The spectra confirm that the tetragonal symmetry is conserved down to the lowest temperatures, with no appreciable orthorhombic distortion.

Optical study is completed by measuring the optical conductivity in the region of electronic bands of $Ba_2CuGe_2O_7$, both in the ab plane and along the c axis. Three groups of absorption bands, rather weak, are identified, in the mid infrared, near infrared and visible range. It would be interesting to investigate the pressure dependence of the optical properties of $Ba_2CuGe_2O_7$,

which would allow one to verify directly the role of local distortions of CuO_4 in determining the electronic band structure and optical conductivity. $Ba_2CuGe_2O_7$ shows a complex magneto-electric behaviour and additionally hosts a number of interesting properties, as well as is predicted to host magnetic skyrmions.

This work underlines that melilite-type oxides are potential targets for exploring interesting magnetic and electronic properties as well as multiferroicity and magneto electric effects. The physical properties of melilite oxides mainly depend on the nature of the transition metal ion, thus interesting properties could emerge in mixed melilite oxides. This work investigates two mixed melilite oxides: $Ba_2Cu_{(1-x)}Mn_xGe_2O_7$ and $Ba_2Cu_{(1-x)}Ni_xGe_2O_7$.

Furthermore, mixed polycrystalline samples $Ba_2Cu_{(1-x)}Mn_xGe_2O_7$ are successfully synthesized by solid state reaction. The series of samples with x changing in the range (0;1), show an almost constant value for the a-axis, while a linear trend exists for the c-axis.

Mixed polycrystalline samples $Ba_2Cu_{(1-x)}Ni_xGe_2O_7$ are successfully synthesized by solid state reaction. XRD analysis shows that $x=0.3$ is the limit solubility.

The evolution of cell parameters of $Ba_2Cu_{(1-x)}Ni_xGe_2O_7$ as a function of Ni content is investigated. For $x<0.3$, the addition of nickel to structure involves a linear stretching of c-axis and a parallel shortening of a-axis, while for $x>0.3$, the cell parameters keep constant.

Single crystals of $Ba_2Cu_{(1-x)}Ni_xGe_2O_7$, with x in the range (0.05;0.3), are successfully grown by the floating zone technique.

This work reports optimized conditions to produce the single crystals. The excellent crystallinity of the crystals obtained is confirmed by the very low FWHM value of X-ray rocking curve. The FWHM of $Ba_2Cu_{(1-x)}Ni_xGe_2O_7$ is similar to one acquired on $Ba_2CuGe_2O_7$ single crystal.

X-ray Laue back reflection and EBSD techniques are used to orient single crystals specifically for selected experiments.

To study the magnetic phase diagrams of grown crystals, magnetization measurement as a function of temperature (M(T)) is performed.

This work shows that M(T) curves of $Ba_2Cu_{0.95}Ni_{0.05}Ge_2O_7$ and of $Ba_2Cu_{0.92}Ni_{0.08}Ge_2O_7$ are similar to the $Ba_2CuGe_2O_7$ behaviour but with greater intensity.

In conclusion, these investigations indicate that substitution of Nickel on Copper site induces effects on magnetic and structural properties. They are a crucial step to further studies as for example neutron diffraction on single crystal samples to study the magnetism of this system.

$Cu_3Nb_2O_8$ single crystals are successfully grown by the floating zone tech-

nique. This work reports optimized conditions to produce the best crystals using both two and four mirror optical floating-zone furnaces.

The single crystals are found to be of highest quality as characterized by polarized optical microscopy, EDS, X-ray powder diffraction, and X-ray Laue diffraction measurements.

$Cu_3Nb_2O_8$ crystal cleaves without a natural favourite crystallographic direction, therefore the X-ray Laue back reflection and EBSD techniques are used to orient single crystals specifically for selected experiments.

To study the magnetic phase diagrams of grown crystals, magnetization measurement vs temperature is performed.

$Cu_3Nb_2O_8$ is one of only two multiferroic known with centrosymmetric triclinic crystal structure with P -1 space group. We report magnetization data measured along the a-, b- and c-axes. The M(T) curves in $Cu_3Nb_2O_8$ are anisotropic, with the magnitude of the magnetization being significantly different along each axis.

Moreover, dM/dT show a peak at T = 25K for magnetic field applied along the crystallographic axes. These divergences match to cusps in specific heat plot and with a ferroelectric transition reported in literature.

The bulk property measurements motivate the need to further investigate the different phases present in $Cu_3Nb_2O_8$ using neutron diffraction. Some preliminary information on the nature of the magnetic order is now available, however, completion of these study would be very useful for microscopically characterising the magnetic phases.

Acknowledgments

First of all, I would like to acknowledge my supervisors Dr. Antonio Vecchione and Professor Sandro Pace for the advice and support I have received for the last three and a half years. It has been a real pleasure to work with them. I am extremely grateful to Dr. Rosalba Fittipaldi of CNR-Spin-Salerno for her help with carrying out physical measurements and understanding the results. It has been a privilege to work with you.

Thanks to my supervisor Professor Geetha Balakrishnan for supervising the crystal growths and for her advice on Laue imaging system at Warwick University. A special thanks to Dr. Monica Ciomaga Hatnean for her assistance.

Many thanks to Dr. Veronica Granata, Dr. Alberto Ubaldini, Dr. Anita Guarino for lots of moral support.

Finally, I would like to thank and dedicate this thesis to my family for all support and encouragement. To my wonderful Mum, thank you for your love and support, and Dad, I hope you can enjoy what life brings to you, for you have both been such successful parents. Special thanks for the support from my irreplaceable sister and Carminuccio, my brother acquired.

To my boyfriend, Armando, thank you for the way you love me.

By the will of God to whom I give thanks.

Bibliography

[1] Williams, Wernick, Sherwood, and Wertheim, J. Appl. Phys.,37 ,1256, (1966)

[2] Brown, Forsyth, and Lander, J. Appl. Phys., 39,1331, (1968).

[3] Ishikawa, Tajima, Bloch, and Roth, Solid State Commun., 19,525, (1976).

[4] Moriya, Solid State Commun., 20, 291, (1976)

[5] Thessieu, Peiderer, Stepanov, and Flouquet, J. Phys. Condens. Matter, 9, 6677, (1997).

[6] Ishimoto, Yamaguchi, Suzuki, Arai, Furusaka, and Endoh, Physica B, 213, 214, 381, (1995)

[7] Yu, Onose, Kanazawa, Park, Han, Matsui, Nagaosa, and Tokura, Nature, 465,901, (2010)

[8] Wilhelm, Barnitz, Schmidt, Robler, Leonov, and Bogdanov, Phys. Rev. Lett., 107, 127203, (2011).

[9] Murakawa, Onose, Miyahara, Furukawa, and Tokura, Phys. Rev. B 85, 174106 (2012).

[10] Johnson, Nair, Chapon, Bombardi, Vecchini, Prabhankaran, Boothroyd, Radaelli, Physical Review Letters, 107, 137205 (2011)

[11] Tokura, Seki and Nagaosa Rep. Prog. Phys. 77,076501 (2014)

[12] Dzaloshinsky, J. Phys. Chem. Solids 4, 241 (1958)

[13] Moriya, Phys. Rev. Lett. 4, 228 (1960).

[14] Moriya, Phys. Rev. 120, 91 (1960)

[15] Felser, Angew. Chem. Int. Ed. 52, 2 (2013)

[16] Vopsaroiu, Blackburn, and Cain, Journal of Physics D, Applied Physics 40, 5027 (2007).

[17] Zhang, Li, Deng, Nan, Applied Physics Letters 92, 152510 (2008).

[18] S. Muhlbauer, Gvasaliya, Ressouche, Pomjakushina, and Zheludev, Phys. Rev. B, 86, 024417 (2012)

[19] Robler, Bogdanov, Pfleiderer, Nature, 442, 797 (2006)

[20] Wills, Physica B, 276, 680(2000)

[21] Yoshiro Kakehashi, Modern Theory of Magnetism in Metals and Alloys, Springer Science (2013)

[22] S. Blundell, Magnetism in Condensed Matter, Oxford University Press, New York, (2001)

[23] Bauer, Chacon, Wagner, M. Halder, Georgii, Rosch, Pfleiderer, M. Garst, Phys. Rev. B 95, 024429,(2017)

[24] Belitz, Kirkpatrick, Phys. Rev. B, 81,184419, (2010).

[25] Nagaosa and Tokura Nature nanotechnology, 8 (2013)

[26] Muhlbauer, Binz, Jonietz, Peiderer, Rosch, Neubauer, Georgii, and Boni, Science, 323,915, (2009).

[27] Schmid, Ferroelectrics 162, 317 (1994).

[28] Aizu, Phys. Rev. B 2, 754 (1970).

[29] Spaldin, Cheong, Ramesh, Physics Today, 38, (2010)

[30] Katsura, Nagaosa, Balatsky, Phys. Rev. Lett. 95, 057205 (2005)

[31] Mostovoy, Phys. Rev. Lett. 96, 067601 (2006).

[32] Sergienko, Dagotto, Phys. Rev. B 73, 094434 (2006).

[33] Khomskii, Bull. Am. Phys. Soc. C 21.002 (2001).

[34] Baryakhtar, Chupis, Sov. Phys. Solid State 10, 28182821 (1969).

[35] Baryachtar, Lvov, Jablonskii, JETP Lett. 37, 673 (1983).

[36] Stefanovskii, Jablonskii, Sov. J. Low Temp. Phys. 12, 478 (1986)

[37] Harris, Yildirim, Aharony, Entin, Wohlman, Towards, Phys. Rev. B 73, 184433 (2006).

[38] Kimura, Goto, Shintani, Ishizaka , Arima and Tokura ,Nature, 426, 55 ,8 (2003)

[39] Kimura, Lashley and Ramirez ,Phys. Rev. B 73,220401,(2006)

[40] Yamasaki , Miyasaka , Kaneko , He, Arima and Tokura , Phys. Rev. Lett.,96,207204,(2006)

[41] Taniguchi, Abe, Takenobu,Iwasa and Arima,Phys. Rev. Lett.,97,097203,(2006)

[42] Arkenbout, Palstra, Siegrist and Kimura, Phys.Rev. B 74,184431,(2006)

[43] Kezsmarki, Bordacs,Milde, Neuber, Eng, White,Ronnow, Dewhurst, Mochizuki, Yanai, Nakamura,Ehlers, Tsurkan, Loidl, Nature Materials 14, 11161122 (2015)

[44] Boren, Kemi, Mineral. Geol. , 11A, 10, (1934)

[45] Munzer, Neubauer, Adams, Muhlbauer, Franz, Jonietz, Georgii, Boni, Pedersen, Schmidt, Rosch, Pfleiderer, Phys. Rev. B , 81, 041203 (2010)

[46] Yu, Kanazawa, Onose, Kimoto, Zhang, Ishiwata, Matsui, Tokura, Nat. Mater. 10, 106 (2011)

[47] Seki, Yu, Ishiwata, Tokura, Science, 336, 198, (2012)

[48] Lin, Grundy,Giess, Appl. Phys. Lett. 23, 485487 (1973).

[49] Okubo, Chung, S. Kawamura, Phys. Rev. Lett. 108, 017206 (2012)

[50] Heinze, Nature Phys. 7, 713 (2011).

[51] Alam, Gooen, Di Bartolo, Linz, Sharp, Gillespie, and Janney, J. Appl. Phys. 39, 4728 (1968).

[52] Allik, Ferry, Reeves, Powell, Hovis, Caffey, Utano, and Campana, J. Opt. Soc. Am. B 7, 1190 (1990).

[53] Liebertz and Stahr, Kristallogr. 159, 271 (1982).

[54] Bohaty and Liebertz, Kristallogr. 159, 277 (1982).

[55] Endo, Doi, Wakeshima, Hinatsu, Inorg. Chem. 23, 10809, (2010)

[56] Ochi, Morikawa, Marumo, Nozaki, Rev. Yogyo Kyokai Shi, 91, 229 (1983).

[57] Masuda, Kitaoka, Takamizawa, Metoki, Kaneko, Rule, Kiefer, Manaka, Nojiri, Phys. Rev. B, 81, 100402, (2010).

[58] Zheludev, Sato, Masuda, Uchinokura, Shirane, Roessli, Phys. Rev. B, 68, 024428 (2003).

[59] Zheludev, Maslov, Shirane, Sasago, Koide, and Uchinokura, Phys. Rev. Lett. 78, 4857 (1997).

[60] Petrakovskii, Bezmaternykh, Gudim,Sheptyakov, Bayukov, Vorotynov, Velikanov, Bovina, Phys. Solid State, 47, 2114, (2005).

[61] Petrakovskii, Bezmaternykh, Gudim, Bayukov, Vorotynov, Bovina, Szymczak, Baran, Ritter, C. Phys. Solid State, 48, 1906,(2006).

[62] Akaki, Tozawa, J.; Akahoshi, D.; Kuwahara, H. J. Phys.: Conf. Ser. 150, 042001, (2009).

[63] Takashi, Endo, Doi, Hinatsu and Ohoyama, Inorganic Chemistry , 51, 3572 (2012)

[64] Zheludev, Maslov, Shirane, Sasago, Koide, Uchinokura, Tennant, Nagler, Phys. Rev. B , 56, 14006 (1997).

[65] Barone, Yamauchi, and Picozzi, Phys. Rev. B, 92, 014116 (2015)

[66] Seki, Onose, and Tokura, Phys. Rev. Lett. 101, 067204 (2008).

[67] Murakawa, Onose, and Tokura, Phys. Rev. Lett. 103, 147201 (2009).

[68] McMurdie,Powder Diffr. 1, 64 (1986)

[69] Yi, Choi, Lee, Cheong, Appl. Phys. Lett. 92, 212904 (2008)

[70] Bogdanov, Robler, Wolf, and Muller, Phys. Rev. B 66, 214410 (2002).

[71] Bogdanov and Yablonski, Sov. Phys. JETP 68, 101(1989)

[72] Bogdanov and Shestakov, Phys. Sol. State 40, 1350 (1999).

[73] Zheludev, Maslov, Shirane, Tsukada, Masuda, Uchinokura, Zaliznyak, Erwin, and Regnault, Phys. Rev. B 59, 11432 (1999).

[74] Zheludev, Maslov, Shirane, Sasago, Koide, and Uchinokura, Phys. Rev. B 57, 2968 (1998).

[75] Park, Choi, Zhang and Cheong, Phys. Rev. Lett.98 057601 (2007)

[76] Lu, Whangbo, Dong, Gonh and Xiangm Phys. Rev. Lett. 108, 187204 (2012)

[77] Johnson, Chapon, Khalyavin, Manuel, Radaelli, Martin, Phys. Rev. Lett. 108, 067201 (2012)

[78] Kurumaji, Seki, Ishiwata, Murakawa, Tokunaga, Kaneko, Tokura, Phys. Rev. Lett. 106 167206 (2011).

[79] Zheng, Whangbo, Gong, Xiang, Phys. Rev. B 86, 174401(2012)

[80] Robertson, Kostiner, J. Solid State Chem. 4, 29 (1972).

[81] Ashcroft, Mermin, Solid State Physics, Holt Rinehart and Winston (1976).

[82] Kooy, Couwenberg, Philips Techn. Rundschau 23,143 (1962).

[83] Mizutani, Matsumi, Makino, Yamamoto, Kato, NEC Res. Dev. 33, 86 (1974)

[84] Eyer, Nitsche, Zimmermann, J. Cryst. Growth 47, 219 (1979)

[85] Hurle, Handbook of Crystal Growth, vol. 2,242 (1994)

[86] Croll, German Assoc. Cryst. Growth (DGKK) Newslett. 65,13 (1997)

[87] Fittipaldi, Rocco, CiomagaHatnean, Granata, Lees, Balakrishnan, Vecchione, Journal of Crystal Growth 404 223 (2014)

[88] Granata, Ubaldini, Fittipaldi, Rocco, Pace, Vecchione Journal of Crystal Growth 457 128 (2017)

[89] Sirotinkin, Russ. J. Inorg. Chem., Vol. 37, 1334 (1992)

[90] Sharma, Saha, Kaushik, Siruguri, Patnaik, Solid State Communications 203 54 (2015)

[91] The HighScore suite, Degen, Sadki, Bron, Konig, Nnert, Volume 29, Supplement S2, (2014)

[92] Young,IUCr Monographies of Crystallography, 5; Oxford University Press: Oxford, U.K., (1993)

[93] Rietveld, J. Appl. Cryst. 2, 6571 (1969)

[94] Bowen and Tanner, High Resolution X-ray Diffractometry and Topography,(1998)

[95] X' Pert Pro User's Guide

[96] Fittipaldi, Vecchione, Fusanobori, Takizaw, Yaguchi, Hooper, Perry, Maeno, Journal of Crystal Growth 282, 152,(2005)

[97] Armigliato, Valdre, Microscopia elettronica a scansione e microanalisi parte I,(1981)

[98] Armigliato, Valdre, Microscopia elettronica a scansione e microanalisi parte II,(1981)

[99] Schwartz, Kumar, Adamse, Electron Backscatter Diffraction in Material Science,(1980)

[100] Jensen, Texture and Microstructures 20, 55 (1993)

[101] Oxford Instrumental Analytical, technical brieging, Electron Backscattered Diffraction, explained (1993)

[102] Tovar, Dinnebier, Eysel, Mater.Sci.Forum 278 750755 (1998).

[103] Hutanu, Sazonov, Murakawa, Tokura, Nafradi, Chernyshov, Phys.Rev.B Condens.Matter 84,212101,(2011)

[104] Biegalski, Jornal Of Applied Physics,104, 114109 (2008)

[105] Song, Jornal Of Crystal Growth, 223,129 (2001)

[106] Rodriguez,Carvajal Jornal Physica B., 192, 55 (1993)

[107] Muhlbauer, Gvasaliya, Pomjakushina, Zheludev,Phys. rev. B, Condensed matter 84,18, (2011)

[108] M. McElfresh, Quantum Design Fundamentals of Magnetism and Magnetic Measurements Featuring Quantum Design's Magnetic Property Measurement System, (1994)

[109] Wartewing, IR and Raman Spectroscopy: Fundamental Processing, (2003)

[110] Sole, Bausa, An Introduction to the Optical Spectroscopy of Inorganic Solids, Wiley (2005)

[111] Zheludev, Shirane, Sasago, Kiode, Uchinokura, Phys.Rev.B Condens. Matter 54,15163(1996).

[112] Nucara, Mohamed, Baldassarre, Koval, Lorenzana, Fittipaldi, Balakhrisnan, Vecchione, and Calvani, Phys. Rev. B 90, 014304 (2014)

[113] Capitani, Koval, Fittipaldi, Caramazza, Paris, Mohamed, Lorenzana, Nucara, Rocco, Vecchione, Postorino, and Calvani, Phys. Rev. B 91, 214308 (2015)

[114] Corasaniti, Barone, Nucara, Ortolani, Baldassarre, Fittipaldi, Granata, Rocco, Vecchione, Mohamed, Lorenzana, Calvani, submitted to Phys. Rev. B (2017)